Final Report for Project No. DE-FG07-04ID14603

Novel Nuclear Powered Photocatalytic Energy Conversion

John R. White, Douglas Kinsman, Thomas M. Regan, and Leo M. Bobek

UMass-Lowell Radiation Laboratory
University of Massachusetts Lowell

August 29, 2005

I. Introduction

I.1 Project Overview

The University of Massachusetts Lowell Radiation Laboratory (UMLRL) is involved in a comprehensive project to investigate a unique radiation sensing and energy conversion technology with applications for in-situ monitoring of spent nuclear fuel (SNF) during cask transport and storage. The technology makes use of the gamma photons emitted from the SNF as an inherent power source for driving a GPS-class transceiver that has the ability to verify the position and contents of the SNF cask. The power conversion process, which converts the gamma photon energy into electrical power, is based on a variation of the successful dye-sensitized solar cell (DSSC) design developed by Konarka Technologies, Inc. (KTI).[1] The basic concept of the program is to extend the proven ability of KTI's new class of photovoltaic conversion devices to produce power from high-energy photons. In particular, the goal of the current research is to make direct use of the high-energy gamma photons emitted from SNF, coupled with a scintillator material to convert some of the incident gamma photons into photons having wavelengths within the visible region of the electromagnetic spectrum. The high-energy gammas from the SNF will generate some power directly via Compton scattering and the photoelectric effect, and the generated visible photons output from the scintillator material can also be converted to electrical power in a manner similar to that of a standard solar cell. Upon successful implementation of an energy conversion device based on this new "gammavoltaic" principle, this inherent power source could then be utilized within SNF storage casks to drive a tamper-proof, low-power, electronic detection/security monitoring system for the spent fuel.

The current project has addressed several aspects associated with this new energy conversion concept, including the development of a base conceptual design for an inherent gamma-induced power conversion unit for SNF monitoring, the characterization of the radiation environment that can be expected within a typical SNF storage system, the initial evaluation of Konarka's base solar cell design, the design and fabrication of a range of new cell materials and geometries at Konarka's manufacturing facilities, and the irradiation testing and evaluation of these new cell designs within the UML Radiation Laboratory. The primary focus of all this work was to establish the proof of concept of the basic gammavoltaic principle using a new class of dye-sensitized photon converter (DSPC) materials based on KTI's original DSSC design.

The purpose of this report is to overview the overall gammavoltaic energy concept and to summarize the key aspects of the work performed to date. In achieving this goal, the report clearly establishes the viability of the basic gammavoltaic energy conversion concept, yet it also identifies a set of challenges that must be met for practical implementation of this new technology. Thus, this initial work has indeed established proof of concept, but a fair amount of further research is still required to fine-tune the concept, to optimize the first generation of gammavoltaic cells, and to answer a number of operational and lifetime-related questions that were left unanswered by this initial research.

I.2 Scope of Report

The remainder of this report expands upon the above introductory comments in further detail. Section II elaborates on the basic gammavoltaic principle and its application within a self-powered SNF monitoring system. This section also briefly describes the key differences between the existing solar cell design and the new gammavoltaic cells developed in this work.

The characterization of the radiation environment for a typical SNF storage system is summarized in Section III (and treated in detail in the Appendix). This effort involved the use of standard computational methods to characterize the radiation environment at various locations within a typical interim spent fuel storage system. The goals here were to determine the time-dependent radiation dose rate and the integral dose as a function of the expected service lifetime for the gammavoltaic power conversion system. This analysis was an essential first step in this overall research effort, since the results from this study provided the initial estimates of expected dose rates and lifetime fluence at various locations within a typical cask. These data were used to guide the experimental program and for selection of the optimal placement of the power conversion unit within the cask, both in terms of the input power available to the device and its useful operational lifetime.

Section IV overviews a preliminary review of candidate scintillator materials. Incorporating a suitable scintillator directly with the gammavoltaic cell design is essential from the viewpoint of conversion efficiency, so this subject will become particularly important in future studies concerning cell optimization (only gadolinium oxysulphide has been tested in the current study).

Section V discusses the basic test setup for measuring the power conversion capability of the existing and newly developed cells, and some generic results (and lessons learned) from the initial testing phase of this work. Also included here are discussions of the design process for the new cells and a review of the various configurations studied to date.

The primary results from the current work are presented in Section VI, with focus on the performance of the latest cell designs. Standard current versus voltage relationships (the I-V curves) are presented for individual cells and for simple series and parallel arrangements of cells. The additive nature of the output voltage and current in the series and parallel configurations, as demonstrated here, is very important, since this feature allows for the scale-up of the tested geometries to produce a useful amount of electricity to drive a low-power SNF monitoring system. An example scale-up calculation is included to predict the actual cell configuration needed for a typical gammavoltaic energy conversion module.

In addition, Section VI also presents some preliminary results from an effort to develop a simple one-diode model of a DSPC cell that adequately describes the observed behavior of the gammavoltaic cells. The goal here is to have some capability to relate observed trends in cell

performance to various cell design and construction features and to the integrated dose level associated with a given test cell. The final subsection here also briefly describes some microscopic material characterization work that was initiated as part of this overall project. However, as of this writing, this characterization work is still ongoing, and no real comparisons and conclusions are available at this time.

Lastly, Section VII summarizes the current status of this work and identifies several areas where further investigation is required. This initial research has answered the feasibility question concerning the gammavoltaic power conversion concept, but there are still many unresolved issues concerning the practical use of this concept for the intended SNF monitoring application. Further study is required to address some of these issues and to explore the potential for using the basic gammavoltaic concept in other application areas.

II. Overview of Self-Powered SNF Monitoring System

II.1 Concept Overview

The UMass-Lowell Radiation Laboratory is working on a project to develop a radiation hardened photovoltaic-based energy converter optimized for converting the decay gamma photons from spent nuclear fuel (SNF) into useful electric power. The generated power would then be used to operate a secure GPS-class transceiver that provides information about the location and integrity of the spent fuel. The need for an integral self-powered monitor for SNF is associated with a number of safety and security issues surrounding the transport and storage of large quantities of spent fuel within the US and abroad.

For example, SNF storage within dry casks has been approved at several distributed locations throughout the US in Independent Spent Fuel Storage Installations (ISFSI) close to the sites where the waste was generated.[2] And, as the amount of available storage space in the on-site spent fuel pools continues to decrease, the number and size of the ISFSIs will continue to grow. Although these sites are quite secure and pose minimal risk from theft or sabotage, the spent fuel cask locations, physical integrity, and radioactive level are not currently monitored on a continuous basis. However, a combination radiation-detection/energy-conversion device coupled to a remote GPS transceiver could fill this void and provide an additional level of safety, security, and peace of mind for the SNF storage facility and the nearby populations.

Concerning SNF transport, the tracking of vehicles using a Global Positioning System (GPS) is a mature technology that is currently in routine use within the US.[3] In particular, the TRANSCOM system[4] is currently used to monitor the shipment of spent fuel by the US Department of Energy. The TRANSCOM system utilizes satellite-based communications and a server-based application to allow for remote users to track and locate a TRANSCOM equipped truck quite accurately. In the present system, however, the transponder is mounted to the transport vehicle, not the actual fuel shipment -- that is, no direct measurements from the spent fuel are recorded during transportation. Although unlikely, it is conceivable that the truck/transport vehicle and SNF shipment could be separated. Again, a self-powered GPS system that is integral to the SNF transport cask could address this concern.

In all, an improved SNF tracking system would better address the complex issues surrounding the shipment and storage of spent fuel. The new gammavoltaic power conversion system under

development as part of the current research represents a novel technological solution to these issues -- since a self-powered GPS system could potentially provide the needed information on both the physical location and the status of the fuel and transport/storage cask system at all times.

One proposed solution for producing the power for the GPS system directly from the SNF takes advantage of the direct interaction (via Compton scattering and the photoelectric effect) of the high-energy SNF gammas within the cell. In addition, to increase the efficiency of the overall direct energy conversion process, a secondary two-step procedure is used, where a scintillator is first excited by the gamma photons from the SNF to produce light, and then this light is converted into electricity by a photovoltaic converter. This secondary indirect conversion of decay radiation into useful electric power will be accomplished using a combination of a gamma-sensitive scintillator such as gadolinium oxysulphide, which possesses a photon emission spectrum in the optical region, with a broad-spectrum photoconverter such as the dye-sensitized cells under development at Konarka Technologies.

This particular direct energy conversion system was chosen because of the relatively low temperatures and quality of the energy associated with radioactive decay in aged fuel (the spent fuel is allowed to decay for at least 5 years in the water-cooled spent fuel pool before transport or dry storage becomes an option). Thus, other energy conversion options, such as dynamic energy generation techniques or the use of a thermoelectric generator, are not really viable with this class of energy source. On the other hand, the proposed gammavoltaic direct energy conversion process takes full advantage of the large population of relatively high-energy photons and converts a portion of this waste energy into useful electric power. Also, since the gamma photon population is confined to the internal components of the storage container, any self-powered solution must be located in relatively close proximity to the SNF -- which also gives the added security benefit that the monitoring system cannot be physically separate from the fuel, and that it may also be configured so that it represents a continuous measure of the physical integrity of the fuel storage/transport canister.

II.2 Dye-Based Solar Cells

In the early 1990s, researchers at the Swiss Federal Institute of Technology found that a thin film solar cell composed of percolating networks of liquid electrolyte and partially sintered titanium dioxide nanoparticles could convert solar light to electricity with relatively high efficiencies.[5] Since that time, there has been a tremendous amount of basic research and development in this field, and Konarka Technologies has been a leader in this technology area for a number of years, with special emphasis on developing efficient low-cost manufacturing technologies for producing large quantities of flexible solar cells. In general, these dye-based titanium dioxide solar cells offer the potential for a significant reduction in the cost of solar electricity due to the inexpensive raw materials and simple fabrication process. In addition, for intended application within a high radiation environment, the characteristics of the base materials and the mode of operation of these cells may also offer unique advantages over crystalline, polycrystalline, and amorphous cells in terms of radiation-induced displacement damage. A simple sketch showing the basic layout of a typical dye-sensitized solar cell (DSSC) is given in Fig. 1.

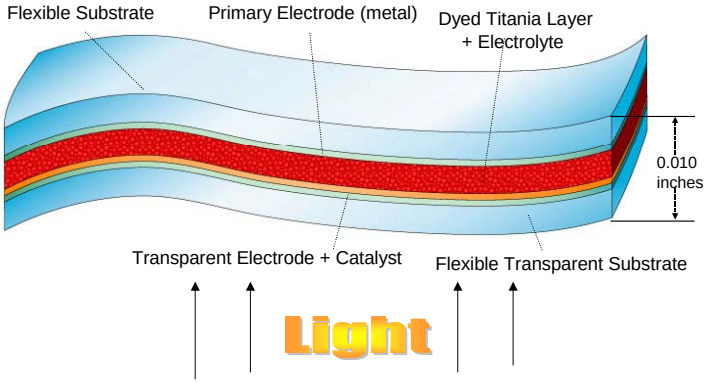

Fig. 1 Simple diagram of a flexible dye-based solar cell.

Dye-sensitized titania-based solar cells can use a variety of organic dyes to "sensitize" the TiO_2 particles, each with its own characteristic absorption spectrum. Also, in contrast to traditional photovoltaic materials, where the semiconductor performs both the task of light absorption and charge carrier transport, these two functions are separate in the DSSC. A single molecular layer of dye adsorbed on the titanium dioxide surface performs light absorption from the sun. The dye then transfers an electron to the titanium dioxide upon excitation by a photon. Charge separation occurs at the interface via photo-induced electron injection from the dye into the conduction band of the solid. The electrons are passed to a conducting electrode through semiconducting TiO_2 channels. The positive charge on the oxidized dye is subsequently transferred to iodide/triiodide (or other redox components) present in the electrolyte solution with which the cell is filled, and subsequently to the counter electrode. The circuit is then closed through an external load to complete the electron transfer path. This process is illustrated in Fig. 2.

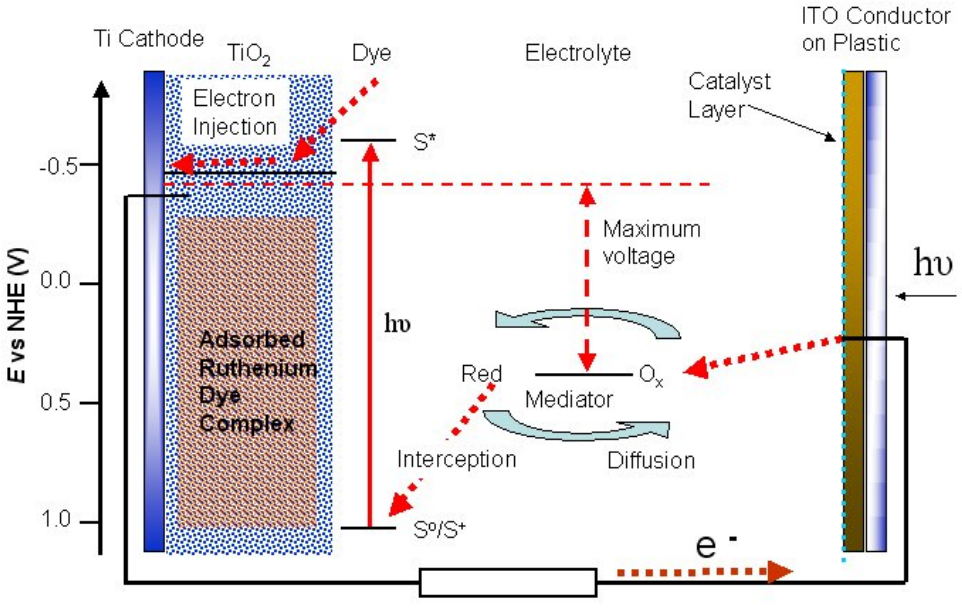

Fig. 2 Basic operation of a dye-sensitized solar cell.

The absorption of light by a single molecular layer of dye is very weak. Hence, a reasonable photovoltaic efficiency could not be obtained by the employment of a flat two-dimensional semiconductor surface. High surface roughness is achieved by employing a highly porous, nanostructured film, which is accomplished by making the semiconductor thin films from colloidal TiO_2 dispersions, followed by sintering or inter-connecting the nanoparticles at appropriate conditions. The end result is a "semiconductor sponge", which has thousands of adsorbed dye monolayers, as sketched in Fig. 3. The highly enhanced absorption by these numerous layers enhances the efficient conversion of photons into electricity. The reported solar conversion efficiency of over 10% from a dye sensitized nanoporous TiO_2 cell with liquid based iodide/triiodide redox electrolyte/mediator approaches that obtained from silicon and other inorganic photovoltaic cells.[6] Furthermore, nanocrystalline TiO_2 has also proven to be stable for over ten years exposure to sunlight under laboratory conditions.

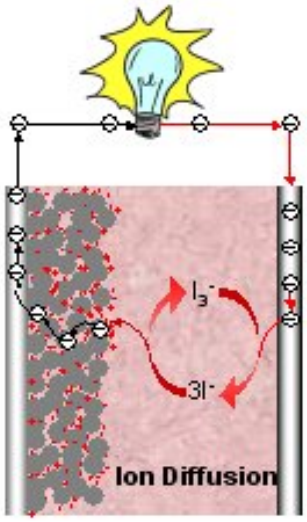

Fig. 3 Electron flow in a DSSC.

II.3 Gammavoltaic System Configuration

The basic thin film solar cell with its optically transparent ITO conductor design is optimized for use with solar spectrum radiation. This proven technology provided a solid basis from which the design of the gammavoltaic cell has evolved. In terms of physical operation, once again the single molecular layer of dye complex adsorbed on the titanium dioxide surface performs photon absorption, where the photons, in this case, are produced from both primary and secondary gamma ray interactions within the volume of the gammavoltaic cell. As in the operation of the solar cell, these gamma photons can directly excite the dye complex to transfer an electron to the titanium oxide. However, the dye complex remains primarily sensitive to photons in the visible wavelengths. Therefore, the addition of a gamma scintillator (such as gadolinium oxysulphide) to the cell volume allows for the internal production of optical photons with a peak emission intensity that closely matches the peak absorption spectra of several commonly used dyes. The electrons produced from both the gamma and optical photon interactions are passed, as usual, to the conducting electrode through the semiconducting channels in the TiO_2.

As expected, experimental determination confirmed that the plastic/ITO anode associated with the standard DSSC design degrades due to radiation damage from the high-energy gamma photon exposure. Thus, the existing solar DSSC system as sketched in Fig. 2 was modified to replace the plastic/ITO layer with a second titanium metal sheet to serve as an anode as shown in Fig. 4. This diagram highlights the two key differences between the gammavoltaic cell and the typical solar cell designs: the removal of the ITO/plastic electrode and the addition of a gamma scintillator to the liquid mediator/electrolyte to enhance the photon down conversion.

In addition to the changes already noted, it should be emphasized that removal of the requirement for a transparent conductor to allow visible light penetration also simplifies the design and construction of the cell geometry. Due to the increased conductivity of the second titanium electrode, the area of an individual cell can be increased significantly and, because light photons do not need to enter the cell, the individual thin film gammavoltaic cells can be stacked

or sandwiched in series to produce a much larger effective cell volume per unit surface area of cell. This is particularly important for the current application, since the majority of the high-energy incident gammas would simply pass through a single thin cell without interaction. However, by providing a larger effective cell volume, the probability of interaction should increase significantly -- thus, a larger portion of the incident gamma energy will be captured and subsequently converted into useful electrical power.

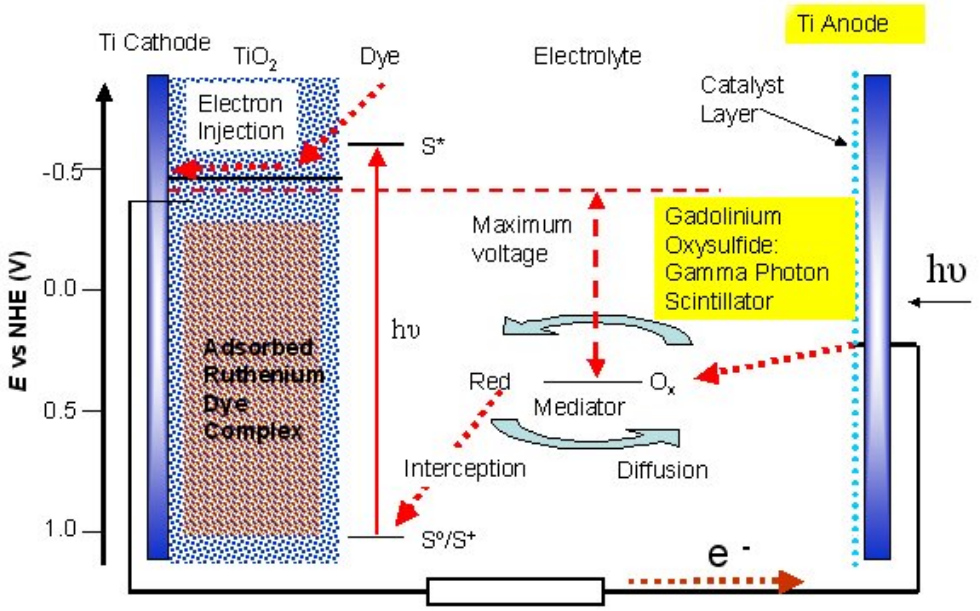

Fig. 4 Basic operation of a dye-sensitized gammavoltaic cell.

III. Characterization of a Typical SNF Cask Environment

Based on the above overview of the intended application and summary of the proposed gammavoltaic cell design, a testing program to evaluate the energy conversion capability of these devices was initiated. However, before physical testing could begin, an estimate of the expected conditions within a typical spent nuclear fuel canister was needed. In particular, reasonable estimates of the expected dose rates and lifetime integral doses were needed to set guidelines for the planned gammavoltaic test program. Thus, in support of the experimental program for this project, a series of computational models were developed and analyzed to characterize the overall radiation environment within a typical SNF storage cask. The specific goal of this separate task was to estimate the neutron and gamma dose rates at different locations within a typical storage canister and cask arrangement. In addition, an estimate of the time-integrated total dose was needed to establish the expected service lifetime of the photoconverter materials associated with the in-situ monitoring system. This information -- the dose rate and total integrated dose versus position within the storage system -- was needed to set parameter specifications for performing the material irradiations and to guide the overall concept development of the gammavoltaic energy conversion system.

A separate complete report[7] summarizes this radiation environment characterization effort, including the development of a computational model of a typical SNF interim storage system, the generation of macroscopic cross sections and response functions for use in the calculations, the development of the neutron and gamma sources within the SNF, and the actual radiation transport calculations and results. The reader should consult Ref. 7 for complete details of this study -- this reference is included in its entirety as an Appendix to this report. However, to make the current document self-contained and to keep it relatively focused, a brief overview of the work and the primary results from this separate effort are highlighted here.

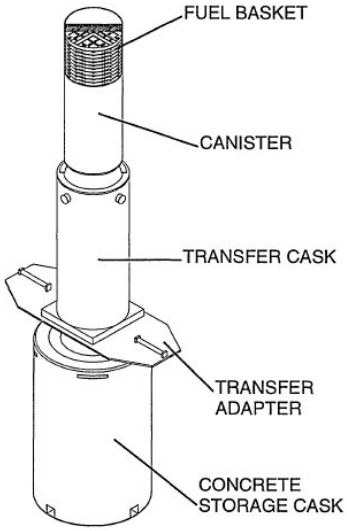

The NAC Universal Multipurpose Cask System[8] (NAC-UMS) was chosen as the typical storage configuration for the current study. As shown in Fig. 5, the NAC-UMS design discussed in Ref. 8 consists of a transportable storage canister, a vertical concrete cask, and a transfer cask that is used for safely transporting and transferring the spent fuel assemblies within the storage canister from the wet storage pool to the dry concrete cask. Since the transfer process occurs over a brief period of time, only the fuel basket/canister arrangement within the vertical concrete cask was treated here. A sketch of the actual storage configuration that was modeled is shown in Fig. 6.

Fig. 5 Basic NAC-UMS design.

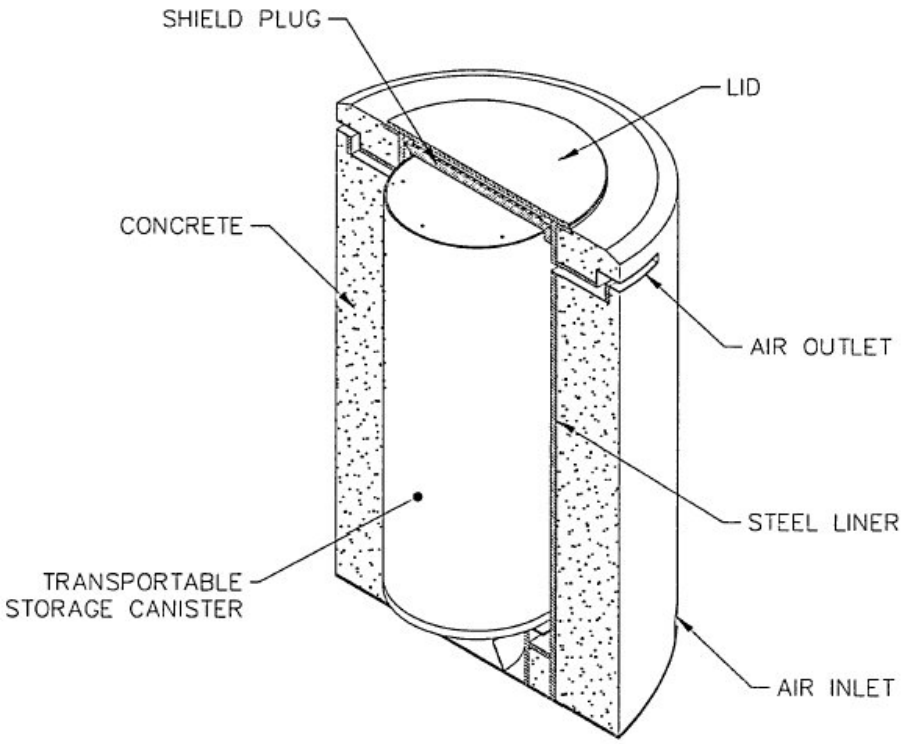

Fig. 6 NAC-UMS canister and vertical concrete cask arrangement (from Ref. 8).

A relatively simple RZ axisymmetric model that represents the geometry depicted in Fig. 6 was constructed for this study. The 2-D model does not include any air penetrations in the concrete cask, and the baffle/structural region just below the canister was simplified considerably. In addition, the fuel basket region, containing 24 PWR fuel assemblies, fuel tubes, neutron absorber material, and a series of stainless steel support disks and aluminum alloy heat transfer disks, was treated as a single 144-inch tall material region consisting of a homogenized mix of all the materials present within the fuel basket region. All the dimensions and material compositions for the model were obtained directly from Ref. 8.

To determine the neutron and gamma sources for the fuel region, a fuel depletion calculation was performed that models the behavior of a particular fuel assembly during the full lifetime of the element, while in the core and after removal from the reactor. A standard Westinghouse PWR 17x17 assembly design with an average burnup of 40000 MWD/MTU was chosen as a typical PWR fuel element. The results from this depletion/decay analysis give the source magnitude and energy spectrum as a function of SNF cool-down time. The source used for the radiation transport calculations was for a 5-year cooling period and, along with a full complement of maximum burnup fuel (at 40000 MWD/MTU), this represents the maximum fuel gamma source strength expected for the given SNF cask design. However, since only the fuel gamma source was treated in these calculations (i.e. the gammas emitted from the activated fuel assembly structural components were not included), it is expected that the source used here is probably quite representative of actual conditions in an average cask environment. Thus, the results obtained here should be a reasonable estimate of actual cask conditions.

Although several preliminary conclusions were made in Ref. 7 based only on the results of the radiation transport analyses performed there, now that some initial testing of the power-production capability has been completed, it is clear that the best location for the gammavoltaic energy conversion unit in the NAC-UMS storage configuration should be in the air gap between the transportable fuel canister and the steel liner for the concrete storage container (see Fig. 6). This location gives the best combination of gamma dose rate and temperature conditions for the power conversion device. As shown in Fig. 7, the gamma dose rate in air is estimated to be in the 8000 to 9000 rad/hr range and, from Ref. 8, the expected temperature range should be about 90 C - 110 C (assuming that the power conversion device is not mounted with good thermal contact directly to the canister shell).

With this expected dose rate, it is recommended that actual testing in the region of 1000 to 15000 rad/hr (or higher) be considered for the materials testing program. This large range is suggested, since there will be large variability from cask to cask and, certainly, there is a fair amount of uncertainty associated with these preliminary calculations. In addition, based on this range of dose rates and a target 30-year lifetime for the self-powered monitoring unit, integral doses ranging from 100 Mrad to 1600 Mrad are possible. Unfortunately, testing this large a range for the integral dose is not possible as part of the current project (because of time constraints and the fact that appropriately radiation hardened gammavoltaic cells are not currently available); however, the potential for very high integral doses clearly exists, and this will be a key issue to address in any future testing plans.

Concerning the expected thermal conditions in the cask environment, information on extended testing of the current class of dye-sensitized solar and gammavoltaic cells at elevated levels in the range of 90 C - 110 C is also not available (all the testing here was performed at room temperature). Thus, further characterization of the gammavoltaic cells envisioned for SNF self-

monitoring applications within an elevated thermal environment is clearly needed. However, again because of time limitations, this aspect of a complete testing program will have to become part of a future follow-on effort.

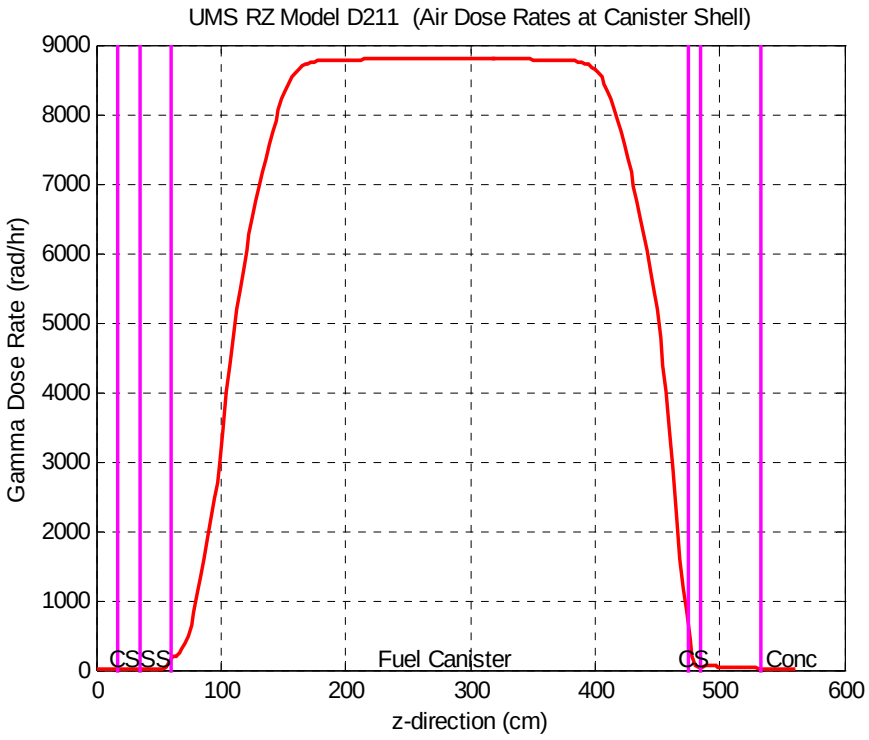

Fig. 7 Gamma dose rate axial profile at the canister shell.

In summary, the SNF cask environmental characterization study has determined a range of possible dose rates (1000 to 15000 rad/hr) and integral doses (100 Mrad to 1600 Mrad) to consider, it has identified the expected temperature range that the gammavoltaic cells will see (90 C - 110 C), and it has identified the radial air gap between the fuel storage canister and steel liner for the concrete shield as a likely candidate location for the self-powered gammavoltaic conversion unit. Although there is clearly a large uncertainty here (that can be refined in follow-on studies), the integral dose and dose rate estimates and the selected cask location obtained from this portion of the overall study are quite sufficient to help guide and parameterize the initial material testing phase of this project.

IV. Overview of Candidate Scintillator Materials

In order to increase the power output of the dye sensitized photon converters (DSPCs), the incident radiation energy should closely match the bandgap energy needed to excite sensitizing dye electrons from the highest occupied molecular orbital (HOMO) to the lowest unoccupied molecular orbital (LUMO) in the dye. This is illustrated in Fig. 8 (note that this figure is similar to Fig. 4, but here the primary focus is on the energy transfer processes in the cell).

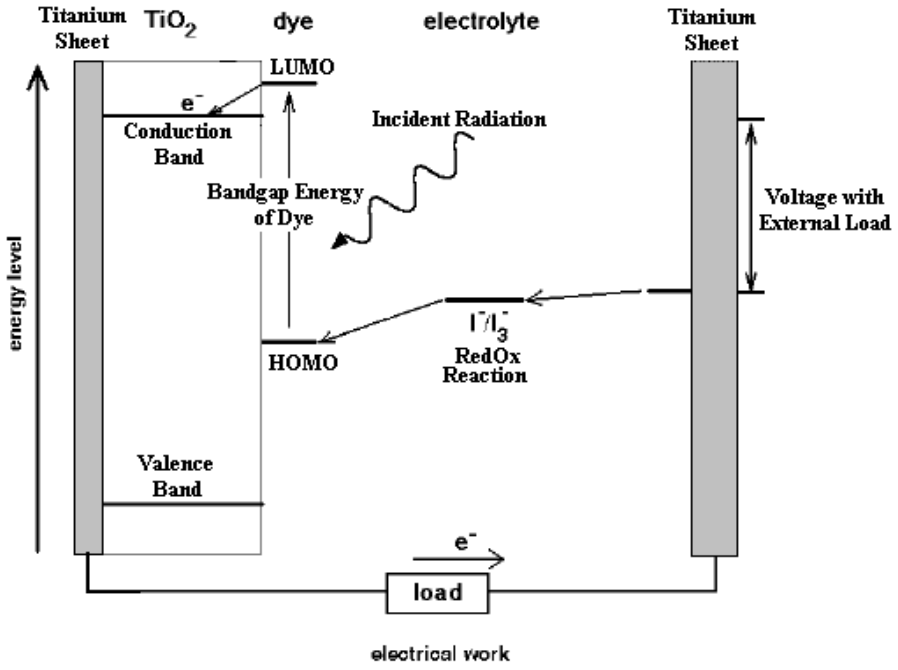

Fig. 8 Electron transport diagram illustrating the bandgap energy in a DSPC.

Ionizing radiation that is absorbed by a DSPC at energies much greater than the bandgap energy will produce secondary electrons and gamma heating before being attenuated enough to excite electrons to the LUMO level. The secondary electrons that are produced by high-energy radiation are beneficial, as they will often appear in the LUMO energy level as they lose energy. However, the gamma heating caused by the slowing down of ionized particles could possibly degrade the photon conversion efficiency of the DSPC. Likewise, absorbed radiation that is at a lower energy than what is required to cross the energy bandgap does not produce LUMO energy level electrons, but instead produces heat and material defects.

In the majority of applications, the incident radiation energy is much higher than that of the material's bandgap energy (near 1 MeV vs. 1-10 eV). Therefore, an intermediary, such as a scintillation material, might be beneficial to attenuate or convert the radiation energy/wavelength to a more appropriate value. Scintillators absorb incident high energy/short wavelength radiation and convert it into lower energy/longer wavelength visible light. This energy conversion process occurs when valence band electrons absorb enough radiation energy that they cross an energy bandgap into an excited state. When returning to the ground state, the scintillation material emits photons of characteristic wavelength in the visible light region (300-700 nm wavelength). A summary of the wavelengths where the peak of the emission spectrum occurs is shown in Fig. 9 for several common scintillator materials, where most of the peaks occur in the narrow visible range between 400-600 nm.

Note that, to improve the probability of visible photon emission during de-excitation, small amounts of an impurity, called an activator, are often added to inorganic scintillators. The activators create special sites in the lattice where intermediate energy states can be created within the forbidden gap. Electrons can then de-excite back to the valence band through these sites with lower energy increments, which give rise to visible photons whose wavelength can be tailor-made to some degree -- that is, it is the activator energy structure within the original crystalline

lattice that determines the primary emission spectrum of the scintillator. This feature gives some flexibility in designing and selecting a scintillator/activator combination to match the absorption spectrum in a particular application. For example, cesium iodide scintillators with both thallium and sodium activators are available, giving emission peaks near 550 nm for CsI:Tl and 420 nm for CsI:Na.

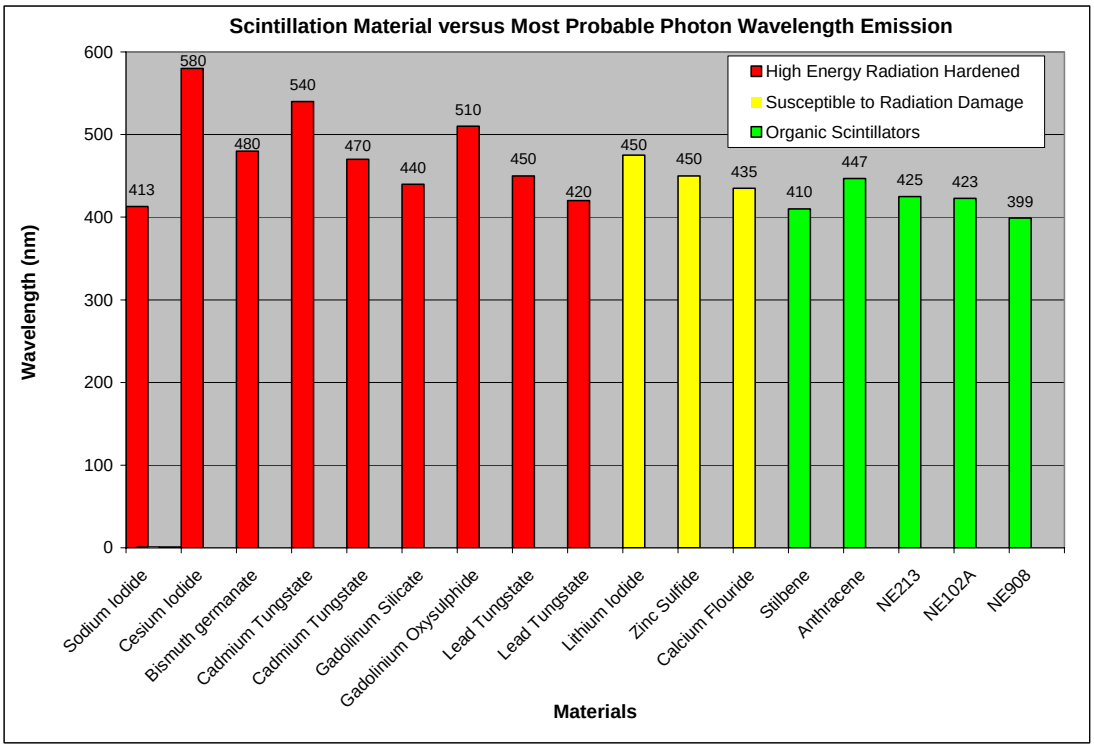

Fig. 9 Photon emission peaks for various scintillation materials.

Scintillator materials are used in a variety of application areas and there are many types having a wide range of characteristics. A brief overview of many of the options available is given in Ref. 9, where the focus is on the use of scintillators for radiation detection and measurement. The ideal scintillator material for use within a gammavoltaic cell must meet many of the same performance criteria as those for other applications, and it will also have to operate over a long period of time in a relatively harsh environment. In particular, the material selected for this application will have to operate within a high-energy gamma radiation field, with dose rates up to 10-15 Krad/hr and a 30-year integrated dose of 1000 Mrad or more. In addition, temperatures up to or exceeding 100 C are also possible. The intense radiation and high temperatures present within the cask will probably eliminate the organic/plastic scintillation materials from consideration. In addition, some crystalline scintillators may also not be very appropriate because of optical defects that can build up under irradiation and the performance degradation that can occur at high temperatures due to decreased bandgap widths. On the other hand, ceramic scintillation materials, which tend to be more radiation and high temperature resistant, are of particular interest for this application.

In addition to being able to withstand the cask environment for a long time period, the scintillation material must also perform well optically in terms of absolute light output and being spectrally matched to the KTI DSPCs. Scintillator light output is typically expressed as an absorbed energy conversion quantity in units of photons emitted per MeV of absorbed radiation energy and this performance measure varies widely among different scintillation materials, as illustrated in Fig. 10.

Other scintillation material performance considerations involve using a high density/atomic number material, which enhances the high energy gamma interaction probability and the photoelectric effect cross section. It should also be noted that in this application, re-absorption of the emitted light by the scintillation material is improbable due to the fact that the scintillation material is in powdered form in a thin film geometry (as opposed to sheet form), which provides a more light-efficient geometry.[10] Also, as a final note, any scintillation material that is considered must not interact chemically with the sensitizing dye or electrolyte within the DSPCs due to the potential for internal cell degradation. In general, selection, testing, and final optimization of the scintillation material for use in the gammavoltaic cell design will become increasingly important in future DSPC design iterations.

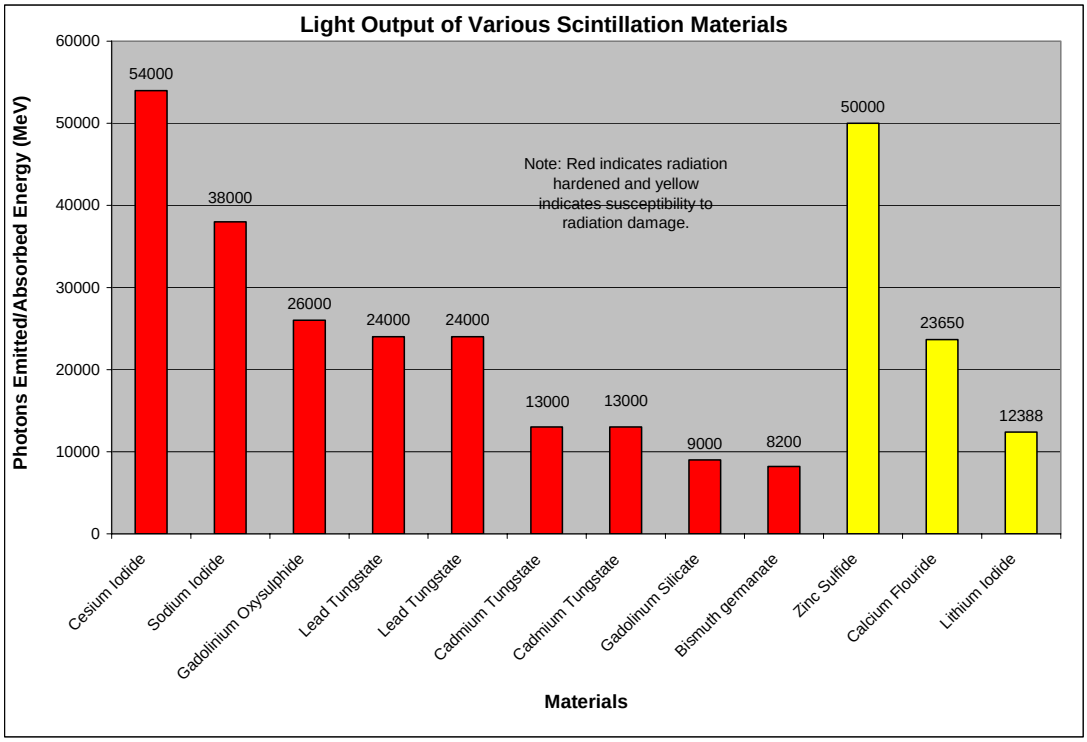

Fig. 10 Optical performance of various scintillation materials.

Based on the above performance parameters, gadolinium oxysulphide (Gadox) was selected as the first candidate scintillation material to evaluate in this research due to the fact that its peak spectral intensity resides in the green visible light region (545nm, 2.28eV), which corresponds to the sensitivity peak of the dye infused titanium dioxide substrate used in the gamma cells, as shown in Fig. 11. Other reasons for testing Gadox as the initial scintillator candidate are its relatively high absolute light output and the fact that the UML Radiation Laboratory had

sufficient quantities of Gadox in stock when DSPC testing began. Certainly there are a number of other potential candidates, but due to time constraints in this initial study, additional selections will be made and investigated in much further detail as part of future DSPC design efforts.

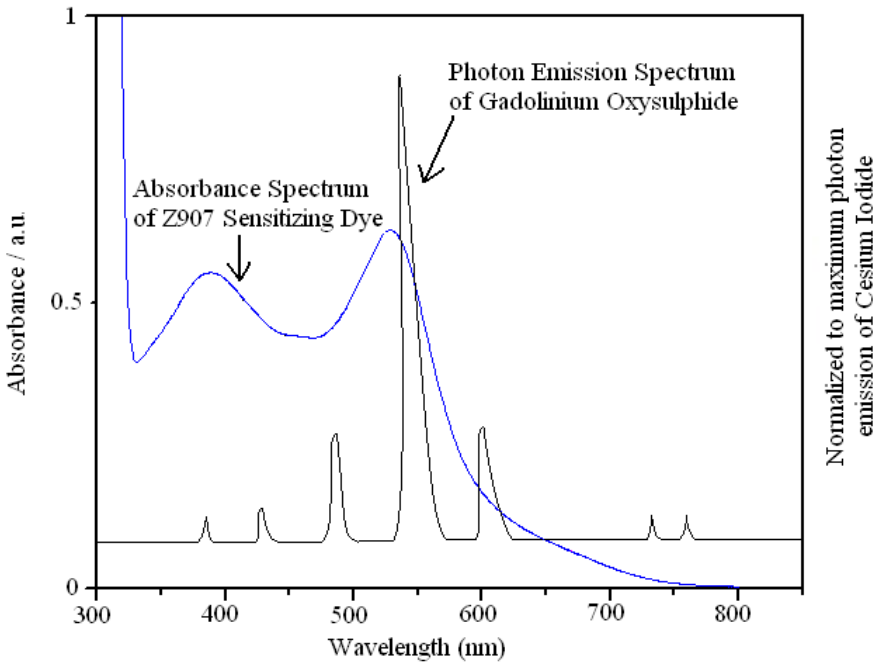

Fig. 11 Spectral matching of Gadox and the Z907 dye used within the DSPCs.

V. Test Setup, Initial Test Results, and Evolution of Different Cell Designs

Actual measurements of the power characteristics for the standard Konarka DSSCs and a series of different gammavoltaic cell designs were made using the Co-60 irradiation facilities within the UMass-Lowell Radiation Laboratory.[11] As with traditional photovoltaic systems, the short circuit current, the open circuit voltage, and the I-V curves were measured under a variety of conditions for the different cell designs. This section of the report gives an overview of the methodology used to characterize the power production capability of the cells, summarizes in general terms some of the test results obtained to date, and gives a brief description of the various cells tested and how the testing program affected the on-going evolution of the current gammavoltaic cell design.

V.1 Testing Methodology

The initial objective of testing the dye sensitized photon converters (DSPCs) was to prove that incident gamma radiation would actually produce useful power in the form of electricity. Once feasibility was established, the emphasis shifted towards quantifying the relative performance of different cell designs. In order to determine the cell performance experimentally, the actual inputs and outputs of the system must be characterized and quantified: the input of the test system being the incident gamma radiation from the Co-60 rack placed in front of the window to

the Radiation Laboratory's gamma cave facility, and the output being the electric power produced by the cells. The gamma radiation incident on the test cells is quantified using alanine pellet dosimetry, while the electrical output is measured using a data acquisition system designed specifically for the current project. An overview of these two systems is explained here to clarify the overall implementation and operation of the testing program.

V.1.1 Radiation Field Calibration

In order to quantify the gamma dose rate (Krad/hr) and actual energy flux (W/m^2) incident on the DSPCs at a given location in the gamma cave, dosimetry readings are taken periodically to verify the Cobalt 60 source strength using alanine pellet dosimetry. Alanine pellet dosimetry operates on the principle that ionizing radiation creates free radicals in the form of unpaired electrons in the amino acid alanine.[12] The effect of the production of free radicals is a shift in the resonance absorption peak of the alanine crystalline structure, which is measured using a spectrometer at wavelengths of 510 or 600 nanometers. The pellet dosimeters are usually distributed in a cross pattern within the lead-aluminum test fixture enclosure, as shown in Fig. 12, in an effort to measure the average dose.

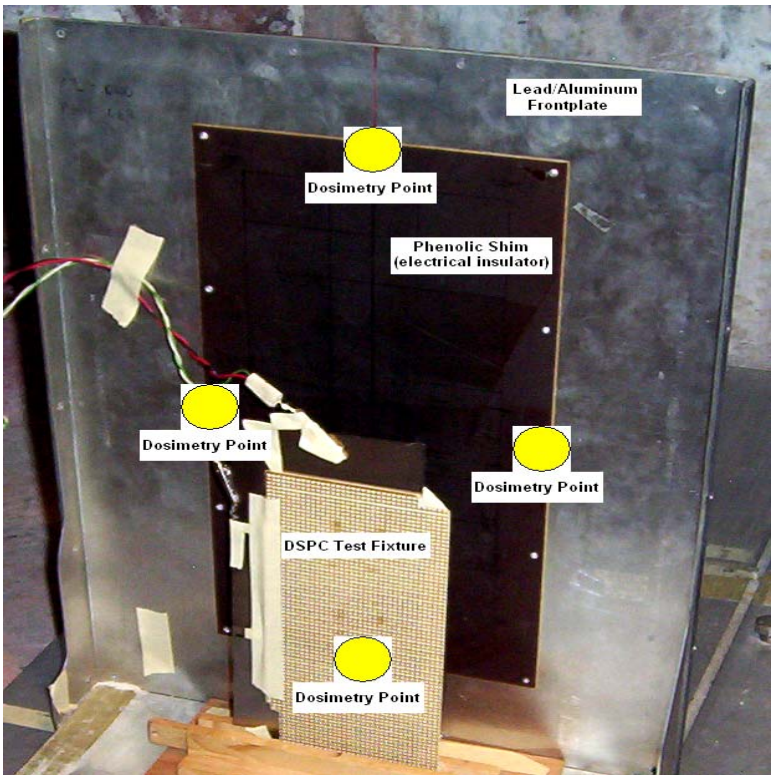

Fig. 12 Illustration of dosimetry point distribution in the lead-aluminum test enclosure.

The reason for using the lead-aluminum test fixture is to achieve charged particle equilibrium (CPE) within the test volume. CPE occurs when the energy transported into a given volume by charged particles is balanced by the energy transported out of the volume by charged particles. It is also worth noting that, when doing calculations, dose is equal to kerma under CPE conditions. CPE would never be established using only the relatively thin DSPC test fixture (approximately 0.125 in. thick) because the range of the secondary electrons created by the ionizing radiation

would exceed this thickness. Consequently, the test fixture would lose more electrons than it would gain, producing a net charge. Therefore the placement of the DSPC test fixture in the lead-aluminum enclosure ensures that the charge is balanced within the test volume, since the secondary electrons produced at the front surface of the enclosure do not have the range needed to escape the back surface of the enclosure.

The NIST-traceable gamma dose rate calibration procedure is performed periodically for each Co-60 rack at a variety of standard locations within the gamma cave (i.e. at varying distances from the source window). Thus, various dose rates can be obtained for different applications by simply choosing an appropriate Co-60 rack and distance to source combination. Note also that, at the time of use, the recorded data are decay corrected to account for the source decay since the calibration date.

The information available from the calibration procedure is given in units of absorbed dose to silicon (Krad/hr). However, for the present work, a more convenient measure of input energy density is the energy flux in units of W/m^2 incident on the test cells. The macroscopic kerma factor for silicon at 1.25 MeV, as obtained from the BUGLE-96 library,[13] is approximately 1.9×10^{-9} Krad/hr per unit photon flux (note that 1.25 MeV is the average of the two discrete gamma photon energies [1.17 MeV and 1.33 MeV] emitted from Co-60). Thus, denoting the measured dose rate in Krad/hr as DR, the incident areal power density in W/m^2, PD_{in}, can be written as

$$PD_{in} = \left(DR\,\frac{\text{Krad}}{\text{hr}}\right)\left(\frac{\gamma/\text{cm}^2-\text{s}}{1.9\times10^{-9}\,\text{Krad/hr}}\right)\left(\frac{10^4\,\text{cm}^2}{\text{m}^2}\right)\left(\frac{1.25\,\text{MeV}}{\gamma}\right)\left(\frac{1.6\times10^{-13}\,\text{J}}{\text{MeV}}\right) = 1.05\,DR\,\frac{\text{W}}{\text{m}^2}$$

Therefore, converting the measured dose rate, DR, into the desired input areal power density, PD_{in}, is straightforward, and this quantity will be used to compute the cell (and module) performance index or efficiency in subsequent analyses (see below).

V.1.2 Data Acquisition System and Test Procedure to Characterize Electrical Performance

The system setup used to measure the electrical output of the DSPCs due to gamma radiation exposure consists of a Keithley 2400 Source Meter Unit (SMU),[14] Labview PC based data acquisition software, and a general purpose interface bus (GPIB) card. The Keithley SMU receives electrical data from the cells under test via a pair of 25 foot twisted leads that are routed through a small penetration in the gamma cave testing facility. The electrical data are then preprocessed by the Keithley SMU and sent to a Labview buffer using the GPIB card. For visual reference, the relative location of the various pieces of data acquisition equipment and the test fixture within the gamma cave is illustrated in Fig. 13 (note that the electrical penetration is off to the side of the gamma cave, not in a direct line-of-sight direction with the Co-60 source).

In order to measure the power output of the DSPCs, a characteristic current-voltage (I-V) curve must be obtained that describes the power handling capabilities of a given device. The preferred method of obtaining an I-V curve is to program the Keithley SMU to source or input a voltage to the device being tested and then require the SMU to also measure and record the current being produced. This method is considerably faster and more accurate than programming the SMU to source current and measure voltage, because of the high capacitive load that is inherent to the DSPCs. The main advantage of using the Keithley SMU is that it allows for the automation of gathering I-V curve information by creating a voltage “sweep” which sources voltage over a

specified range in a predetermined time interval, while simultaneously measuring the current of the device being tested. The GPIB card then allows for two-way communication between the Keithley SMU and the Labview software running on the attached PC.

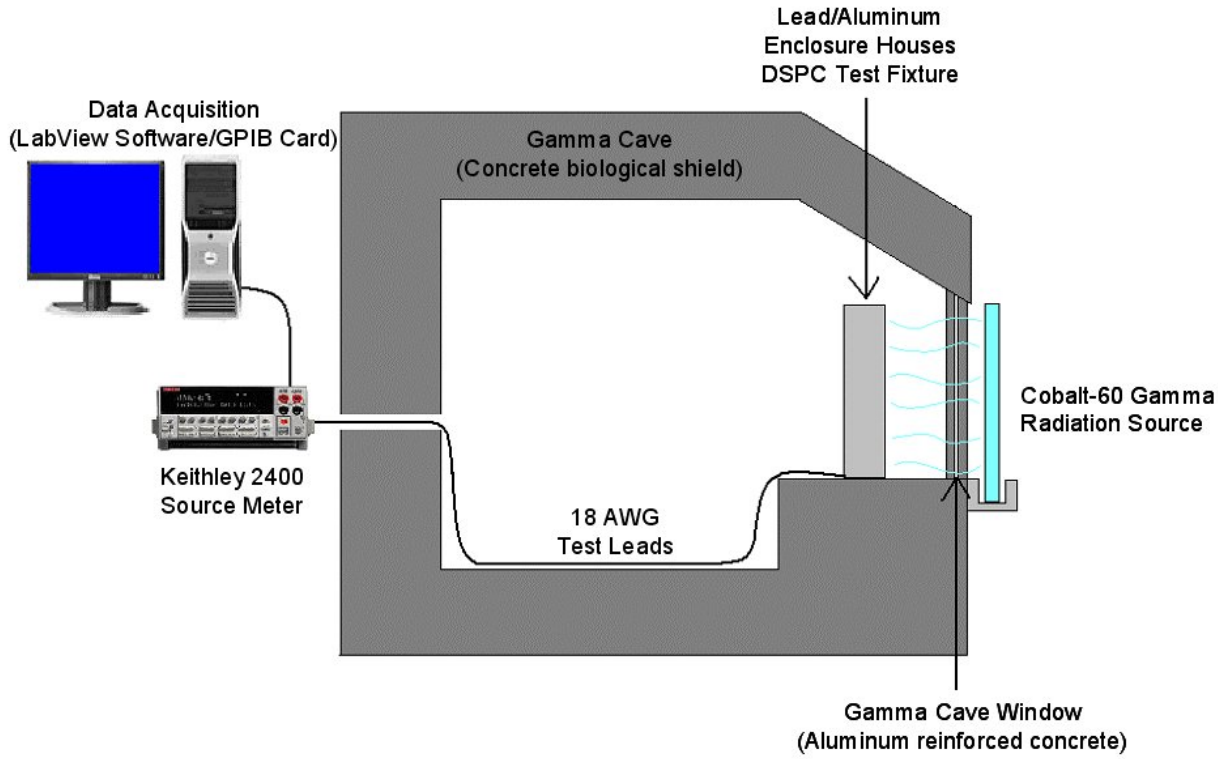

Fig. 13 Relative locations of the test equipment inside and outside of the gamma cave.

The Labview software becomes particularly important when programming the test parameters as well as during data collection from the Keithley SMU. The Labview program selected for this work utilizes a graphical user interface (GUI) that mimics the front manual control panel of the Keithley SMU, as illustrated in Fig. 14. The GUI allows for adjustment of the different voltage sweep parameters used by the SMU including voltage range, voltage increment, voltage settling time (VST), current compliance, number of power line cycles (NPLC), and number of measurements to be made over the specified voltage range. A secondary GUI was added that allows access to some of the finer controls of the SMU, such as the 4-wire resistance compensation circuitry and internal buffer control. The 4-wire resistance compensation circuitry allows for the use of relatively long (25 foot) test leads without sacrificing measurement accuracy. The internal buffer control feature allows the SMU buffer to be reset remotely, as opposed to manually toggling through the Keithley SMU front control panel, after every test to avoid overwriting data. Finally, for preliminary graphical and data analysis purposes, the numerical data gathered in Labview are routed into a Microsoft Excel spreadsheet using a double array output function found in Labview. Eventually the data collected in a series of tests are combined and subsequently processed with a set of Matlab programs written specifically for this project (to be discussed in Section VI).

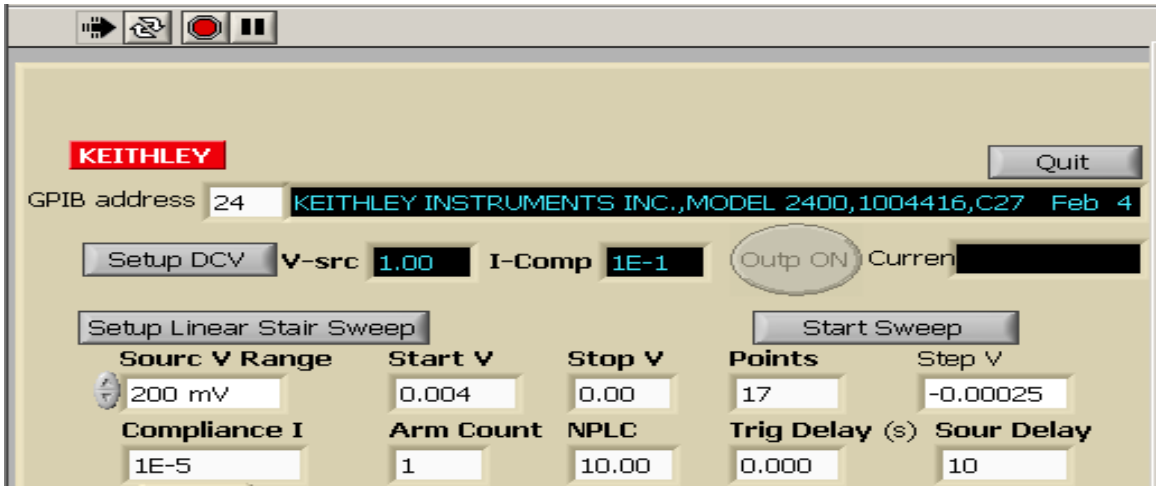

Fig. 14 Main Labview GUI for programming the Keithley 2400 voltage sweep.

When testing, it is important to have the cell power output of sufficient magnitude to overcome the inherent noise and uncertainties in the measured quantities. This was a consistent problem during the early tests because the cells tested were relatively small and only one layer thick. Thus, the gamma interaction probability with these small-area thin-film cells was very low, leading to very low power production. This issue has been alleviated somewhat in the later tests by using cells with a larger base area, by increasing the incident gamma dose rates by as much as a factor of 10 above the expected SNF cask levels, and by placing the cells into stacked series and/or parallel arrays to increase the effective cell volume. When cells are connected in series, their respective open circuit voltages should combine to create a larger voltage potential than with a single cell. Likewise, when cells are connected in parallel, their respective short circuit currents should combine to create more current flow than with a single cell. The disadvantage of manually creating an array of cells from a set of single cells is associated with the added resistance caused by the interconnections between cells. Poorly connected cells lead to resistive power losses, which can negate some of the advantage associated with stacking the cells. In the long term, however, the best way to get a significant increase in power output is to create a single integrated module that has multiple cell layers in series (or parallel) to increase the overall cell volume and the effective interaction probability of the incident gammas.

Finally, after putting the individual cells into a particular test configuration, the cell array is placed in the lead-aluminum enclosure to insure charged particle equilibrium conditions during testing. The whole enclosure is then moved into a position within the gamma cave consistent with previous dosimetry calibrations to achieve the desired target dose rate. After positioning the enclosure and attaching the test leads to the cells under test, the gamma cave is sealed and the light is turned off to avoid the photon contamination that might be caused by the ambient room light source. The cobalt radiation source is then placed adjacent to the gamma cave “window” to create the required gamma radiation field for the test configuration. The cells are then electronically tested with the appropriate voltage sweep parameters programmed into the Keithley SMU using the Labview GUI. The voltage sweep is conducted and the data defining the I-V curve is collected by Labview and subsequently routed into an Excel spreadsheet for processing. This sequence is repeated, as needed, for multiple dose rates (i.e. different locations) and for a variety of different cell types and cell geometries.

V.1.3 Lessons Learned

One problem with initiating a new research project is the learning curve associated with performing the tests and analyses required as part of the overall research effort. For example, for the current project, the Keithley test equipment was utilized to make the I-V traces, but learning how to accurately perform the tests, and then streamline the overall procedure to make testing as accurate and as efficient as possible, required significant effort. In particular, two of the "Lessons Learned" during this process for the current project that deserve mention here concerns the proper choice of the Voltage Settling Time (VST) and the Current Compliance Setting (CCS) on the Keithley unit.

Concerning the selection of the VST, after a series of initial tests that were difficult to interpret and reproduce, it was determined that the voltage settling time (VST) was causing the observed effects. Because of the large inherent capacitance of the dye-sensitized solar and gamma cells, it was discovered, through trial and error, that the VST (i.e. the Sour(ce) Delay in the GUI in Fig. 14) needed to be set to a much larger value than for the standard silicon solar cells (typically as high as about 5 s to 15 s). In order to ensure that the VST setting was no longer a concern, several rounds of cell testing were performed manually without the use of the Keithley 2400 voltage sweep feature. Testing the cells using the manual method involved sourcing a voltage and measuring the resulting current after allowing enough time for the current reading to settle down to its steady state value. A voltage sweep would then be run using the Keithley unit with a VST comparable with what seemed to be necessary to achieve steady state during the manual voltage sweep. A comparison of the two resulting I-V curves was then used to determine if the VST was set for a long enough time interval based on whether or not the automated voltage sweep was within the uncertainty of the manual voltage sweep. This approach allowed the determination of an appropriate setting for the KTI cells, and all the subsequent measurements were much better behaved.

The issue with the Current Compliance Setting was a direct result of the initial problem with the Voltage Settling Time. This concern surfaced when it was discovered that the cells were actually operating in the microampere range as opposed to the milliampere range (which was originally thought to be correct based on erroneous measurements produced by the incorrect VST). The Keithley 2400 has several different current compliance settings, as show in Table 1, for use when making current measurements over different ranges. For example, if one was expecting a peak current of 1.5 mA during a given test, the current compliance setting would be set to 10 mA in order to get the best accuracy range based on the maximum measurement value.

Table 1 Measurement accuracy for different range settings on the Keithley 2400 SMU (from Ref. 14).

Current Range	Measurement Accuracy +/- (%Reading + amps)
1 uA	0.029% + 300 pA
10 uA	0.027% + 700 pA
100 uA	0.025% + 6 nA
1 mA	0.027% + 60 nA
10 mA	0.035% + 600 nA
100 mA	0.055% + 6 uA
1 Amp	0.22% + 570 uA

However, the difficulty with selecting the proper current compliance is that the behavior of the cells is such that, at voltage levels above the open circuit voltage, the current decreases quickly towards negative infinity. A typical I-V curve that highlights this result is shown in Fig. 15 (the I-V curve flattens out after 0.55 volts because the Keithley unit is current limited to 1 ampere).

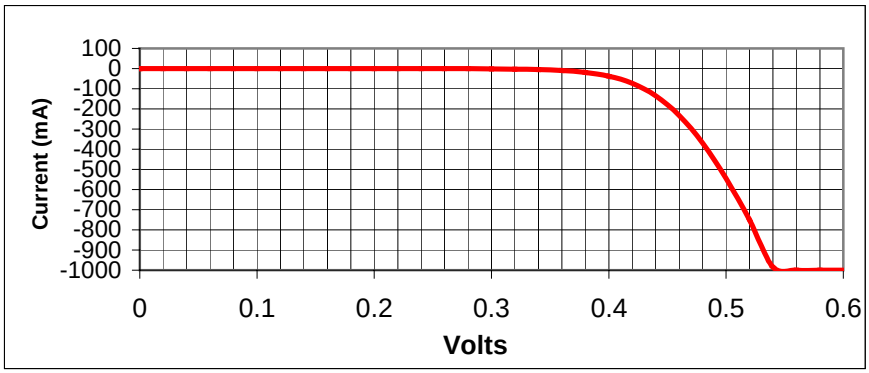

Fig. 15 Typical I-V curve when measurements extend beyond the open circuit cell voltage.

Due to this situation, the testing protocol adopted for this work is to manually source the voltage to determine the exact point where the current changes sign -- this is the open circuit voltage (V_{oc}). For voltages less that V_{oc}, the current is positive, but the magnitude is very low (in the μA range), and an appropriate Current Compliance can be chosen to maximize the accuracy for this range of measured currents. Following this procedure not only allows for the optimum current range to be selected, but it also ensures that all the data points collected are from the power-producing quadrant of the I-V curve.

V.2 Design Evolution and Description of the Cells Tested

Initial testing started with the existing class of solar cells being fabricated at Konarka as part of their continuing research in the design and manufacture of flexible thin-film dye-sensitized solar cells. In addition, a standard silicon solar cell array was also evaluated as a base case. After this startup period, a series of the newly-developed gammavoltaic cells containing two Ti-metal electrodes were fabricated at KTI and tested at the UMLRL (recall that no transparent conductor is needed for operation with gamma photons). Several variations upon the basic metal-metal dye-sensitized photon converter (DSPC) design have been fabricated and tested as part of this project, and the goal of this subsection is simply to overview some of the details of the various designs that have been considered thus far. Towards this end, a summary of some general cell design information is given in Table 2 and a picture showing some of the cells tested thus far is shown in Fig. 16.

The original batch (Cell Set #1) of five solar cells (DSSCs) were constructed with a cathode of sheet titanium that was coated with a 9 micron thick sintered titanium dioxide (TiO_2) layer which serves as the substrate for the light sensitizing dye. The dye is a ruthenium-based complex that is chemically bound to the TiO_2 substrate and promotes light sensitivity over a broader spectrum than the TiO_2 alone. The cells also contained an iodine-based electrolyte that serves as a charge transport medium within the cell via oxidation-reduction reactions involving triiodide/iodine. An

indium tin oxide (ITO) transparent conducting layer represents the cell's anode, and this has a thin layer of platinum catalyst that creates better charge transfer at the ITO/platinum/electrolyte interface than with the bare ITO/electrolyte surface alone. A limitation on the width of the active cell region to 0.7 cm was due to the relatively high surface resistance of the ITO; however the cells could be manufactured to any reasonable length. Thus all of the original ITO/titanium cells were restricted to 0.7 cm width, and the first set of cells tested had about a 1.4 cm^2 - 1.5 cm^2 active surface area.

Table 2 Catalog of cells developed and tested as part of current program.

Cell Set #	Cell Description	Substrate Thickness (μm)	Electrolyte	Active Area (cm^2)	# of Cells*	Status
1	ITO/Ti DSSC	9	Standard	1.5	5	Tested
2	ITO/Ti DSSC	9	Standard	10	5	Tested
3	ITO/Ti DSSC	9	Standard	13	6	Tested
4	Ti/Ti DSPC	9	Standard	30	5	Tested
5a	Ti/Ti DSPC	14	Standard	45	8	Tested
5b	Ti/Ti DSPC, no dye	14	Standard	45	5	Tested
5c	Ti/Ti DSPC, with Platinum	14	Standard	45	2	Tested
6	Ti/Ti DSPC, with scintillator	14	Gadox 150 mg/cm^2	45	2	Tested
7	Ti/Ti DSPC, with glass rods	14	Standard	45	5	Tested
8**	Ti/Ti DSPC, with scintillator, glass rods, and epoxy sealant	14	Gadox	45	8	Future Work

*Note that many of the hand-made DSPC cells were faulty. Thus, the total number of cells characterized within a gamma field is less than indicated here.
**The Set #8 specifications are proposed as the next logical step for future gamma cell development and testing.

As mentioned earlier, the measured current output from the small cells was extremely small -- on the order of nanoamperes -- which lead to measurement difficulties. To help resolve this issue, larger cells were produced, which resulted in two additional sets of the standard solar cell design: Set #2 with an active area of about 10 cm^2 and Set #3 with active areas near 13 cm^2. These series of cells were identical to the first set in chemical composition and construction, except these cells were longer in length, which lead to the larger areas. Unfortunately, the measured currents for these cells were still relatively small and, when these were connected into parallel arrays, the expected increase in the current was not observed -- possibly because of large losses due to poor conductivity at the ITO/ITO junctions.

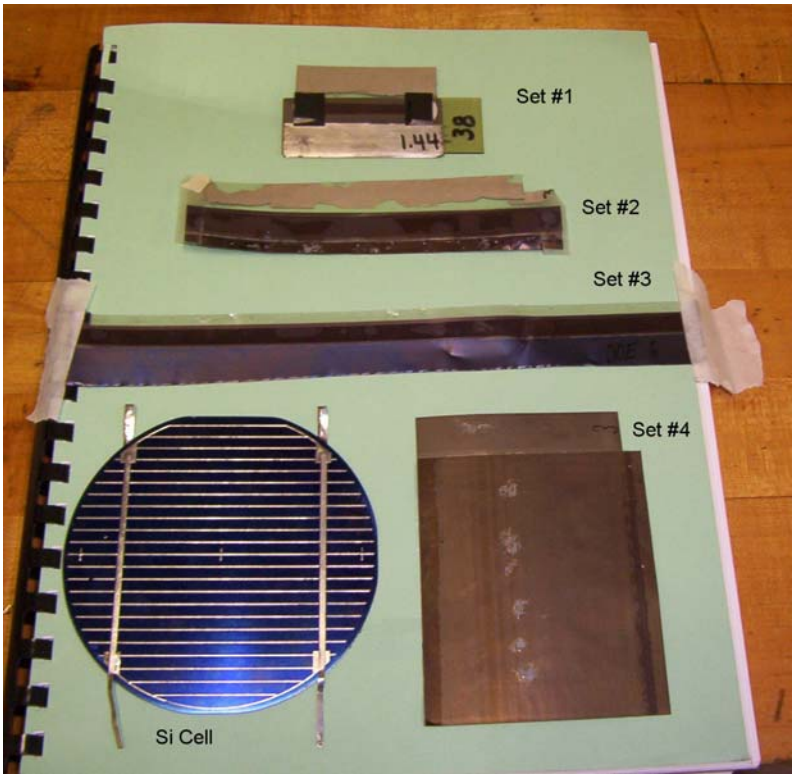

Fig. 16 Photo showing typical cells tested as part of this project.

The next logical step was to remove the ITO completely from the cell design, since a transparent conducting layer is not necessary when the cells are used within in a high-energy gamma photon environment. Thus, all subsequent cells were constructed with sheet titanium on both the anode and cathode sides, and these cells were referred to internally as "gamma cells" (as opposed to "solar cells"). In order to insulate the two titanium sheets, a 25 μm thick Teflon spacer that is 50% porous was placed between cathode and anode -- this allows for electrolyte diffusion but prevents direct contact of the anode and cathode which would cause a shorted condition. The higher conductivity of the titanium anode allows for cell widths up to 5 cm, which is restricted by the current DSSC manufacturing process, not the resistivity of the titanium.

The first five gamma cells (Cell Set #4) that were developed had an active area of 30 cm^2 and allowed for easier array construction due to much larger cell-to-cell contact areas. After some initial testing on these cells was performed, it was decided to produce gamma cells with larger interaction volumes in an effort to increase the signal to noise ratio during testing. The gains in interaction volume were realized by increasing the cell area from 30 cm^2 to 45 cm^2 and by increasing the titanium dioxide substrate thickness from 9 to about 14-15 micrometers. This larger, second generation of gamma cells (Cell Set #5) was produced in three subsets (Sets 5a, 5b, and 5c), which allowed experimenting with using a platinum catalyst coating on the anode and permitted testing identical cells with and without sensitizing dye. In particular, cell Set 5a is identical to Set #4 except for the size differences noted above, Set 5b was produced without sensitizing dye infused in the titanium dioxide substrate, and Set 5c has a platinum-coated anode but is otherwise identical to Set 5a.

The Ti-Ti gamma cells generated for Test Sets #5, in particular, established the viability of the basic gammavoltaic concept. The areal power density produced from these cells was relatively low, but the output response of a given cell configuration increased linearly with the input gamma photon intensity, and the expected additive behavior of the output current and voltage for cells connected in parallel and series was observed. Basically, the results from Cell Set #5 demonstrated that the gammavoltaic cells could indeed produce power from high-energy gamma photons in a predictable and scalable manner -- thus, the primary initial goal of this work had been achieved.

However, the base metal-metal DSPC design is still expected to have its highest conversion sensitivity to optical photons, and the Set 4 and 5 designs did not address this issue (these cells did not contain any scintillator material as part of the cell construction). Based on the expected improvements that a scintillator could offer, and drawing from earlier solar cell test results that indicated an increase in DSSC performance when using an external scintillator, a new cell design that blended a powder form of a scintillation material directly into the gamma cell electrolyte was developed. The resulting gamma cells (Set #6) were produced with a scintillator/electrolyte concentration of 1:1 by weight using powdered Gadox (gadolinium oxysulphide). Gadox was selected as the initial scintillation material to test due to its availability and to the fact that its peak emission spectral intensity resides in the green visible light region (545nm, 2.28eV), which corresponds to the high sensitivity region of the dye infused titanium dioxide substrate used in the gamma cells.

One of the issues associated with the development of the gamma cells concerns the reliability and consistency of the manual cell fabrication process. Since the development and fabrication of the current generation of gamma cells represent one-of-a-kind processes, everything is done by hand -- that is, because of the unique nature of each cell, this work could not take advantage of KTI's automated manufacturing process for their standard product line. In particular, the sequence of steps involved in the bench-top cell preparation process for Sets 4-6 was as follows:

1. A titanium foil is coated with TiO_2 and a polymer binder and then sintered with a stepped-ramped temperature profile.
2. A ruthenium dye complex is applied and the dye is adsorbed onto the titanium dioxide, turning the TiO_2 a purplish color.
3. A polymer-based adhesive is placed in a four-sided window-frame arrangement on the outer rim of the sintered/dyed Ti foil.
4. A porous spacer material is placed inside the active cell window area to act as an insulator between the two titanium sheets.
5. The electrolyte is applied and allowed to thoroughly soak the porous insulator.
6. Finally, the second Ti foil (which may contain a sputtered Pt catalyst) is applied as the counter electrode and this is attached to the cell via the adhesive window frame at an elevated temperature for several seconds.

Although this procedure sounds straightforward, hand preparation of the cells is somewhat of an art, and good reproducibility from cell to cell was hard to achieve. In particular, several of the cells produced this way were faulty (shorted) and the measured power characteristics of the good cells varied considerably. The large variability, in particular, was thought to be associated with a possible uneven distribution of the electrolyte throughout the active area (with the possibly of

some dry spots), which would lead to reduced electron transport and less efficient operation of the cell.

In addition, some preliminary integrated dose testing on Cell #1 in Set #5 revealed cell performance degradation to the point of total cell failure before reaching the 150 Mrad total integrated dose (TID) point. The Teflon insulation material was suggested as the reason for this premature failure as it has been shown to degrade quickly under irradiation.

Thus, to address some of these concerns, another gamma cell iteration was produced (Cell Set #7), this time with 10 μm diameter borosilicate glass beads blended into the electrolyte at a concentration of 0.2 weight percent of the total electrolyte. The glass beads would act as an insulated spacer between the two electrodes, allowing the elimination of the Teflon insulation material. At the same time, a slightly different fabrication procedure was developed to try to reduce the initial cell failure probability and the variability among cells of identical structure. In particular, the four-sided adhesive window frame was eliminated in favor of a three-sided U-shape frame, and the second Ti electrode was put in place before adding the electrolyte to the cell. Once the three sides containing the adhesive were sealed, the volume between the electrodes was uniformly filled with the electrolyte-bead mix through the open fourth side using a syringe. This approach allowed the electrolyte to be inserted under some pressure (instead of by simple diffusion through the porous Teflon layer) to give it a more even distribution. Finally, the fourth edge of the cell was cleaned, an insulating adhesive was added, and this side was sealed to prevent leakage of the electrolyte material.

The new cell preparation process used for Set #7 appears to have been somewhat successful, since only one cell out of five was faulty on initial evaluation, and the remaining four cells showed very good uniformity during the power characterization tests (see detailed results in Section VI). However, this set of gamma cells also showed some degradation under long-term irradiation, and one cell failed (Cell #4) at approximately the same total integrated dose as the previous one with the Teflon insulator (Cell #1 in Set #5a). The exact cause of failure of Cell #4 in Set #7 is not certain, but the current focus is on the polymer adhesive used to bond the two electrodes of the gamma cell together and also insulate the cell around its perimeter. Adhesive failure with increasing integrated dose would lead to the electrolyte leaking out of the cell as well as loss of electrical insulation, thus prohibiting any voltage potential from being generated -- and this is exactly what was observed in the integrated dose testing of some of the Set #7 cells. A general result of this observation is that all polymer-based materials should be eliminated from any future gammavoltaic cell designs, since it is well known that most polymer-based materials do not stand up well to a large gamma fluence.

Clearly it makes sense that the specifications for any future gamma cells should incorporate the lessons learned from the test results from the current study. In particular, it is proposed that the next evolutionary set of cells (i.e. Set #8 in Table 2) should utilize radiation hardened epoxy seals combined with glass rods for insulation and a Gadox blended electrolyte to enhance cell efficiency. This choice of features for the next design iteration (epoxy seals, glass beads, and an internal scintillator material) is shown schematically in Fig. 17. Of course, the details (such as the concentrations at which the insulating glass rods and Gadox scintillator are added to the electrolyte) for the next cell design will have to be worked out as part of future work. However, upon development and testing, it is predicted that the next gammavoltaic design iteration (Set #8) will bring this overall design effort one step closer to the development of a practical device based on this new power conversion concept.

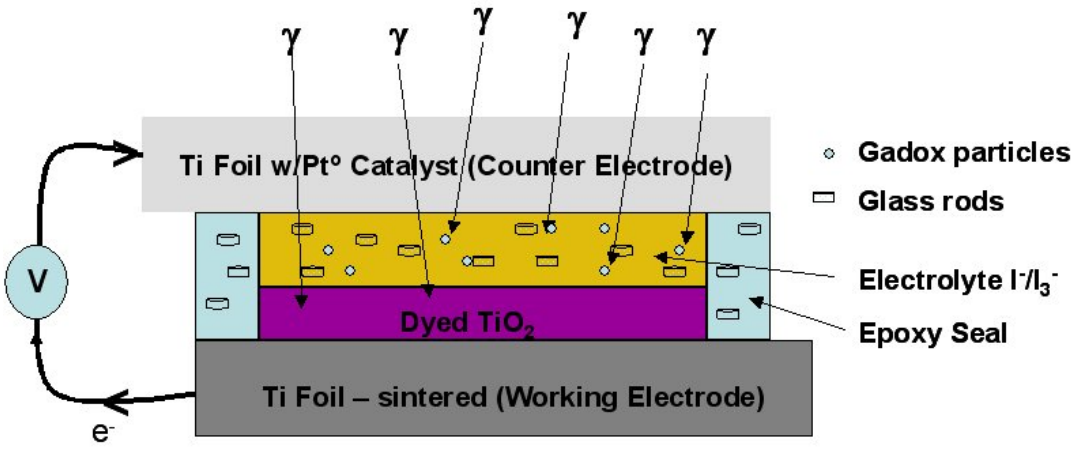

Fig. 17 Sketch showing proposed features for the next cell design (future work).

VI. Presentation of Primary Test Results

Several generic observations from the testing program have already been summarized in the previous section. This section elaborates on these points somewhat and it presents the actual data that lead to these observations. Furthermore, a number of additional analyses, comparisons, and conclusions are made.

The primary test results are organized and presented in a fashion that highlights a particular feature, such as the linear behavior of power production versus dose rate, the additive nature of current when the cells are connected in parallel, the gain in efficiency when a scintillator material is used, etc. As such, the same data for several of the cells may be repeated a number of times to help facilitate the illustration of a particular feature of interest.

Overall, there has been a large amount of data recorded during testing of the various cells studied as part of this research program. To help organize, compare, and present these data, a series of Matlab programs were written to summarize the data from a single test sequence (which typically involved three different dose rate points) and to compare data from different tests. The results presented from a single test include the standard I-V curves at each dose rate and a plot that shows the behavior of the peak power and cell or array efficiency, η, versus dose rate. In addition, a table summarizing several important parameters versus dose rate is given, which includes the short circuit current, I_{sc}, the open circuit voltage, V_{oc}, the fill factor, FF, which is defined as the ratio of P_{max} to $I_{sc} \times V_{oc}$, etc. When comparing multiple tests, these same data are presented for a single dose rate point, where the data presented here include the I-V curves and a graphical representation that compares I_{sc}, V_{oc}, FF, and η for the particular tests of interest.

Before showing the actual data, a note concerning the evaluation of the relative cell performance may be appropriate. In particular, one usually defines the efficiency of a solar cell as the ratio of the maximum electrical power density output from the cell to the power density input as solar irradiance. Since the geometry of interest is really two-dimensional for solar cell applications, these power "densities" are evaluated as power per unit area. Thus, the cell efficiency is simply

$$\eta = \frac{\text{max electrical power output per unit area}}{\text{input power per unit area}}$$

where the electrical output power is given by the product of current and voltage ($P_e = I*V$) at the maximum power point, and the input power density is the incident solar irradiance (typically given in W/m^2). This is the quantity that is usually presented as a measure of cell performance for solar cells.

Essentially the same definition as above is also used for the gammavoltaic cells under investigation here, but with added emphasis that the efficiency for a single cell is expected to be very low. In particular, since the gamma interaction probability for a single thin-film gammavoltaic cell is so low, most of the incident energy flux simply passes through the cell without interaction, with little conversion of the incident energy to useful power. For spent nuclear fuel (SNF) monitoring applications, however, many thin-film cells will be stacked or layered to produce a cell volume with some appreciable overall cell thickness, and this will be an important design variable in the final gammavoltaic energy conversion unit. Thus, the efficiency, η, for the gamma cell modules will be a strong function of the number of cell layers present in the full module, where an actual unit employed for SNF monitoring applications could contain as many as several hundred layers. Note, however, for the testing completed so far, only one or two layers have been used -- so the recorded efficiencies were indeed expected to be very low.

VI.1 Actual Results and Observations

With this background, many of the key results and observations from this work are presented below. These are separated into several short subsections that display and briefly discuss the particular feature of interest. The reader should refer back to Table 2 in the previous section, as needed, for a description of the different test sets discussed here.

VI.1.1 Proof of Concept -- Linear Behavior of Power Versus Dose Rate

The measurements associated with Cell Set #5 were the first set of tests that produced consistent, repeatable results. By this time, the testing program had identified and resolved several issues, and the cells were now large enough so that the measured current signal from a single cell had good signal-to-noise characteristics. Three of the cells produced for Set #5a, in particular, saw a full set of tests. Cell #3 in this set gave the best performance and some summary results for a test performed on 3/08/2005 are given in Fig. 18. As mentioned above, this figure has the standard set of results recorded for a single test with three individual dose rate points. The dose rates start at about 20 Krad/hr and go to about 120 Krad/hr, which is about a factor of 10 greater than the expected radiation environment in a typical SNF cask. This range was chosen for the experimental program here to give reasonable measured current levels for a single thin-film gamma cell -- lower values than about 20 Krad/hr lead to some of the measurement difficulties mentioned earlier.

As apparent in Fig. 18, the familiar I-V curve was obtained, with the measured current level increasing with increasing dose rate (input power level). The maximum power point of each curve was recorded and this is plotted versus dose rate in two ways: directly as peak power versus dose rate and as part of the module efficiency versus dose rate, where $\eta = PD_{out}/PD_{in}$. For the efficiency expression, the output areal power density, PD_{out} is computed as the ratio of

the peak power and the cell area exposed to the gamma photon beam. The input power density, PD_{in}, was measured via alanine pellet dosimetry as previously discussed. Finally, a number of tabulated parameters for each dose rate point are also given in the lower half of the figure.

The two most important results from the data in Fig. 18 are that measurable power is indeed produced by the gammavoltaic cell and that the output power is linear with dose rate. The power level is quite low (<1 μW), but this was an expected result for an un-optimized single cell with a total thickness of only about 0.01 cm, since there is very little interaction with the incident high-energy gammas. This, of course, also leads to the recorded low efficiency shown in the figure (that was also expected).

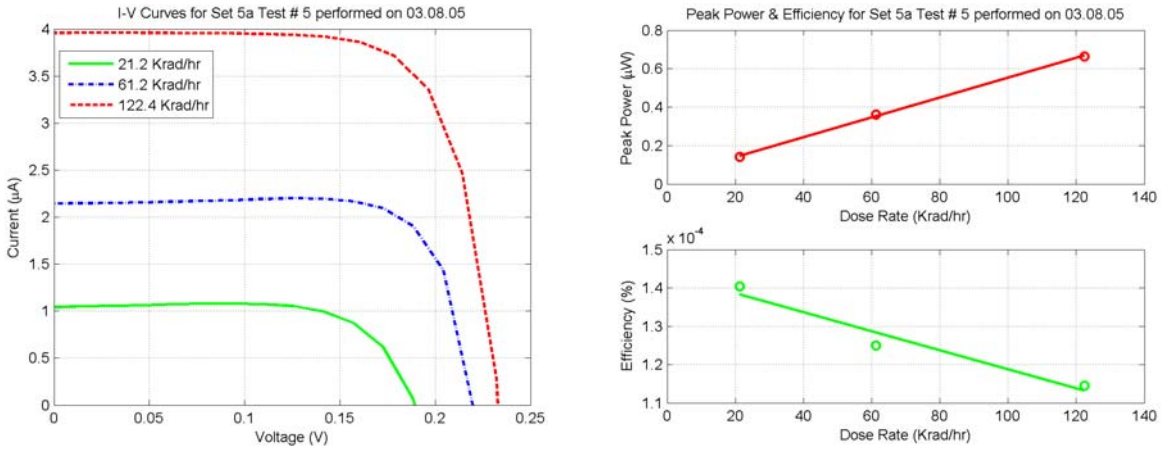

Summary Results from Test # 5 for Cell Set 5a

```
Set Description:  Ti-Ti cells (45 cm^2 & 15 micron TiO2 layer) with dye
Test Description: Single cell (Cell 3) on 03.08.05
Test Date:        03.08.05
Test Status:      GOOD Data

Basic Test Parameters
  Number of cells used:                          1
  Array volume (cm^3):                       0.616
  Beam area (cm^2):                           45.0
  Effective thickness (cm) of array:        0.0137
  Average integrated dose (Mrad):              0.0

Array Performance vs. Dose Rate
  Parameter of Interest      21.2 Krad/hr  61.2 Krad/hr  122.4 Krad/hr
Max electrical power (uW):       0.1413        0.3625        0.6640
Short circuit current (uA):      1.0460        2.1470        3.9630
Open circuit voltage (V):        0.1893        0.2199        0.2329
Fill factor (unitless):          0.7135        0.7678        0.7194
Current at Pmax (uA):            0.9984        2.0980        3.7180
Voltage at Pmax (V):             0.1415        0.1728        0.1786
Module Efficiency (%):         0.000140      0.000125      0.000115
```

Fig. 18 Illustration showing linearity of power versus dose rate for Cell #3 in Set #5a.

Although the cell behaved generally as expected, it was necessary to experimentally quantify the actual current and voltage levels for the given dose rates, since there was no way to predict the actual levels that would be obtained. Thus, this set of experiments gave the desired proof of concept for the basic gammavoltaic principle, and it gave a base level of performance for the first generation of gamma cells generated here.

VI.1.2 Cell Consistency -- Set #5a Versus Set #7

As noted previously, there was a change in the bench-top cell preparation procedure between the production of the Set #6 and Set #7 cells. This was in response to the observed relatively wide variation in performance among cells of the same batch. This inconsistency is seen clearly in Fig. 19 for three cells from Set #5a (Cells 1, 3, and 6). However, also shown here is the good consistency observed with four different cells from Set #7 (Cells 1, 3, 4, and 5). As apparent, the I-V curves for the four different cells from Set #7 are tightly grouped, with similar values for I_{sc}, V_{oc}, FF, and η. On the other hand, the Set #5a cells vary considerably, with more than a factor of two difference in many of these parameters, including the overall cell efficiency. Thus, it appears that the change made in the cell preparation procedure was indeed successful in producing better consistency in performance among cells of the same batch.

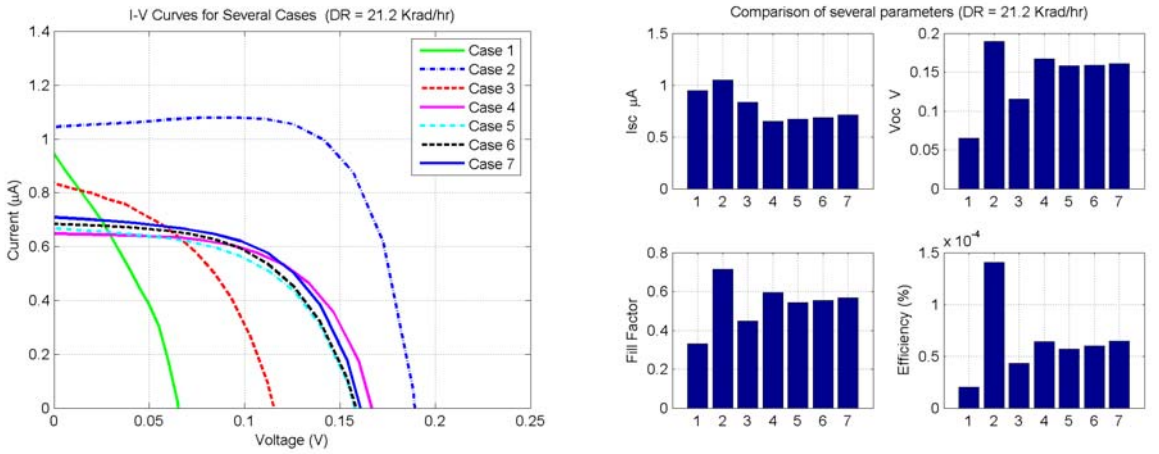


```
Legend for data sets in plots:
   Case 1.  Set 5a Test 2:  Single cell (Cell 1) on 02.16.05
   Case 2.  Set 5a Test 5:  Single cell (Cell 3) on 03.08.05
   Case 3.  Set 5a Test 6:  Single cell (Cell 6) on 03.08.05
   Case 4.  Set 7 Test 1:  Single cell (Cell 1) on 4.1.05 TID = 0Mrad
   Case 5.  Set 7 Test 4:  Single cell (Cell 3) on 4.1.05 TID = 0Mrad
   Case 6.  Set 7 Test 7:  Single cell (Cell 4) on 4.1.05 TID = 0Mrad
   Case 7.  Set 7 Test 10:  Single cell (Cell 5) on 4.1.05 TID = 0Mrad
```

Fig. 19 Effect on cell consistency with the change in cell preparation procedure.

Although the cells from Set #7 behave more consistently, it was Cell 3 in Set #5a that gave the best overall performance. The replacement of the Teflon insulation with very small glass rods as the insulator between the two electrodes should be the only fundamental difference in the Set #5a

and Set #7 designs, and this single design change should not, by itself, lead to a significant change in performance. An improvement in cell consistency was expected due to the change in the cell preparation procedure, but it is not clear, at this point, why Cell 3 in Set #5a performed so well relative to the other cells. Unfortunately, because of the wide variation in performance for the Set #5a cells, the root cause of this behavior may never be determined.

VI.1.3 Scalability -- Series and Parallel Configurations

Beyond initial proof of concept, the most important feature that required demonstration was scalability. Clearly, the power production capability of a single cell, by itself, is too small to be of practical importance. However, if many such cells are connected together, then useful power levels may be achievable. In particular, when two identical cells are connected in series, the open circuit voltage, V_{oc}, for the combination should be essentially twice the single cell V_{oc} value. Likewise, when two cells are connected in parallel, the composite short circuit current, I_{sc}, should be nearly the sum of the I_{sc} values for the two individual cells.

Various series and parallel combinations were tested to demonstrate this thesis. In particular, Cells 1 and 3 and Cells 4 and 5 from Set #7 were paired together in both series and parallel combinations and the results of these two-cell tests are summarized in Fig. 20 for Cells 1 and 3 and in Fig. 21 for Cells 4 and 5. Clearly, as seen in both figures, the actual behavior is essentially as predicted, with the performance of the two-cell combinations showing the expected additive behavior of the series and parallel array arrangements. This scalability feature of the cells is exploited in a subsequent subsection to predict the cell configuration for an actual gammavoltaic power conversion unit for use within a SNF cask environment (see Section VI.2).

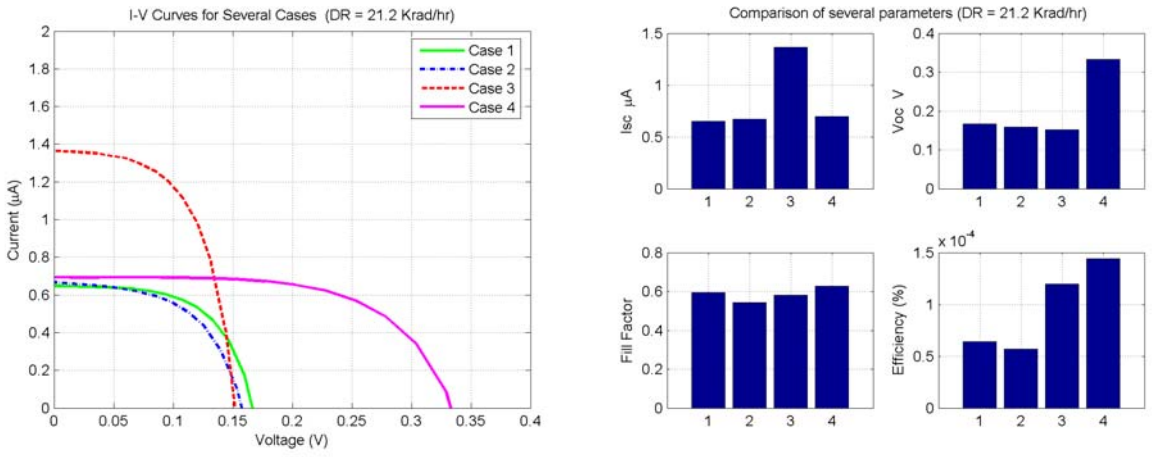


```
Legend for data sets in plots:
 Case 1.  Set 7 Test 1:  Single cell (Cell 1) on 4.1.05 TID = 0Mrad
 Case 2.  Set 7 Test 4:  Single cell (Cell 3) on 4.1.05 TID = 0Mrad
 Case 3.  Set 7 Test 14: Cells 1,3 Stacked Parallel Array 4.4.05 TID = 0Mrad
 Case 4.  Set 7 Test 19: Cells 1,3 Stacked Series Array 4.4.05 TID = 0Mrad
```

Fig. 20 Series and parallel configurations using Cells 1 and 3 from Set #7.

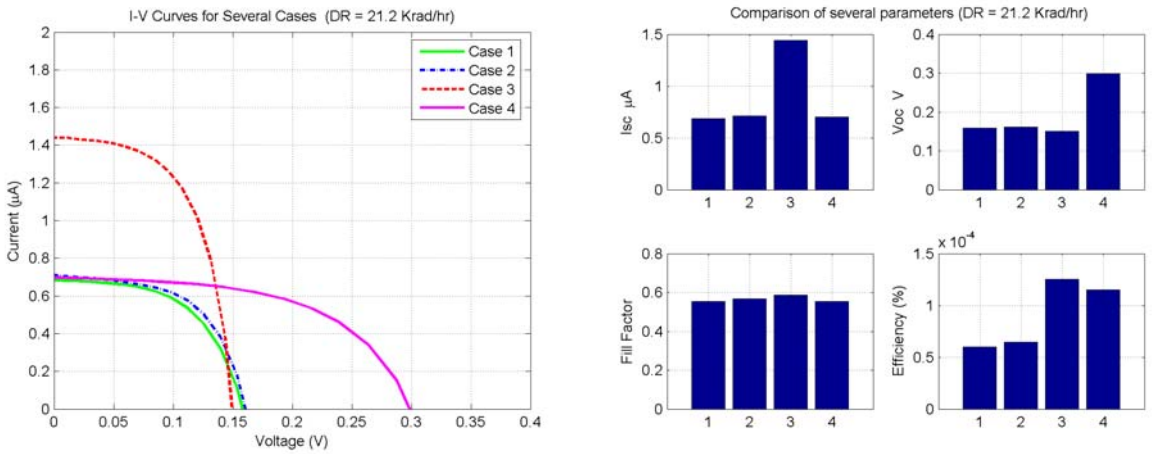


```
Legend for data sets in plots:
 Case 1.  Set 7 Test 7:  Single cell (Cell 4) on 4.1.05 TID = 0Mrad
 Case 2.  Set 7 Test 10: Single cell (Cell 5) on 4.1.05 TID = 0Mrad
 Case 3.  Set 7 Test 24: Cells 4,5 Stacked Parallel Array 4.4.05 TID = 0Mrad
 Case 4.  Set 7 Test 29: Cells 4,5 Stacked Series Array 4.4.05 TID = 0Mrad
```

Fig. 21 Series and parallel configurations using Cells 4 and 5 from Set #7.

VI.1.4 Repeatability of the Test Results

One important aspect of any testing program is repeatability -- that is, can a particular set of measurements be repeated with reasonable consistency? Several checks to validate the repeatability of the testing procedure have been performed over the course of this study. One particular check, as shown in Fig. 22, measured the performance of the series and parallel combinations of Cells 1 and 3 and Cells 4 and 5 from Set #7 on two separate dates. Although all the comparisons are not perfectly matched, it is clear that the same basic information about the cells was obtained on both days of testing. The small uncertainties observed here are typical, and they are quite acceptable for the current testing phase of this study.

VI.1.5 Cell Performance with an Internal Scintillator Material

As discussed previously, it is expected that the final optimized design of the gammavoltaic cell will include a scintillator material blended directly within the electrolyte material. The purpose of the scintillator is to better match the photon spectrum to the peak sensitivity of the dye-sensitized TiO_2 substrate within the cell. As a test of the utility of this design feature, the cells within Set #6 were constructed with Gadox as the scintillator material in a 1:1 weight ratio with the standard electrolyte. Unfortunately, however, only one of the two Set #6 cells was usable, leaving only one cell to test the benefit of including the Gadox scintillator.

Since Set #6 and Set #5a were similar cell designs, except for the addition of the Gadox scintillator, it makes sense to compare the performance of these two cell sets. However, of additional concern here is the inconsistency of the Set #5a cell performance (as discussed previously). Nevertheless, since these are the only data available at this time, Fig. 23 does indeed compare the relative performance of Cell #1 in Set 6 to Cells 1, 3, and 6 in Set 5a.

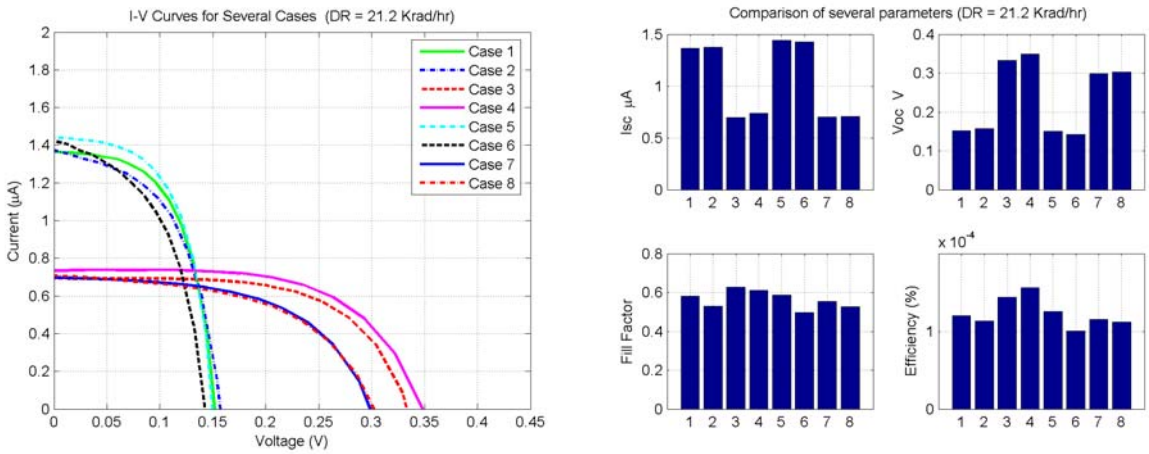


```
Legend for data sets in plots:
 Case 1. Set 7 Test 14: Cells 1,3 Stacked Parallel Array 4.4.05 TID = 0Mrad
 Case 2. Set 7 Test 15: Cells 1,3 Stacked Parallel Array 4.12.05 TID = 0Mrad
 Case 3. Set 7 Test 19: Cells 1,3 Stacked Series Array 4.4.05 TID = 0Mrad
 Case 4. Set 7 Test 20: Cells 1,3 Stacked Series Array 4.12.05 TID = 0Mrad
 Case 5. Set 7 Test 24: Cells 4,5 Stacked Parallel Array 4.4.05 TID = 0Mrad
 Case 6. Set 7 Test 25: Cells 4,5 Stacked Parallel Array 4.12.05 TID = 0Mrad
 Case 7. Set 7 Test 29: Cells 4,5 Stacked Series Array 4.4.05 TID = 0Mrad
 Case 8. Set 7 Test 30: Cells 4,5 Stacked Series Array 4.12.05 TID = 0Mrad
```

Fig. 22 Example showing the repeatability of the current testing procedures.

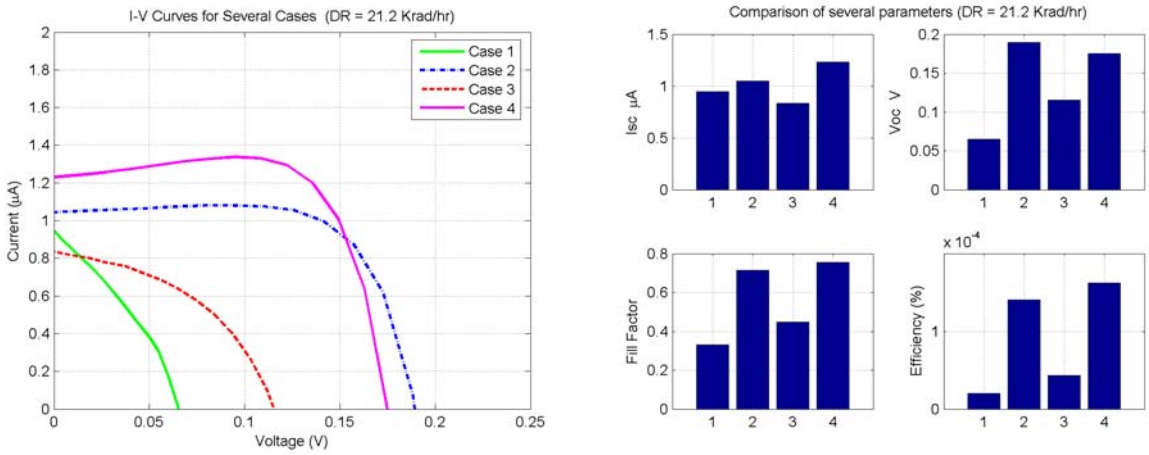


```
Legend for data sets in plots:
   Case 1.  Set 5a Test 2:  Single cell (Cell 1) on 02.16.05
   Case 2.  Set 5a Test 5:  Single cell (Cell 3) on 03.08.05
   Case 3.  Set 5a Test 6:  Single cell (Cell 6) on 03.08.05
   Case 4.  Set 6 Test 1:  Single cell (Cell 1) on 03.08.05
```

Fig. 23 Comparison of cell performance with and without an internal scintillator.

As apparent, especially from the efficiency measure, the single functional cell in Set 6 was the best cell in the group (by about 10% or so over Cell 3 in Set #5a). In fact, this cell gave the best performance of all the cells tested thus far in this program. This result is encouraging, since increased performance was expected from cells with an internal scintillator present. However, because of the variability in performance from cell to cell prior to the development of Set #7, and the fact that there is only one working cell with the Gadox scintillator, it is difficult to quantify the expected gain to be achieved from the additional scintillator material. For example, what if the result from the single cell with Gadox represents a cell that was poorly made, with overall performance on the low end of what really could be achieved? Under this scenario, the improvement seen here is on the low side of what could be expected in general. The counter argument is, of course, what if the measured data given here are on the high side of what can be expected? Then, the overall conclusion would be quite different, with only a marginal increase in expected performance gain from the Gadox-loaded cell. Clearly, the bottom line here is that there are simply not sufficient data available to obtain quantitative evidence of the expected efficiency gain. Thus, the best that can be stated at present is that the results are encouraging, and that more experimental evidence is needed before any quantitative conclusions can be made. One of the goals of the proposed Set #8 cell design is to incorporate a Gadox internal scintillator in order to generate additional data associated with scintillator performance (this will be one of the first issues addressed in any future projects that continue this initial work).

VI.1.6 Preliminary Evaluation from the Integrated Dose Test Program

Another important question that needs to be addressed in detail concerns the expected service life of the gammavoltaic cells. The computations performed for the particular spent nuclear fuel (SNF) storage cask studied in this work predicted that a total integrated dose of well over a 1000 Mrad may be required for a service life of 30 years. This is a severe requirement for any electronic device, and this performance specification for the gammavoltaic cells will not be easy to achieve. In particular, it is expected that optimizing the design to maximize the actual service lifetime will be one of the most challenging aspects of this overall research effort.

Thus, although the current generation of gamma cell designs has not been specifically optimized with service lifetime as a key issue (needed to demonstrate power conversion feasibility first), a first preliminary look at how performance degrades versus exposure and where failure can be expected for the current cell design has already been initiated as part of the current study. In particular, since there were four consistent cells in Set #7 that were tested extensively at zero total integrated dose (TID), these same cells were selected for irradiation over an extended period of time to evaluate their performance versus TID. All four cells have been irradiated, at intervals of roughly 30 to 60 Mrad, to total exposures of about 150 to 180 Mrad and, after reaching 180 Mrad, Cell #5 was placed in a particularly large gamma field until an integrated dose of about 780 Mrad was achieved. After performance testing with a TID = 780 Mrad, Cell #5 was sent to the UMass-Lowell Materials Characterization Lab for testing using various microscopic characterization techniques (see discussion in Section VI.4).

All the cells showed significant degradation versus exposure and, unfortunately, Cell #4 completely failed at the 150 Mrad point. At failure, the cells are effectively shorted. Also, for the current cell design (that uses a polymer-based adhesive around the cell periphery), physical degradation of the seals was apparent in all cases, with actual leakage of the liquid electrolyte in some of the cells.

The measured performance behavior of the cells versus total integrated dose (TID) is highlighted in Fig. 24, Fig. 25, and Fig. 26. In particular, Fig. 24 shows the maximum power output versus exposure for each of the four cells (excluding the one data point at 780 Mrad for Cell 5) at a dose rate of 21 Krad/hr. Both the actual measured points and a quadratic curve fit are given so that the general downward trend of power output is emphasized, clearly noting the gradual degradation of the overall cell performance with exposure. If these curves are extrapolated beyond the 150-200 Mrad range, it appears that a very significant drop-off in performance would occur.

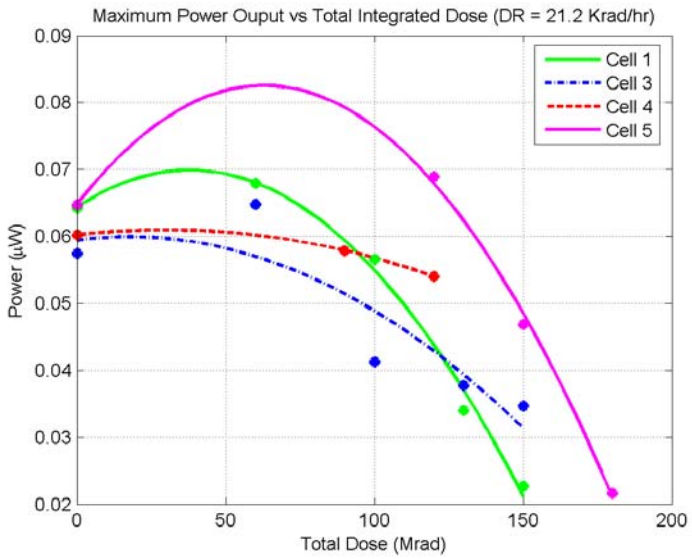

Fig. 24 Output power versus exposure for four cells in Set #7.

However, the trend indicated in Fig. 24 may be somewhat misleading, and further detail and insight are given in the various curves shown in Fig. 25 -- which include the single large exposure point associated with Cell 5. In particular, the I-V curves for Cells 1 and 5 at a dose rate of 21 Krad/hr, each at five different values of TID, are shown in the upper portion of the figure. Then, in the lower portion, all 18 measurement points to date for this dose rate are used to show the general behavior of I_{sc}, V_{oc}, FF, and η versus exposure for all four cells combined. And, although there is only one data point beyond an exposure level of 180 Mrad, these data seem to suggest that the performance degradation may reach some saturation level, with little additional performance loss with exposure after this point. A possible argument for this saturation theory may be related to the shape of the I-V curve and the behavior of the fill factor versus exposure.

First, one should note that the general shape of the efficiency versus dose curve is very similar to the peak power versus TID curves in Fig. 24 in the TID < 200 Mrad range. Here one sees that both the efficiency and peak power increase slightly at low dose and then drop as the TID increases. This same trend is also observed for the short circuit current, I_{sc}. Along with these changes, one also sees that the open circuit voltage, V_{oc}, decreases somewhat with exposure. This general behavior can be attributed to the rather significant change in shape of the I-V curves with integrated dose, as seen in the upper portion of Fig. 25. Upon careful inspection of all these data, one can easily see that the changing shape of the I-V curve clearly explains the observed exposure dependence of I_{sc}, V_{oc}, and the cell efficiency, η.

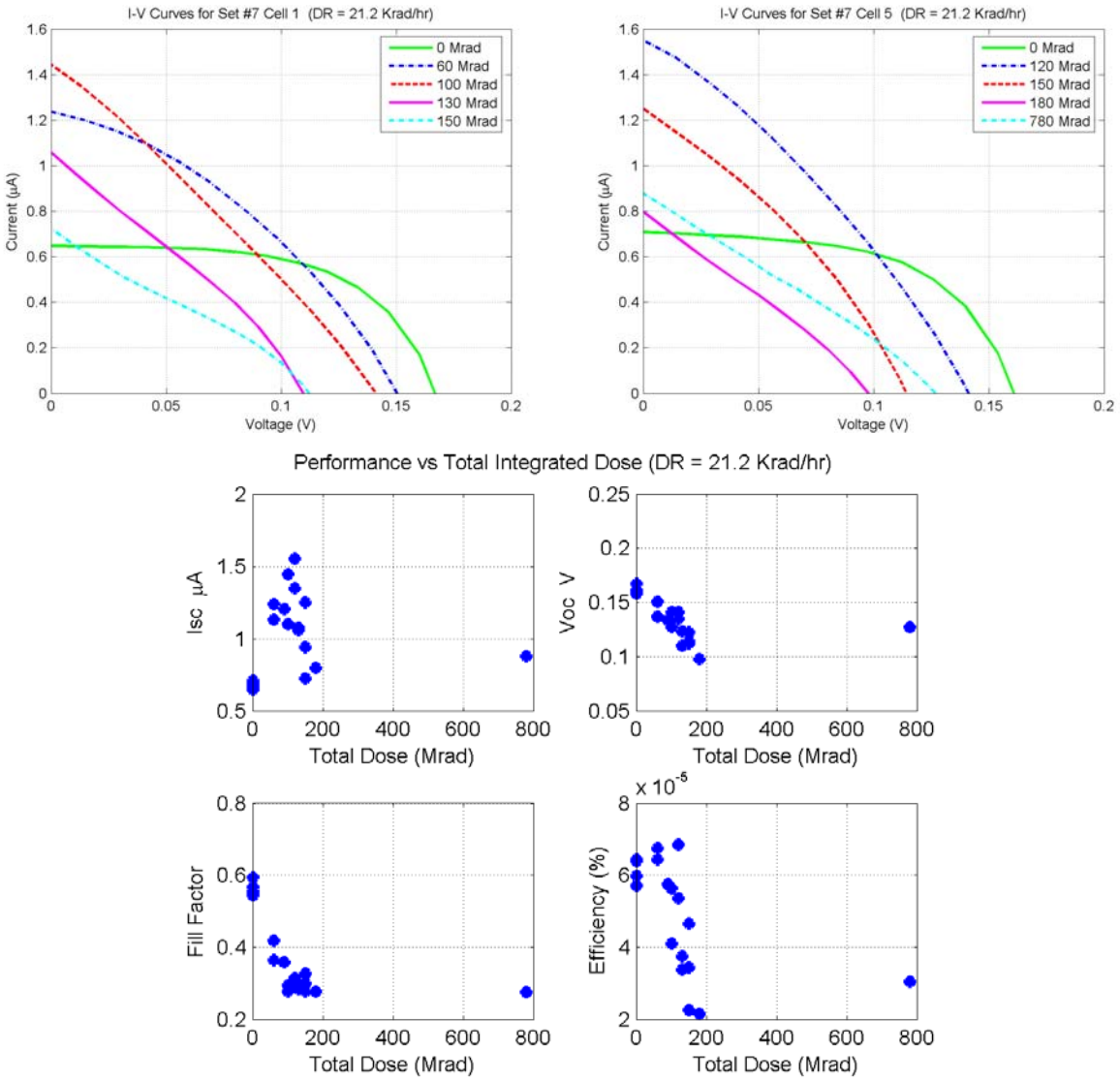

Fig. 25 Additional exposure-dependent performance data for Cell Set #7 at 21 Krad/hr.

The change in shape in the I-V curve is probably best reflected by the fill factor (FF) versus dose curve for all the cells. Recall that the fill factor, FF, is defined as the ratio of P_{max} to $I_{sc} \times V_{oc}$, or

$$FF = \frac{P_{max}}{I_{sc} \times V_{oc}} = \frac{I_{max} \times V_{max}}{I_{sc} \times V_{oc}}$$

where I_{max} and V_{max} are the current and voltage at the maximum power point. For the unirradiated Set #7 cells at a dose rate of 21 Krad/hr, the fill factor has a value in the 0.55 to 0.60 range, and this is representative of a profile with a well-defined knee in the I-V curve with moderate curvature (the FF approaches unity as the knee becomes very sharp -- approaching a 90 degree right angle). However, at exposures above about 120-130 Mrad, the fill factor is only in the 0.25 to 0.30 range, which is indicative of a near linear profile. In fact, if the I-V curve is perfectly linear, then $V_{max} = V_{oc}/2$ and $I_{max} = I_{sc}/2$, and the fill factor, FF, becomes exactly 0.25 (note that the fill factor can go below 0.25 if the I-V curve has a slight concave profile). Thus, it

appears that the shape of the I-V curve approaches a roughly linear profile after some exposure level (as indicated by visual inspection of the I-V curves and the value of the fill factor), and after this point there may be less degradation in performance with increasing exposure.

Another view of the fill factor and its relationship to performance (peak power) versus exposure is given in Fig. 26, where the left-side subplots include the 780 Mrad exposure point and the right-side subplots do not (to give a better view of the low exposure region). These plots include data from all three dose rates used as part of the current testing program. For each dose rate, the measured power clearly decreases with exposure, but there appears to be some leveling-off in the 0.02-0.07 μW power range, and this behavior is roughly similar to the FF versus TID curve which saturates in the FF = 0.2-0.3 range (which implies an I-V curve that should appear roughly linear in shape). Clearly, the gap in experimental data in the 200-750 Mrad exposure range makes it difficult to draw any definitive conclusions here. However, the shape of the I-V curve and the value of the fill factor do tend to stabilize after a rapid change at low exposures, and this could represent a plausible explanation for the observed power levels at the 780 Mrad exposure point -- but additional data are needed before this hypothesis can be confirmed.

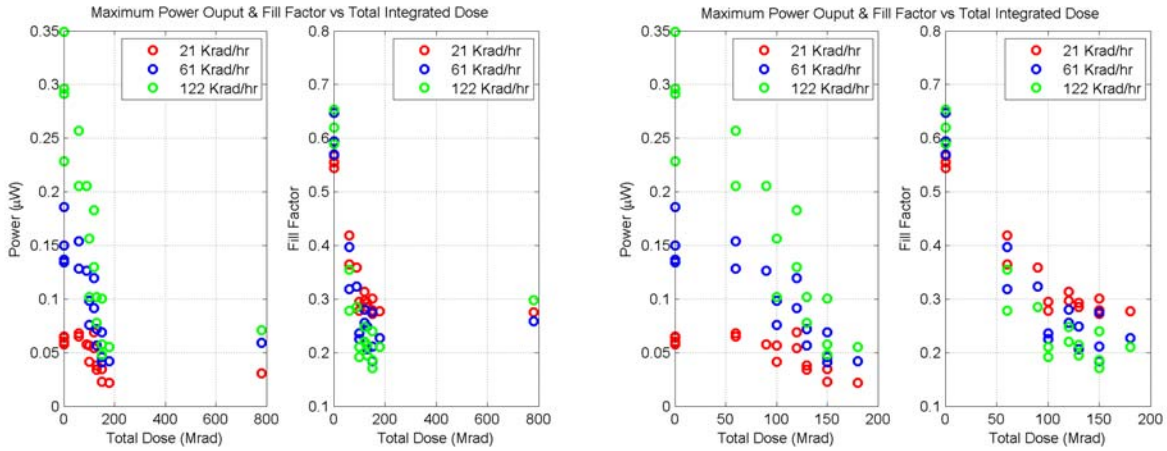

Fig. 26 Peak power and fill factor versus exposure for Cell Set #7.

The root cause of the behavior observed in the preliminary irradiation tests is not fully understood, since material damage versus exposure is generally very complex. One area of focus, however, is on the polymer adhesive used to bond and insulate the two electrodes around the cell periphery. Since physical degradation and electrolyte leakage along the seams of the cells were observed with increasing exposure, plus the fact that polymer-based materials are known to degrade under irradiation, this seems like a good place to focus attention to improve upon the overall radiation hardness of the basic gamma cell design. To address this concern, the next proposed cell design iteration would remove all polymer-based material from the cell by replacing the polymer adhesive with a more radiation-tolerant epoxy. This design change was already incorporated into the proposed Cell Set #8 specifications (as part of a future work plan). It is clear that there will be, without doubt, some degradation of basic cell operation due to material damage at high exposures even after removal of the polymer adhesive -- however, the proposed Cell Set #8 specifications should represent a step in the right direction. Once the polymer adhesive factor has been eliminated, further tests similar to those described above should help identify how the base gammavoltaic cell behaves versus exposure.

Final Note: Cell 1 in Set #5a was also irradiated to about 120 Mrad in a single step. After testing, the cell was irradiated again for another 30 Mrad, to give a total exposure of about 150 Mrad. The cell was shorted and no longer useful after the second exposure step. Thus, the behavior of this cell versus irradiation is quite similar to that observed for Cell #4 from Cell Set #7. This cell had a Teflon insulator between the electrodes, instead of the glass rods used in the Set #7 design. Both designs, however, used the polymer-based adhesive material, and it is possible that the degradation of this insulator material allowed the two Ti-metal plates to touch, leading to the observed defective behavior.

VI.1.7 Miscellaneous Comparisons

The Set #5 cells were really comprised of three subsets, where the goal was to determine the impact of the dye complex adsorbed onto the TiO_2 substrate and the use of a Pt catalyst on the inner surface of the counter electrode for the newly constructed Ti-Ti gamma cells. The problem, however, is that the large variability in performance observed with all the Set #5 cells essentially masks the effects that were being investigated. Thus, the tests were inconclusive -- that is, the effect of the design feature on performance was small enough to be hidden in the noise associated with the base data.

As an illustration, Fig. 27 compares two separate evaluations of Cell 1 from Set #5c with the performance of Cells 1, 3, and 6 from Set #5a. In this case, it is apparent that the performance of the cells with the platinum coating on the counter electrode lies within the range of performance for the three cells tested from the Set #5a batch (with no Pt catalyst). Thus, one might be able to conclude that the use of the Pt catalyst does not cause a large effect but, because of the wide range in behavior of the 5a batch of cells, this statement cannot be quantified to any degree.

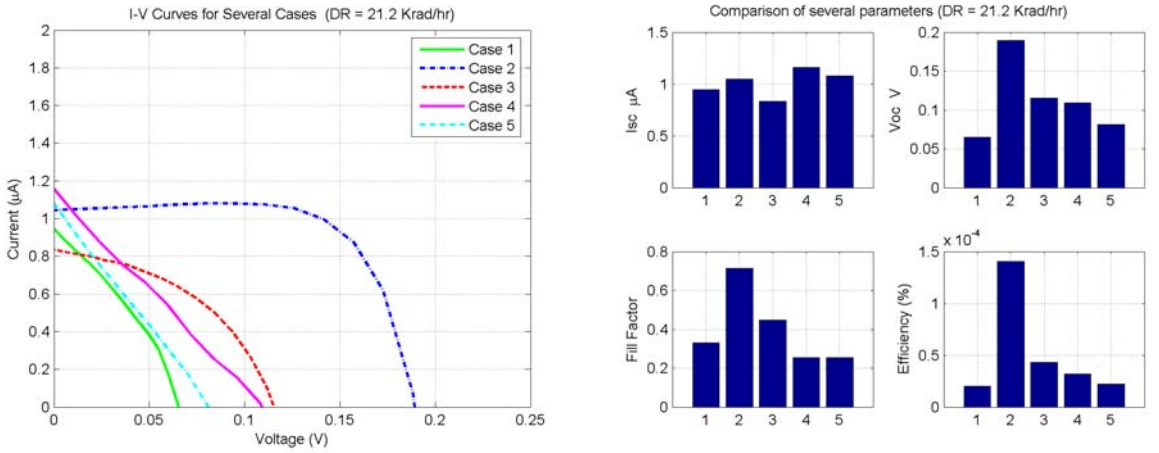


```
Legend for data sets in plots:
   Case 1.  Set 5a Test 2:  Single cell (Cell 1) on 02.16.05
   Case 2.  Set 5a Test 5:  Single cell (Cell 3) on 03.08.05
   Case 3.  Set 5a Test 6:  Single cell (Cell 6) on 03.08.05
   Case 4.  Set 5c Test 1:  Single cell (Cell 1) on 03.09.05
   Case 5.  Set 5c Test 2:  Single cell (Cell 1) on 03.11.05
```

Fig. 27 Comparison of cell behavior with and without the use of a Pt catalyst.

Thus, several of the design features studied as part of this study should be re-evaluated as part of future work now that the cell preparation process has been refined to give more consistent cell behavior for a particular batch of cells. Individual effects may be relatively small but, when combined into an optimized cell design, the composite gain could be significant. Unfortunately, in the early stages of the development of the gammavoltaic energy conversion process, the cell design and cell fabrication procedures were simply not refined sufficiently to be able to quantify the importance of some features. However, as the cell manufacturing process matures, it might be worthwhile to revisit some of the possible cell design features that gave inconclusive results in this initial study.

VI.2 Power Conversion Unit Design and Example Scale-Up Calculation

Although the power conversion capability of the new gammavoltaic cell has been clearly demonstrated, the low power output from a single cell dictates that many such cells, connected in various stacked series and parallel configurations, will be needed for a practical power conversion device. In practice, it is envisioned that a single power conversion unit will be composed of several modules connected in a parallel arrangement. Each module will contain a layered stack of cells connected in series, where the cathode of one cell serves as the anode for the next cell in the series (i.e. two cells share a common electrode). A sketch of the module construction for a particular 4-cell module is shown in Fig. 28 where, in practice, many such cells can be stacked in series to meet a given total voltage requirement (recall that the voltage output is additive for cells placed in series). An integrated power conversion unit is then completed by stacking a number of the series modules in parallel as shown in Fig. 29, where the particular arrangement sketched here includes three of the series modules. A radiation-tolerant insulator would separate each module, and the completely integrated unit would be sealed and packaged for use, as needed, for the particular application of interest.

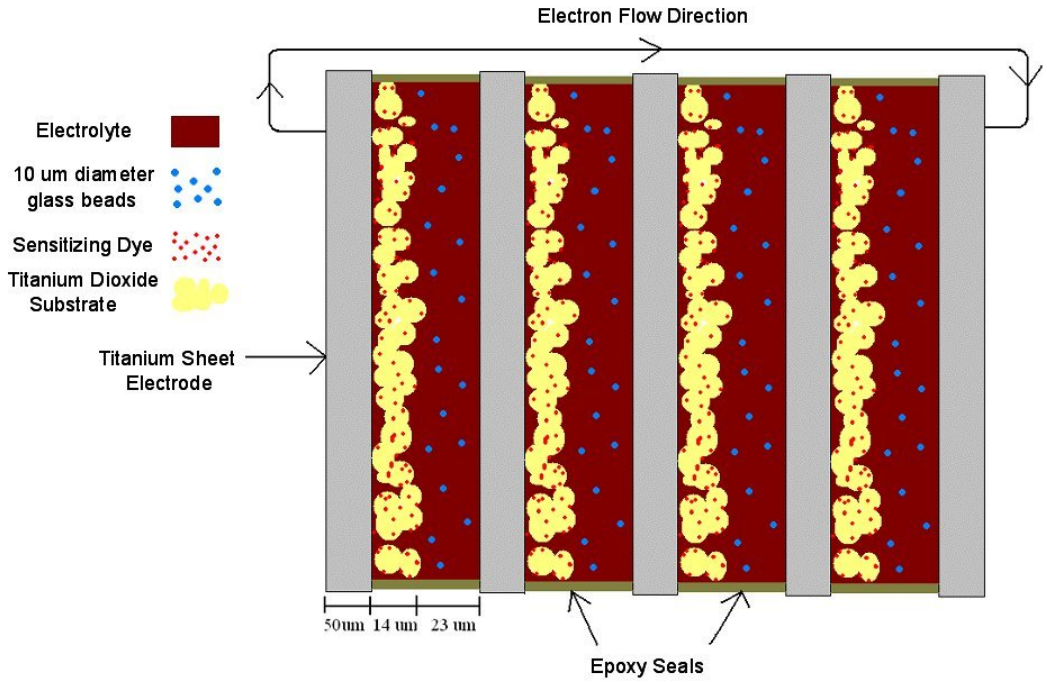

Fig. 28 Sketch of gammavoltaic module containing a series arrangement of cells.

As an example, consider a power conversion unit for the SNF monitoring application discussed previously. In the cask design modeled here, the gap between the fuel canister and the shell of the vertical concrete shield is only about 3.75 inches, and this region is used for convective cooling of the canister and cask liner. One option for placement of the gammavoltaic power conversion unit would be to use a portion of this gap region, being careful not to significantly alter the air flow and cooling capability of this region. Thus, the power conversion unit, in practice, will need to be relatively thin and, for the current example scale-up calculation, a maximum thickness of 1 inch has been selected. With this specification and the fact that a single cell is about 87 μm thick, a maximum of about 250-260 cells can be stacked within the 1" limit, including a space allowance for end electrodes, insulation between modules, and packaging. In addition, a reasonable voltage requirement for a low-power SNF monitoring system of about 4 V has been assumed.

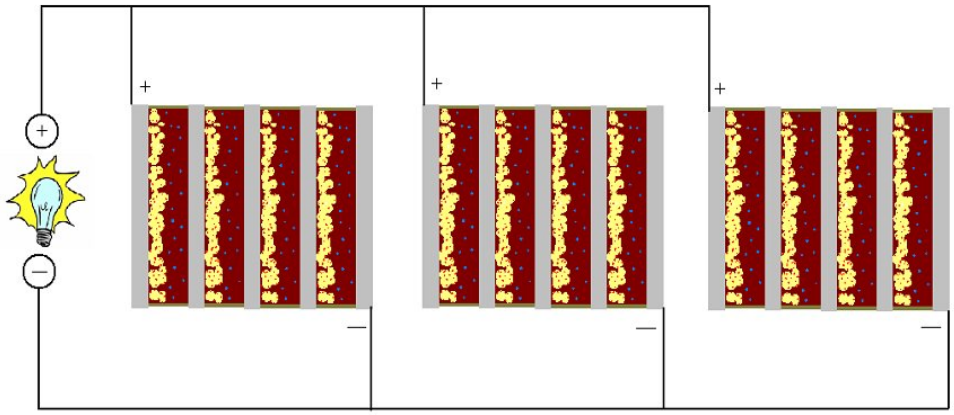

Fig. 29 Sketch of an integrated power conversion unit containing several gammavoltaic modules in a parallel arrangement.

Now, with this target voltage level and thickness limit, a hypothetical gammavoltaic power unit can be designed and an estimate can be made for the output power density under the dose rate conditions treated in the current testing program. In particular, recall that Cell 1 in Set #6 gave the best single-cell performance of all the cells tested so far. Since future cell optimization studies should lead to much better performance, it is fair to use the power conversion capability of the best cell to date to predict the overall capability of a complete module containing many cells of this caliber connected in various series and parallel arrangements. Thus, for use in this scale-up example, the measured performance data for Set #6 Cell 1 will be used. For reference, these data are summarized in Fig. 30, which shows the expected I-V relationships and near-linear increase in power production with dose rate, as for all the gamma cells tested. In addition, at the low dose rate point of about 21.2 Krad/hr (22.3 W/m^2), Fig. 30 shows that the current and voltage at the maximum power point are 1.20 μA and 0.136 V, respectively.

Using these data and the scalability feature demonstrated above in Section VI.1.3, the number of series cells required to produce a 4 V power source is

$$N_s = \frac{4\ \text{V}}{0.136\ \text{V/cell}} \approx 30\ \text{cells}$$

and, with a thickness limit of about 1 inch, this implies that the maximum number of series modules that can be placed in parallel is $N_p = 8$, to give an integrated single power conversion unit of $N_s \times N_p = 240$ layered cells.

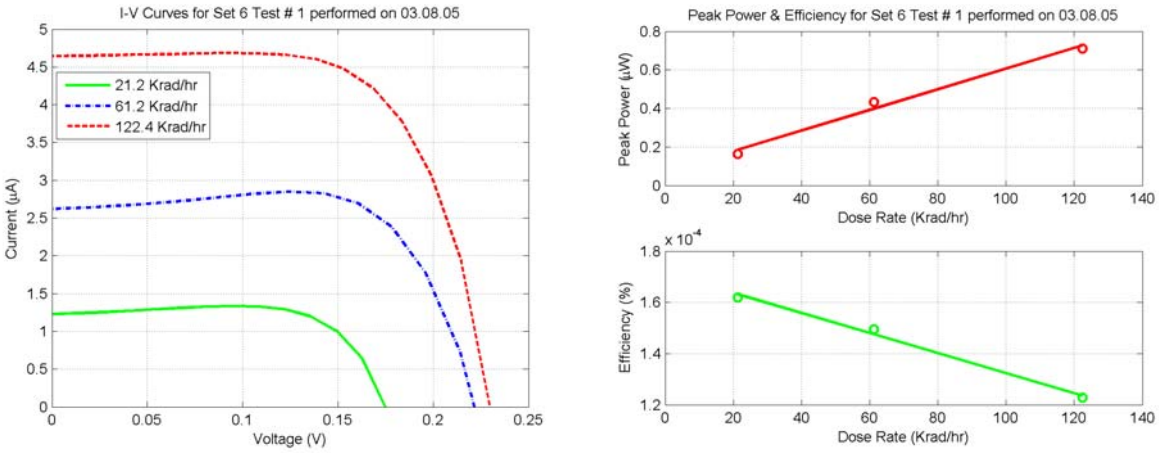

Summary Results from Test # 1 for Cell Set 6

Set Description: Ti-Ti cells (15 um TiO2 & 45 cm^2), 1:1 wt ratio of Gadox/electrolyte
Test Description: Single cell (Cell 1) on 03.08.05
Test Date: 03.08.05
Test Status: GOOD Data

Basic Test Parameters

Number of cells used:	1
Array volume (cm^3):	0.616
Beam area (cm^2):	45.0
Effective thickness (cm) of array:	0.0137
Average integrated dose (Mrad):	0.0

Array Performance vs. Dose Rate

Parameter of Interest	21.2 Krad/hr	61.2 Krad/hr	122.4 Krad/hr
Max electrical power (uW):	0.1630	0.4336	0.7117
Short circuit current (uA):	1.2320	2.6230	4.6472
Open circuit voltage (V):	0.1750	0.2217	0.2298
Fill factor (unitless):	0.7558	0.7455	0.6664
Current at Pmax (uA):	1.2010	2.6980	4.2190
Voltage at Pmax (V):	0.1357	0.1607	0.1687
Module Efficiency (%):	0.000162	0.000150	0.000123

Fig. 30 Detailed experimental results for Cell 1 in Set #6 -- the best single cell so far.

With the present generation of cells (using data from Set #6 Cell 1), the output current density of the gammavoltaic unit would be about 1.20 μA per 45 cm^2 = 0.267 mA/m^2 per module times the number of modules connected in parallel. With $N_p = 8$, this gives about 2.14 mA/m^2. Thus, the output power density for this particular design would be 4 V × 2.1 mA/m^2 = 8.4 mW/m^2.

Finally, with an input power density from the Co-60 gammas of 22.3 W/m^2, an areal power density of 8.4 mW/m^2 gives an overall unit conversion efficiency of $\eta = 0.0084/22.3 = 0.038\,\%$. This preliminary conversion efficiency, of course, is quite low -- too low, in fact, to produce useful power. However, this is based on data from a first generation, un-optimized cell design, and it is expected that, with some further development, this can be improved significantly (see the discussion of future work in Section VII).

To complete this discussion of scale-up, it is appropriate to establish a minimum target efficiency that must be met for practical implementation of a gammavoltaic power conversion unit for SNF monitoring applications. To establish some reasonable reference, assume that a peak power of 1 W would be needed for a low-power monitoring system. Also, from the radiation transport calculations detailed in Ref. 7, the input energy flux available for conversion to useful power within the radial gap between the fuel canister and the concrete shield in the NAC-UMS system is about 4.7 W/m^2 (under the conditions of the calculations). Although there is a very large surface area available in a typical storage cask (over 20 m^2), it is not practical to consider using more than 50% of the available area. Thus, as a reasonable assumption, a maximum upper limit has been set at 10 m^2 for the exposure area for the power conversion unit. With this assumption, the total power input would be approximately 47 W and, with a desired output power level of 1 W, the minimum efficiency must be 1/47 = 2.1 %.

Certainly there are a lot of assumptions here, including the maximum cross sectional area of the power conversion unit (10 m^2), the maximum power level needed by the SNF monitoring system (1 W), and the expected input gamma power density available within the SNF storage cask (4.7 W/m^2), but a minimum target conversion efficiency for the integrated gammavoltaic power unit of about 2% seems quite reasonable.

Although the cells developed and tested as part of the current research effort are not yet at this level of performance, only a factor of 50 or so improvement is needed to approach the desired target efficiency (2.1/0.038 = 55). This, of course, is asking a lot from future design and optimization efforts but, since this research represents the initial proof-of-concept study in this area, significant improvements in cell design that lead to large gains in performance in the future are not entirely unrealistic.

VI.3 Mathematical Modeling of a DSPC Cell

In conjunction with the pure experimental evaluation of cell performance as detailed in Section VI.1, a preliminary effort was also made to develop a relatively simple mathematical model of a DSPC cell. The goal here was to utilize the measured cell performance data collected in the form of the I-V curves to perform a curve fit, thereby determining the adjustable parameters associated with a mathematical model that approximately reproduces the measured I-V curves. If successful, the mathematical model could then be used as a diagnostic tool in future DSPC development. For example, the irradiation testing discussed in Section VI.1.6 showed that the cell's fill factor decreased by a factor of 2-3 over a relatively narrow exposure range, and then remained roughly constant at higher exposures. This observation is interesting, but it would even

be more useful if this behavior could be tied to one or more parameters within a given mathematical model, thereby giving further insight and understanding of cell performance versus exposure. Thus, the real goal of this modeling effort is to identify general trends in various cell performance parameters and to relate these trends to specific cell construction features and/or to the observed behavior versus exposure. The analytical information obtained from the mathematical model, coupled with additional analytical data from the ongoing microscopic material characterization study (see discussion in the next subsection), could then be used as a guide in future cell design optimization efforts -- to aid in the material selection process and in identifying the best cell construction techniques.

There exist a plethora of solar cell modeling techniques that are application specific; thus, selecting the most appropriate model was the first task in modeling the KTI gamma cells. In particular, there are different models for cells that experience high reverse bias voltage, that are modeled in large interconnected arrays, and that operate over large temperature ranges, as well as one- and two-diode models. To keep things relatively simple for this initial modeling effort, a straightforward one-diode model was selected that does not include provisions for a large reverse bias voltage or cell operation over large temperature ranges. The reason for not including such modeling considerations is that the data collected so far in this work are primarily in the power producing quadrant of the I-V curve (which does not include high reverse bias voltage measurements), and that all of the measurements thus far have been conducted at room temperature.

A schematic of the equivalent circuit associated with the standard one-diode model of a solar cell is shown in Fig. 31. Applying Kirchhoff's current law to this circuit gives

$$I_{PH} - I_D - I_P - I = 0$$

where I_{PH} is the photon-generated current from the gammavoltaic cell, I_D is the diode current, I_P is the current through the internal parallel resistance, and I is the terminal current that passes through the internal series resistance, R_S, and the external load. Solving this expression for I, inserting a more detailed expression for I_D, and writing I_P as the voltage drop divided by the parallel resistance, R_p, gives the following nonlinear mathematical model that relates the terminal current, I, to the terminal voltage, V:

$$I = I_{PH} - I_S\left(e^{\frac{V+R_S I}{c_1 V_T}} - 1\right) - \frac{V + R_S I}{R_P}$$

where I_S is the diode reverse saturation current, V_T is the temperature voltage (this is a known parameter), and c_1 is the diode ideality factor. The parameters that are measured when collecting I-V curve data are the terminal voltage and current, whereas the other five parameters (I_{PH}, I_S, R_S, R_P, and c_1) are estimated by interpretation of the characteristic I-V curve, and then solved for using a formal nonlinear curve fitting technique.

Note that the diode ideality factor, c_1, presented here does not have the same physical meaning as for solid-state solar cells.[15] Instead, DSPC operation is somewhat more complex, and the DSPC cell behavior usually cannot be easily represented by the single diode model used in solar cell modeling. However, if the diode ideality factor is simply treated as a curve fitting parameter (with no direct physical meaning), then this model may still allow for accurate I-V curve modeling as well as general parameter-based comparison between the different cells.

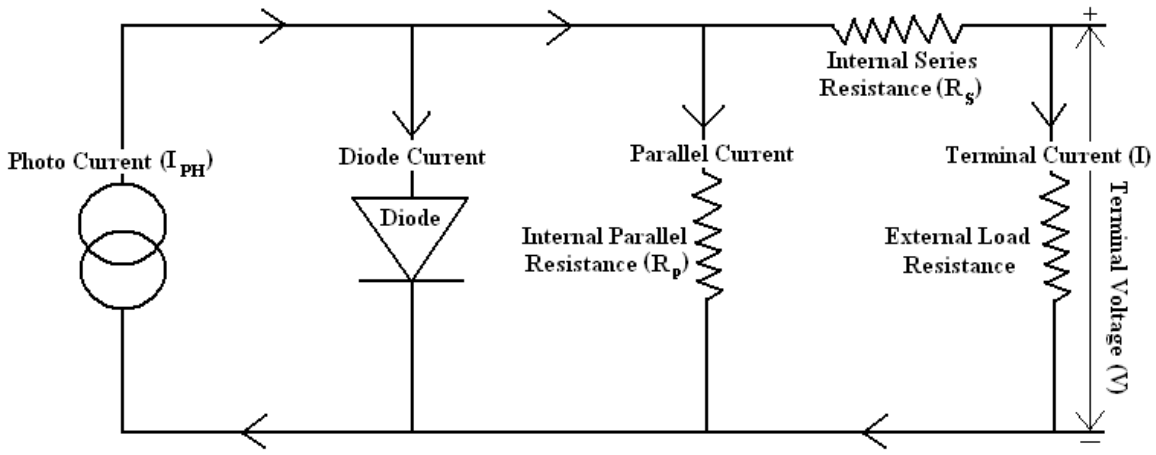

Fig. 31 Equivalent circuit diagram for DSPC modeling.

With the above model as the desired mathematical representation, the challenge now shifts to finding the best set of five parameters for a particular set of measured I-V data. A Matlab code was developed for this purpose which takes advantage of Matlab's built-in ***fzero*** and ***nlinfit*** capability to evaluate nonlinear equations and to perform non-linear least squares curve fitting, respectively. The code has four primary sections, as follows:

1. The measured I-V curve data are read into Matlab using an application-specific GUI.
2. The I-V curve data are preprocessed to find estimates of the cell parameters in question.
3. A nonlinear curve fit is performed using the parameter estimates from Step 2 as initial guesses for the coefficients of the curve fit.
4. Finally, the output coefficients from the curve fitting are post processed into graphical and tabular formats.

In order to generate a starting point for the nonlinear curve fit routine, initial values or estimates of the curve fitting coefficients must be available. Analyzing various sections of a given I-V curve allows for the estimation of the parallel and series resistances, diode ideality factor, and photon generated current. In particular, Ref. 16 shows that the internal parallel and series resistances are related to the inverse of the slope where the I-V curve crosses the current axis (short circuit current, I_{sc}) and the voltage axis (open circuit voltage, V_{oc}), as illustrated in Fig. 32. Therefore, taking the inverse of the slope of the curve using the starting and final two sets of V,I data pairs gives the desired estimates for the series and parallel resistances, assuming a voltage sweep in the backward direction (i.e. from positive to zero voltage).

When trying to estimate the diode ideality factor, which primarily affects the curvature of the I-V profile near the maximum power point (commonly referred to as the "knee" of the I-V curve), several assumptions must be made regarding the significance of terms in the characteristic equation (see Ref. 17). For example, the one-diode model can be reduced to

$$I \approx I_{PH} - I_S \, e^{\frac{V+R_S I}{c_1 V_T}}$$

by assuming that V > 0.1 volts at 300 K and $c_1 < 2$, as well as neglecting the $(V+R_SI)/R_P$ term by assuming $R_P >> R_S$ (see Ref. 16). Taking the natural logarithm of both sides of this reduced equation gives

$$\ln\left(I_{PH} - I\right) \approx \ln(I_S) + \frac{1}{c_1 V_T}(V + R_S I) \approx \ln(I_S) + \frac{1}{c_1 V_T} V$$

Thus, a plot of $\ln(I_{PH} - I)$ versus V yields a slope of $1/(c_1 V_T)$ -- from which the diode ideality factor, c_1, can be estimated.

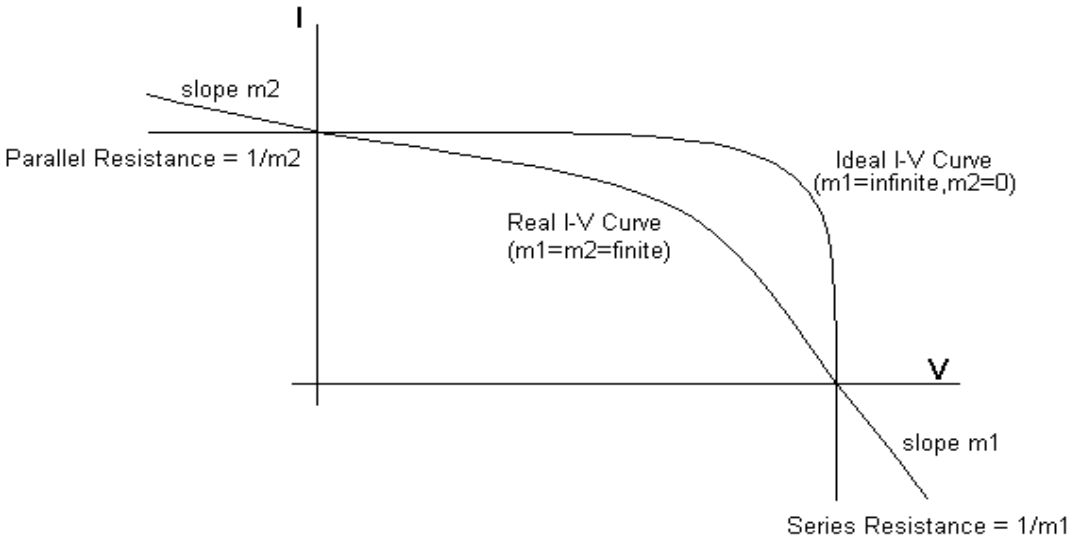

Fig. 32 Illustration of graphical determination of parallel and series resistances.

Extracting the value for the photon current, I_{PH}, from I-V data typically involves subtracting the short circuit dark current value from the short circuit current under illumination or, in this case, under irradiation. This gives an empirical value for the current generated by a given cell by taking the difference between how much current the cell produces under irradiation and how much current is produced by the cell in the dark at zero volts. However, lack of dark I-V curve data, particularly at high TID levels, dictated using the short circuit current alone as an estimate of the photon current produced by a given cell.

Finally, the only remaining variable in the 5-parmeter model is the reverse saturation current, I_S. Since there was no easy way to estimate this quantity, the initial guess, in all cases, was set to 1 nA, thus completing the set of initial guesses needed by Matlab's ***nlinfit*** routine.

The curve fitting procedure described above was initially tested using standard solar cell I-V data generated using known coefficients for the cell parameters based on information taken from Ref. 17. The reason for this initial verification effort was to insure that the curve fit was producing accurate cell parameter values and not just a good curve fit based on the lowest possible residual. For example, it became apparent after performing several curve fits that there is a strong interdependence between the diode ideality factor and the series resistance value. Therefore the curve fit could actually give an excellent match to the data with a correlation coefficient near unity, but produce inaccurate diode ideality factor and series resistance coefficients. Based on

this result (and several other observations from the initial model testing), an option was incorporated that allows the user to select the number of free parameters for the curve fit. For example, since the procedure illustrated in Fig. 32 gave good estimates of the series resistance, one might fix this parameter at the estimated value, and not include it as a free parameter in the nonlinear curve fit (i.e. with R_S excluded, the mathematical model reduces to a 4-parameter model). In some cases, especially for I-V data at high exposures, this approach gave a more realistic representation of cell behavior.

Although there is still much to be learned from this cell modeling effort (with several variants of the algorithm that still need to be tested), the preliminary work completed thus far suggests that this line of work may indeed lead to a better understanding of cell performance. One illustration that highlights this conclusion is the dependence of the internal parallel resistance with exposure, as shown in the upper part Fig. 33. In particular, the 4-parameter model (excluding R_S from the curve fit) was used to characterize Cell 3 from Set #7 over a range of TID levels from 0-150 Mrad. The model coefficients that resulted from the 4-parameter curve fit at each TID level were plotted versus exposure, with the behavior of R_P shown in Fig. 33. A similar relationship versus exposure, however, was previously seen when plotting the fill factor versus TID, and this has been included in the lower subplot for direct comparison. Clearly, there is a direct relationship here that suggests that the fill factor (and the shape of the I-V curve) is strongly correlated with the cell's parallel resistance. Also, during actual irradiation testing, it was observed that the Bynel seals which serve as the insulation layer between the anode and cathode showed significant degradation with exposure. With insulator degradation, one might expect a drop in internal parallel resistance and, according to the data given here, a corresponding drop in fill factor. Although more work is needed in this cell modeling effort, obtaining further insight and understanding into these types of cause-effect interactions is exactly why this work was initiated.

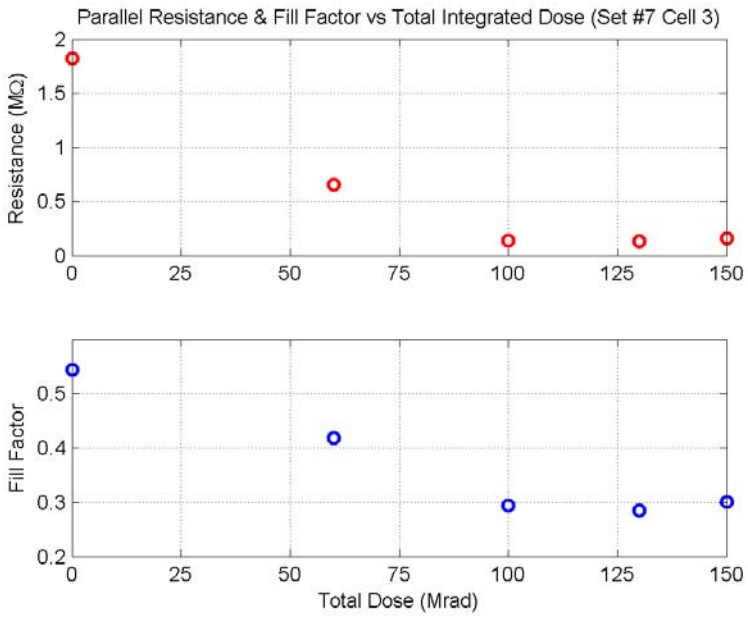

Fig. 33 Parallel resistance and fill factor dependence on cell exposure.

VI.4 Materials Characterization Effort

Another analytical tool employed as part of this work was the use of atomic force microscopy (AFM) and transmission electron microscopy (TEM) to characterize the microstructure of the DSPC cells both before and after irradiation. AFM utilizes physical contact with a nanometer-scale probe in order to detect the microscopic surface features of a material. The application of AFM analysis in this project was to investigate the surface structure of the TiO_2 as well as the degree of bonding between the TiO_2 substrate and the Ti metal. Analyzing the surface structure of the TiO_2 allows for a quantitative analysis of surface roughness, which affects the usable surface area of the substrate. Investigation into the degree of substrate to electrode bonding is important in terms of charge transfer between the two physical boundaries, especially when considering that the thin cells are flexible and that excessive cell flexing could lead to interfacial debonding.

TEM operates by using a cathode to produce a stream of electrons, which are then focused onto an extremely thin sample (less than 200 nm thick) using a magnetic field. TEM forms an image by detecting electrons that are transmitted through the material sample. The incident electron beam interacts with a very small volume of material, called the interaction volume. Secondary electrons, backscattered electrons, and X-rays are produced from the electron beam excitation, but only the secondary electrons are detected due to their relatively low energy. At raised surfaces on the material, more secondary electrons can escape the interaction volume, which results in a bright spot that represents an edge or feature in the sample. A scintillation material, which interacts with the secondary electrons, is used in conjunction with a photo multiplier tube to control light output to a CRT -- which then displays the magnified image. Magnification of up to 500,000 times is achievable with TEM technology.

Sample surface preparation is the most important factor when performing TEM analyses. Coating the sample with an electrically conductive material such as gold or graphite is necessary in the case of semiconductor or insulator materials to allow for better electron interaction. In order to prepare a DSPC sample thin enough for analysis, a microtome (which utilizes a very accurate diamond knife) was used to pare the sample down to less than 200 nm thickness. Other methods of sample thinning, including grinding, polishing, ion beam milling, and sputtering, were not performed in favor of the faster and higher quality microtome sample preparation method.

Transmission electron microscopy (TEM) was utilized because of its overall good resolution and its ability to allow for compositional analysis in energy dispersive x-ray spectroscopy (EDXS) mode. EDXS mode operates on the principle that each element emits characteristic x-ray photons when bombarded by electrons of high enough energy to cause electrons to transition to different energy orbitals. The resultant x-rays are then detected by a lithium-doped silicon crystal, which emits a pulse magnitude proportional to the energy of the incoming x-ray. EDXS analysis was performed to verify the purity of the DSPC composition, since impurities can lower the overall cell efficiency.

The focus of the materials characterization work for this project was to compare the AFM and TEM analysis of a DSPC cell before and after gamma irradiation in an effort to detect any radiation-induced changes to the cell microstructure that may have occurred. In particular, Cell 1 from Set #4 and Cell 5 from Set #7 were destructively tested using both AFM and TEM techniques. The Set #4 cell was unirradiated but, as discussed previously, Cell 5 in Set #7 was

irradiated to an exposure of about 780 Mrad. The makeup of the two cells and the overall gamma cell preparation method were slightly different (see the discussion in Section V.2), but the TiO_2 substrate, dye adsorption, and method for bonding to the Ti plate were identical for the two cells. Thus, the only real difference from the materials characterization perspective is that the two samples have significantly different total integrated doses -- 0 Mrad and 780 Mrad. Thus, the real goal of this study is to compare the AFM and TEM analyses before and after irradiation to identify what type of radiation induced changes might occur in the base cell microstructure (for use as a diagnostic tool in troubleshooting material and performance degradation).

Unfortunately, at the time of this writing, the AFM and TEM analytical results for the irradiated sample are not yet complete -- thus, no comparative analysis can be performed at this time. Although the AFM/TEM analyses of the irradiated sample are nearly finished, a detailed comparative study still has yet to be performed -- and this will be treated as part of a future project related to this work.

VII. Summary and Recommendations for Future Work

VII.1 Summary

This work has been successful in establishing feasibility of a new direct energy conversion concept that utilizes gamma photons to drive a gammavoltaic cell -- a device that is based, in principle, on Konarka Technologies' novel dye sensitized solar cell design, but that has been modified to also be sensitive to high energy gamma photons. The initial focus for this new technology was geared towards the development of an inherent power source for use in spent nuclear fuel (SNF) cask monitoring applications.

Several different cell designs were developed, fabricated, and tested as part of this program. The key results of the initial characterization effort are listed below:

1. Measurable power can be produced from the gammavoltaic cell and the output power is linear with gamma dose rate.
2. The power level from a single thin-film cell is quite small (< 0.1 mW/m^2) for an input dose rate of about 20 Krad/hr because of the low interaction probability of the incident gamma photons.
3. Since the gamma photons penetrate the cell volume, the individual thin-film cells can be stacked with series and parallel electrical connections to increase the active cell volume per unit area exposed to the gamma photon source.
4. To first order, the output power from the stacked cell configurations scales linearly with cell volume -- that is, a tenfold increase in volume should increase the areal power density by about a factor of ten.
5. The output voltage is additive for cells connected in series and the current is additive for cells connected in parallel. This feature allows flexibility in designing an integral gammavoltaic power conversion unit for different applications.

6. An internal scintillator material can improve cell performance by better matching the photon spectrum to the peak sensitivity of the dye-sensitized TiO_2 substrate within the cell. The amount of improvement has not been quantified as yet (more experimental data are needed).
7. Preliminary testing to address the service lifetime of the gamma cells has also been initiated. The cells tested thus far show decreased performance versus integrated dose, and complete cell failure was observed for two individual cells with exposures in the range of 150 Mrad. However, since physical degradation and leakage from the polymer-based adhesive seals along the periphery of the cells were observed, it is believed that this early failure of the current generation of gammavoltaic cells is due primarily to the adhesive used to insulate the two titanium electrodes and seal the overall cell. This polymer adhesive will be replaced with a more radiation-resistant epoxy in future cell tests. Also of note is the fact that one cell was irradiated to a total exposure of about 780 Mrad and, although performance was decreased, this cell was still capable of producing some power after this exposure level. This observation suggests that the performance degradation may saturate after some amount of gamma irradiation -- but further testing is needed to confirm this hypothesis.
8. A conceptual design for an integrated power conversion unit was also considered. The design includes several modules stacked in parallel to increase the current density, with each module containing several layered cells in series to meet the voltage requirement for the particular application. For a specific scale-up example using reasonable assumptions for a low power SNF monitoring system, the overall power conversion efficiency was estimated to be about 0.04 %. This example was scaled using measured results from the best single cell tested thus far.
9. Some preliminary work to develop and use different diagnostic tools to help understand the observed cell behavior has also been initiated. This work included the development of a computational tool to perform nonlinear curve fits to the measured I-V data, and the use of AFM and TEM techniques to perform a comparative study of the changes that occur during gamma irradiation of the DSPC cells. Both of these tools hold promise for improved analytical capability and increased understanding of future cell designs.

VII.2 Future Work

This initial research has formulated and demonstrated the basic gammavoltaic power conversion concept, with focused attention on its potential utilization as an in-situ power source for monitoring the location and condition of spent nuclear fuel for increased security during transport and storage. Although a number of important issues associated with the new technology have been addressed, there are still many unresolved questions and uncertainties concerning the practical use of this concept for the intended SNF monitoring applications, where the remaining issues can be grouped into two main categories: overall performance and the service lifetime within a typical SNF cask environment.

VII.2.1 Improved Performance

In a specific example, the overall incident power conversion efficiency was estimated to be about 0.04 % for an integrated gammavoltaic unit using cells generated as part of this initial research effort. However, it was also estimated that an efficiency of about 2 % would be needed for practical implementation of the concept within a SNF monitoring application. This difference in available versus needed performance suggests that a 50-fold increase in efficiency is required for

practical use of this concept for the intended application. This certainly represents a challenge for future studies, but there are also a number of areas where significant improvements in cell design and manufacture could possibly lead to improved performance that approaches this target level, including the use of a typical SNF gamma spectrum versus a Co-60 spectrum, cell optimization focused on finding the best type and loading for the scintillator material, and the investigation of cell chemistry and module construction improvements to enhance performance.

One important issue for efficient utilization of both solar and gamma cells is to match the spectral sensitivity of the cell to the spectrum of the incident energy flux. In the current work, essentially unperturbed Co-60 gamma rays were used as the incident photon source for testing the power production capability of the various cells. However, in a SNF cask, the expected gamma energies take on a broader distribution, with a lower energy peak than the 1.2 MeV gammas from Co-60, as highlighted in Fig. 34. Although the expected improvement cannot be easily quantified, an increase in efficiency with the actual SNF spectrum relative to the Co-60 spectrum is certainly expected. Thus, one area of focus for future studies is the development of a spent nuclear fuel environment simulator (SNFES) so that a more realistic radiation test environment can be used during characterization of the dye-sensitized photon converter (DSPC) modules. This effort, although not directly focused on cell development, should show an real improvement in the base-level cell efficiency -- since testing within the softer gamma spectrum typical of SNF applications will lead to a greater primary gamma interaction rate.

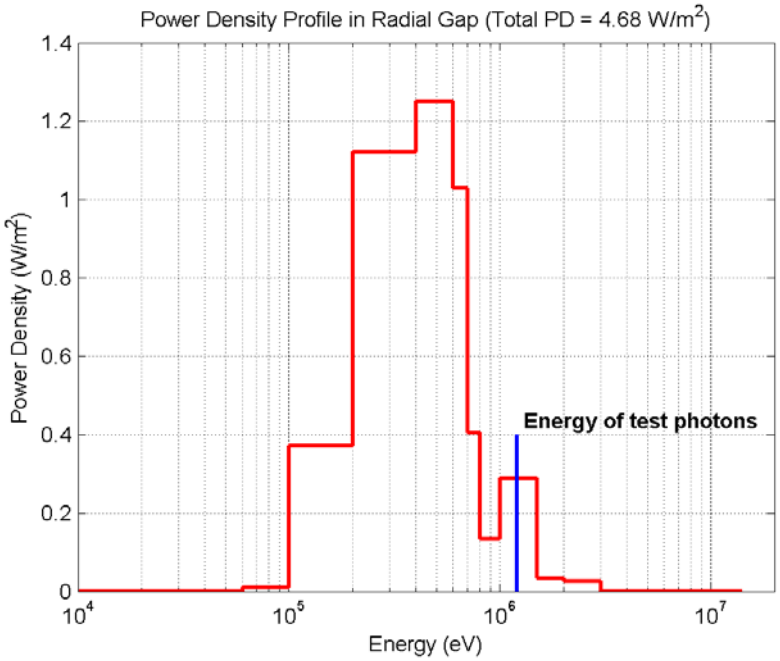

Fig. 34 Typical gamma energy deposition spectrum just outside a SNF storage canister.

A brief preliminary review of potential scintillator materials has been completed as part of the current study, and some initial testing with a single concentration of gadolinium oxysulfide (Gadox) has been performed. These studies have suggested that adding a scintillator material to convert some of the incident high energy photons into photons in the visible spectrum should significantly improve the overall performance of the gammavoltaic cells. Unfortunately, however, as of this writing, a statistically significant number of measurements are not available

to explicitly quantify this improvement. Thus, a second area for additional work is to significantly expand the experimental database of different scintillator materials at different concentration levels. Potential problems with the electrolyte-scintillator interactions should also be examined to ensure that long-term irradiation exposure does not produce significant degrading photochemical interactions.

The current cell chemistry for the gamma cells is based on Konarka's reference design that was optimized for solar energy conversion applications. Thus, a third major effort to improve overall efficiency is to modify and adapt, as needed, Konarka's proven electrolyte and dye combinations specifically for the gammavoltaic cell design. KTI has developed a wide variety of electrolytes ranging from solvent-based electrolytes to near solid electrolytes. Similarly, the dye development has covered a wide range of absorptances -- primarily in the solar spectrum. Thus, there is the potential for significant efficiency improvement by optimizing the cell chemistry for spectral and chemical compatibility with the scintillator material chosen, and for direct use of the incident high-energy gamma photon flux associated with typical SNF applications.

VII.2.2 Service Lifetime Considerations

Assuming that the power conversion efficiency can be improved to levels sufficient for practical implementation, the longevity issues associated with long-term operation of the gammavoltaic cells in a relatively harsh environment still need further study. In particular, since operating temperatures as high as 100 C or more are possible, plus the fact that total integrated exposures of 1000 Mrad or more may be required, it is clear that testing and qualification under these conditions needs to be an important component of any future studies.

For example, all the experimental testing to date has been done at room temperatures. To address this, an important part of the design of the spent nuclear fuel environment simulator (SNFES) mentioned above would be to include a heating unit, chosen from a variety of commercially available devices, that is capable of producing a thermal environment similar to that present in typical SNF applications. The final SNFES facility would then allow cell design characterization within the radiation and thermal environment expected to be present during actual use of the gammavoltaic power conversion unit.

Some preliminary evaluation and design modifications that consider the cell performance under long-term irradiation have already been addressed (i.e. removal of the Teflon spacer from the current design and elimination of the polymer-based adhesive in the next cell design iteration). However, since a 30-year service life may require very large total exposures, all the cell and module components will need to be highly radiation resistant. Thus, any future studies will also need to address this concern, with the careful selection of materials and fabrication techniques to maximize the service lifetime of the cells. Significant effort will be needed to complete a systematic integrated dose testing program, but this work is essential for the proper design, evaluation, and qualification of the gammavoltaic cells for long-term use as an inherent power source for SNF monitoring applications.

With the question of concept feasibility clearly resolved with the current effort, the burden of subsequent work in this area now needs to focus on design improvements that can lead to practical implementation scenarios. It is expected that progress in the several areas of future work identified here should help move the gammavoltaic energy conversion concept much closer towards this ultimate goal.

VIII. References

1. General information about Konarka Technologies, Inc. and its products and manufacturing processes can be found at www.konarkatech.com.
2. See discussion of dry cask storage options and site locations at www.nrc.gov/waste/spent-fuel-storage/dry-cask-storage.html.
3. G. Mintsis, et. al., "Applications of GPS technology in the land transportation system" **European Journal of Operational Research , 152,** 399-409 (2004).
4. US DOE National Transportation Program "TRANSCOM a Transportation Tracking and Communications System" at www.ntp.doe.gov/ftplink/transcom.pdf.
5. B. O'Regan and M. Graetzel, "A Low Cost High Efficiency Solar Cell Based on Dye-sensitized Colloidal TiO_2 Films,**" Nature**, **353**, 737 (1991).
6. M. Graetzel, "Molecular Photovoltaics that Mimic Photosynthesis," **Pure & Applied Chemistry**, **73**, 459 (2001).
7. J. R. White, "Preliminary Characterization of the Radiation Field Within a Typical Spent Fuel Storage Cask," Internal Documentation, Chemical and Nuclear Engineering Dept., UMass-Lowell (Aug. 2004). This document is included here as an Appendix to this Final Report.
8. "Final Safety Analysis Report for the UMS Universal Storage System," NAC International, Docket No. 72-1015 (March 2004).
9. G. F. Knoll, **Radiation Detection and Measurement**, 3rd Edition, John Wiley & Sons, Inc. (2000).
10. Yu. K. Akimov, "Scintillation Counters in High Energy Physics," Joint Institute for Nuclear Research, Academic Press (1965).
11. General information about the radiation facilities within the UMass-Lowell Radiation Laboratories can be found at www.uml.edu/Dept/Physics/Rsc/RL/index.htm.
12. Specification data for FWT-50 Alanine Pellet Dosimeters, Far West Technology, Inc. at www.fwt.com/racm/prod_racm.htm.
13. "BUGLE-96 - Coupled 47 Neutron, 20 Gamma-Ray Cross Section Library Derived from ENDF/B-VI for LWR Shielding and Pressure Vessel Dosimetry Applications," Radiation Safety Information Computational Center, DLC-185 (1996).
14. Product information and data sheets for Keithley Instruments Model 2400 Series SourceMeter Line can be obtained at www.keithley.com/products/currentvoltage.
15. B. O'Regan, F. Lenzmann, R. Muis, and J. Wienke, "A Solid-State Dye-Sensitized Solar Cell Fabricated with Pressure Treated P25-TiO_2 and CuSCN: Analysis of Pore Filling and IV Characteristics," ***Chem. Mater.***, **14**, 5023-5029 (2002). Full text can be found at http://www.ecn.nl/docs/library/report/2002/rx03005.pdf.
16. A. L. Fahrenbruch and R. H. Bube, **Fundamentals of Solar Cells**, Academic Press, 1983.
17. P. Mialhe, J.P. Charles, A. Khoury, and G. Bordure "The diode quality factor of solar cells under illumination," ***J. Appl. Phys.***, **19**, 483-492 (1986).

IX. Acknowledgement and Disclaimer

This report is based upon work supported by the U.S. Department of Energy under Award No. DE-FG07-04ID14603. Any opinions, findings, and conclusions or recommendations expressed in this report are those of the authors and do not necessarily reflect the views of the Department of Energy.

Appendix

Preliminary Characterization of the Radiation Field Within a Typical Spent Fuel Storage Cask

Preliminary Characterization of the Radiation Field Within a Typical Spent Fuel Storage Cask

Dr. John R. White

Chemical and Nuclear Engineering Department
University of Massachusetts Lowell

August 31, 2004

Introduction

The University of Massachusetts Lowell (UMass-Lowell) Radiation Laboratory is investigating a novel radiation sensing technology with applications for in-situ monitoring of Spent Nuclear Fuel (SNF) during cask transport and storage. The technology relies on the radioactive decay energy of SNF to self-generate electric power for the monitoring systems, avoiding the less secure aspects of external or battery powered monitoring systems. One promising technique would use a new dye-based photovoltaic material[1-2] that scavenges waste energy from high-energy gamma photons and produces electrical power. The electric power from the gamma photon interactions can then power a GPS-class transceiving system possessing the ability to pinpoint the location and presence of the SNF cask and its contents. To establish proof-of-concept, the project involves experimentally evaluating a number of potential material combinations for the photoconverter. These experiments will focus on evaluating the power producing potential of the test materials as a function of dose rate and total integrated dose.

In support of the experimental program, an effort to characterize the radiation environment within a typical SNF storage cask has also been initiated. The goal of this separate task is to estimate the neutron and gamma dose rates at different locations within a typical storage canister and cask arrangement. In addition, an estimate of the time-integrated total dose is needed to establish the expected service lifetime of the photoconverter materials associated with the in-situ monitoring system. This information -- the dose rate and total integrated dose versus position within the storage system -- will be used to set parameter specifications for performing the material irradiations and to guide the overall concept development of the photocatalytic energy conversion system.

This report summarizes the radiation environment characterization effort, including the development of a computational model of a typical SNF interim storage system, the generation of macroscopic cross sections and response functions for use in the calculations, the development of the neutron and gamma sources within the SNF, and the actual radiation transport calculations and results. It also draws some preliminary conclusions relative to the suitability of various regions within the storage system as appropriate locations for placement of the photoconverter materials.

Overview of the Modeling/Characterization Process

The goal of the radiation transport modeling performed here is to determine the neutron and gamma dose rates in air* throughout a particular SNF storage configuration. The computational system in place at UMass-Lowell for this type of work usually relies on the DORT code[3] and BUGLE-96 cross section library[4] when 2-D radiation transport analyses are needed. DORT solves the Boltzmann transport equation using the discrete ordinates method for the angular variable, a finite difference mesh for the spatial variable in 2-D geometries, and the standard multigroup approach for treating the energy dependence of the coupled neutron and gamma radiation field. The BUGLE-96 multigroup library contains the required cross sections, kerma factors, and a variety of response functions in a particular 47 neutron and 20 gamma group structure that is appropriate for deep penetration radiation shielding analyses, where good high energy resolution is needed to accurately account for particle transport from a source region to all affected areas within the geometry of interest.

In the usual reactor physics analysis, the particle source is associated with the neutrons and gammas given off in the fission process within the fueled region of the reactor. However, for SNF storage applications, the neutron source comes primarily from actinide spontaneous fission and α,n reactions in the fuel, and the gamma source is associated with the radioactive decay of both the fission products and actinides in the fuel, as well as from the decay of activation products within the fuel hardware (in both the fueled region and end fittings of the fuel assembly). Thus, a series of source calculations is needed to determine the distributed source that is required as input to the DORT computations. This type of source calculation is usually performed with the ORIGEN code, and the ORIGEN-S version, which is distributed as part of the SCALE 5.0 modular code system,[5] is the one currently in use at UMass-Lowell.

Thus, the modeling process can sometimes be rather involved, with the use of several codes and data libraries, and a variety of pre- and post-processing steps to properly prepare the output of one code for use by another or for extracting the actual desired result from a large amount of information that is usually generated. Over the years, a series of general-purpose Matlab scripts have been developed locally to assist in this process.[6-7] Also, each new analysis often requires some specialized manipulation that is unique to the particular problem under study.

For the current analysis, the key steps in the modeling process are listed below:

1. Review the literature and select a typical SNF storage configuration for analysis.
2. Obtain typical geometry and material information and prepare a DORT computational model.
3. Using BUGLE-96, generate a problem-specific library of macroscopic cross sections and process any kerma factors or response functions needed for the current study (air kerma factors and a set of flux-to-biological dose conversion factors).
4. For a particular fuel assembly design, generate the neutron and gamma sources that can be expected after some specified minimum cooling period. Also analyze the time dependence of the sources to help estimate the integral dose received by the photoconverter material during a specified service lifetime.

---

* The air dose rate in rad/hr was chosen for this work since the Co-60 irradiation facilities at UMass-Lowell have been characterized experimentally using the dose rate in air as reference.

5. With the geometry, material cross sections, and distributed source established, run DORT to compute the neutron and gamma radiation environment throughout the given geometry.
6. Using the DORT fluxes and desired flux-to-dose conversion factors, generate a map showing the air dose rate distribution throughout the SNF storage configuration.
7. Use the above results to identify potential locations within the storage configuration for placement of the photoconverter materials and to establish air dose rate and integrated dose requirements for planning the irradiation program within the UMass-Lowell irradiation facilities.

Documentation of these tasks for the current analysis is given in the remaining sub-sections of this report.

The DORT RZ Model

Items 1 and 2 from the above list lead to the development of a SNF storage geometry that is compatible with computations using the DORT code. Based on the amount of information available, the NAC Universal Multipurpose Cask System (NAC-UMS) was chosen as a typical storage configuration for the current study. In particular, the NAC-UMS Final Safety Analysis Report (FSAR)[8] was used extensively to identify the geometry and material details for the SNF storage environment and to select a variety of design basis parameters, such as the fuel enrichment, average burnup, minimum cooling time, etc.. In addition, some intermediate results from the current study were checked against the UMS FSAR as a validation that the computational results generated as part of the current study are well grounded -- and that they give a reasonable representation of the expected radiation environment within a typical interim SNF dry storage facility.

As shown in Fig.1, the NAC-UMS design consists of a transportable storage canister, a vertical concrete cask, and a transfer cask that is used for safely transporting and transferring the spent fuel assemblies within the storage canister from the wet storage pool to the dry concrete cask. Since the transfer process occurs over a brief period of time, only the fuel basket/canister arrangement within the vertical concrete cask is treated here. A sketch of the actual storage configuration that is modeled is shown in Fig. 2.

A relatively simple RZ axisymmetric model that represents the geometry depicted in Fig. 2 was constructed for this study. The 2-D model does not include any air penetrations in the concrete cask, and the baffle/structural region just below the canister was simplified considerably. In addition, the fuel basket region, containing 24 PWR fuel assemblies, fuel tubes, neutron absorber material, and a series of stainless steel support disks and aluminum alloy heat transfer disks, is treated as a single 144-inch tall material region

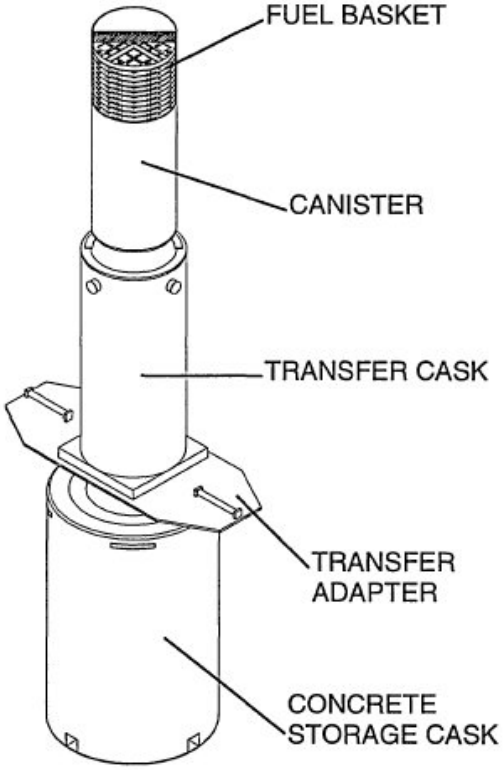

Fig. 1 Basic NAC-UMS design (from Ref. 8).

consisting of a homogenized mix of all the materials present within the fuel basket region. All the dimensions and material compositions for the model were obtained directly from Ref. 8.

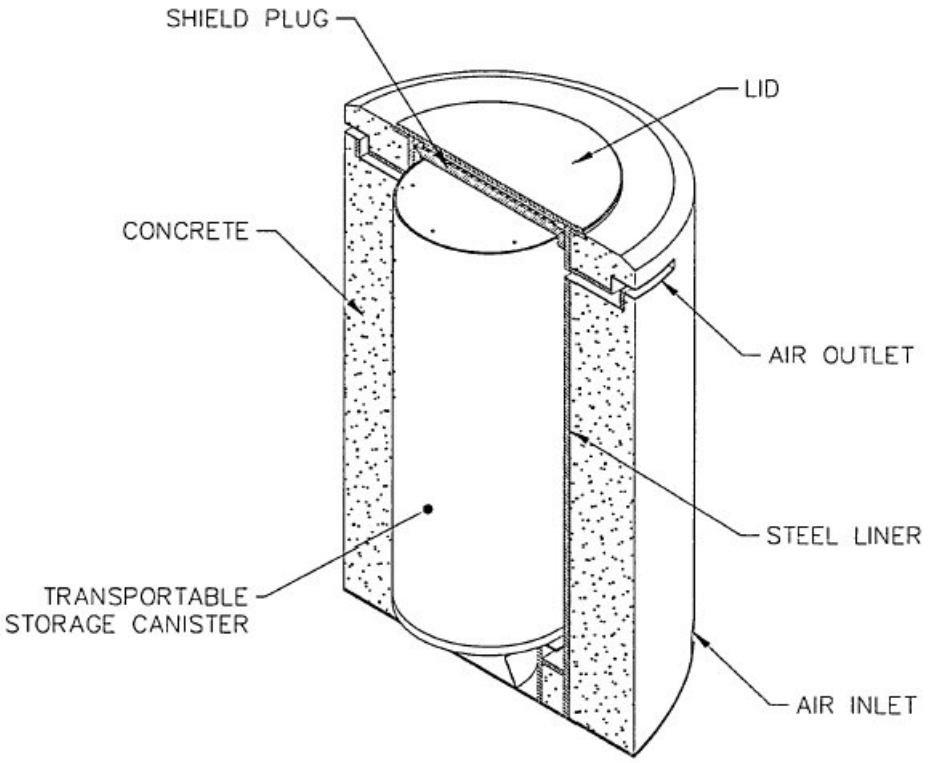

Fig. 2 NAC-UMS canister and vertical concrete cask arrangement (from Ref. 8).

The result of the geometric modeling process, after adding a few extra zones for edit purposes, is shown in Fig. 3. This material map was generated by the Plot_Vgeo Matlab script file that reads the basic geometry information -- mesh layout, zone by mesh, and the material by zone mapping -- and produces a visual representation to aid in the model set up and debugging process (see Refs. 6-7 for a brief description of some of the utility codes in use at UMass-Lowell). The base data for the model are contained in a set of informal spreadsheets, which are summarized here as Tables 1-3. These tables contain the model's region boundaries, a description of the various zone assignments, and the actual zone map used to generate Fig. 3.

The data given in Tables 1-3 should provide all the details needed to fully utilize and understand the UMS model generated for this study. In particular, Table 1 shows the specific mesh spacing used and that the final RZ model has a 123x220 fine mesh grid structure within a 14x23 grid of coarse region boundaries. Tables 2 and 3 give the zone designations and the location within the model of each zone (i.e. the zone by region map). Note that the maximum zone number is 85, but not all the zone numbers are actually used -- this is done for added flexibility in making changes to the model. The geometry information given here can be used to correlate the results in later sections to various regions within the model.

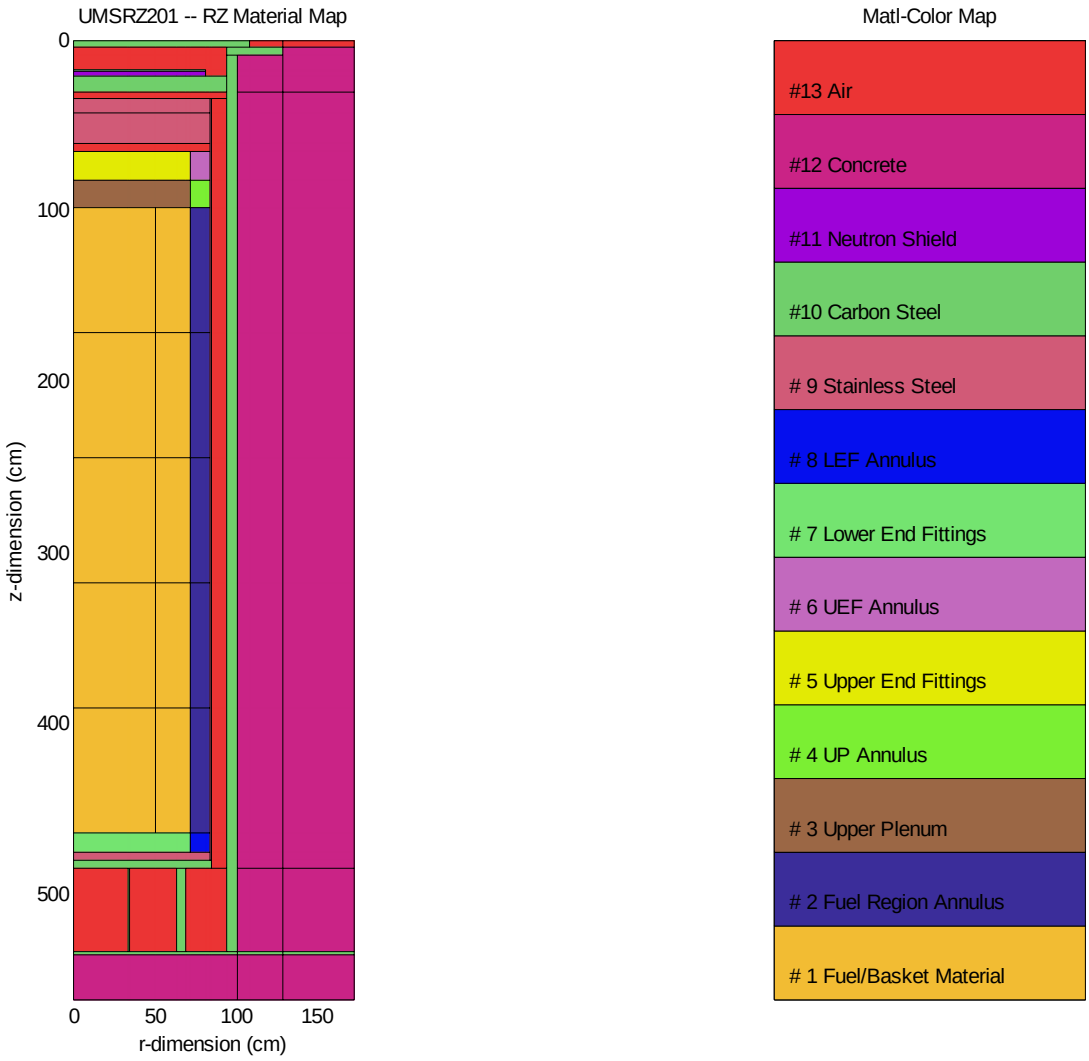

Fig. 3 Material map for the DORT RZ computational geometry.

Table 1 Region boundaries for the DORT RZ model.

R-Direction Region Boundaries (Mesh spacing about 1 - 1.6 cm)

Column #	Primary Region Description	Radius inches	Radius cm	# Mesh	Mesh Delta R cm	Total Mesh
0	centerline of RZ model	0.0000	0.0000			
1	Ri for baffle	13.0000	33.0200	25	1.321	25
2	Ro for baffle (0.5" thick)	13.5000	34.2900	1	1.270	26
3	Ro for inner fuel region	19.9590	50.6959	12	1.367	38
4	Ri for support structure	25.0000	63.5000	9	1.423	47
5	Ro for support structure	27.0000	68.5800	4	1.270	51
6	Ro for outer fuel region	28.2260	71.6940	2	1.557	53
7	Ro for neutron shield	32.0000	81.2800	7	1.369	60
8	Ri for canister radial shell	32.9050	83.5787	2	1.149	62
9	Ro for canister radial shell	33.5300	85.1662	1	1.588	63
10	Ri for VCC shell	37.2500	94.6150	7	1.350	70
11	Ro for VCC shell	39.7500	100.9650	5	1.270	75
12	Ro for cask lid	42.8000	108.7120	6	1.291	81
13	Ro for top flange on VCC cask	50.7000	128.7780	14	1.433	95
14	Ro for radial concrete region	68.0000	172.7200	28	1.569	123

Z-Direction Region Boundaries (Mesh spacing about 2.0 - 2.8 cm -- except for NS)

Row #	Primary Region Description	Delta Z inches	Total Z inches	Total Z cm	# Mesh	Mesh Delta Z cm	Total Mesh
0	top of RZ model	0.0000	0.0000	0.0000			
1	cask lid	1.5000	1.5000	3.8100	2	1.905	2
2	air gap above neutron shield	2.0000	3.5000	8.8900	2	2.540	4
3	air gap above neutron shield	3.3750	6.8750	17.4625	5	1.715	9
4	VCC neutron shield cover	0.3750	7.2500	18.4150	1	0.953	10
5	VCC neutron shield	1.0000	8.2500	20.9550	2	1.270	12
6	VCC shield plug	3.7500	12.0000	30.4800	5	1.905	17
7	air gap above canister	1.6300	13.6300	34.6202	2	2.070	19
8	canister structural lid	3.0000	16.6300	42.2402	3	2.540	22
9	canister shield lid	7.0000	23.6300	60.0202	7	2.540	29
10	fuel/basket He gap	2.0300	25.6600	65.1764	2	2.578	31
11	fuel/basket upper end fittings	6.7200	32.3800	82.2452	7	2.438	38
12	fuel/basket upper plenum region	6.2600	38.6400	98.1456	6	2.650	44
13	fuel/basket region	28.8000	67.4400	171.2976	28	2.613	72
14	fuel/basket region	28.8000	96.2400	244.4496	28	2.613	100
15	fuel/basket region	28.8000	125.0400	317.6016	28	2.613	128
16	fuel/basket region	28.8000	153.8400	390.7536	28	2.613	156
17	fuel/basket region	28.8000	182.6400	463.9056	28	2.613	184
18	fuel/basket lower end fittings	4.2900	186.9300	474.8022	4	2.724	188
19	bottom canister plate	1.7500	188.6800	479.2472	2	2.223	190
20	base plate (canister support)	2.0000	190.6800	484.3272	2	2.540	192
21	air/support region	19.0000	209.6800	532.5872	18	2.681	210
22	bottom plate on VCC	1.0000	210.6800	535.1272	1	2.540	211
23	concrete base pad	10.0000	220.6800	560.5272	9	2.822	220

Table 2 Zone descriptions for the DORT RZ model.

Description	Zone Numbers	Description	Zone Numbers
Fuel/Basket Regions		**Vertical Concrete Cask**	
inner fuel	1 - 5	bottom plate	49 - 51
outer fuel	6 - 10	baffle structure	52
radial fuel gap	11 - 15	support structure	53
lower end fittings	16 - 17	base plate for canister	54
plenum region	18 - 19	air gaps (lower)	55
upper end fittings	20 - 21	air gap (radial)	56
upper He gap	22	air gap (upper)	57
not used	23 - 25	shield plug	58
		neutron shield	59
Canister Regions		neutron shield cover	60
canister bottom plate	26	top air region	61
shield lid	27	cask lid	62
structural lid	28	top flange	63
canister shell	29	VCC shell	64
not used	30 - 48	concrete outer shell	65 - 70
		not used	71 - 80
Extras			
air above concrete	81 - 82		
bottom concrete pad	83 - 85		

Table 3 Zone by region map for the DORT RZ model.

column	1	2	3	4	5	6	7	8	9	10	11	12	13	14
row														
1	62	62	62	62	62	62	62	62	62	62	62	62	81	82
2	61	61	61	61	61	61	61	61	61	61	63	63	63	66
3	61	61	61	61	61	61	61	61	61	61	64	65	65	66
4	60	60	60	60	60	60	60	61	61	61	64	65	65	66
5	59	59	59	59	59	59	59	61	61	61	64	65	65	66
6	58	58	58	58	58	58	58	58	58	58	64	65	65	66
7	57	57	57	57	57	57	57	57	57	57	64	67	67	68
8	28	28	28	28	28	28	28	28	29	56	64	67	67	68
9	27	27	27	27	27	27	27	27	29	56	64	67	67	68
10	22	22	22	22	22	22	22	22	29	56	64	67	67	68
11	20	20	20	20	20	20	21	21	29	56	64	67	67	68
12	18	18	18	18	18	18	19	19	29	56	64	67	67	68
13	5	5	5	10	10	10	15	15	29	56	64	67	67	68
14	4	4	4	9	9	9	14	14	29	56	64	67	67	68
15	3	3	3	8	8	8	13	13	29	56	64	67	67	68
16	2	2	2	7	7	7	12	12	29	56	64	67	67	68
17	1	1	1	6	6	6	11	11	29	56	64	67	67	68
18	16	16	16	16	16	16	17	17	29	56	64	67	67	68
19	26	26	26	26	26	26	26	26	29	56	64	67	67	68
20	54	54	54	54	54	54	54	54	54	56	64	67	67	68
21	55	52	55	55	53	55	55	55	55	55	64	69	69	70
22	49	49	49	49	49	49	49	49	49	49	49	50	50	51
23	83	83	83	83	83	83	83	83	83	83	83	84	84	85

To complete the DORT modeling, a series of user options and convergence parameters are selected for a given run. In particular, all the computations performed here used a symmetric S16 quadrature set (160 angles), a P3 scattering representation, a fission source convergence of 1.0e-3, and the zone-dependent pointwise flux convergence option in DORT -- where all the important zones within and near the fuel region have a convergence criterion of 5.0e-4. The maximum relative flux change per iteration was relaxed somewhat in the outer portions of the model (outer concrete shell, carbon steel plate and concrete pad at the bottom of the model, etc.).

Cross Section and Response Library Information

In addition to the computational geometry described above, a problem-specific coupled neutron-gamma macroscopic multigroup cross section library is also needed to perform the DORT radiation transport analysis. The BUGLE-96 47 neutron group and 20 gamma group library[4] was chosen for use here since we have a lot of experience with this library at UMass-Lowell and it is used extensively in the nuclear community for radiation transport calculations similar to those required here. With the availability of BUGLE-96, generating the macroscopic cross sections needed for the 13 materials used within the DORT calculations (see list in Fig. 3) simply requires a table of homogenized material densities and a relatively simple mixing operation within the GIP code (GIP is distributed along with DORT as part of the DOORS 3.2 package[3]). The specific material data used here are given in Table 4 (these data were obtained primarily from Ref. 8). Note also that, with use of the BUGLE-96 library, a preliminary mixing step is required to create the natural Fe, Ni, and Cr elements based on the distribution of the naturally occurring isotopes that comprise each of these elements.

Along with the base cross sections needed for the transport calculations, one also often needs a set of response functions to convert the computed fluxes into the desired responses of interest in a particular analysis. As mentioned earlier, the air dose rate throughout the SNF storage configuration is the primary response of interest in this study, since this information will be used to guide the planned experimental program. In addition, however, a set of flux to biological dose conversion factors was also of interest since these will allow direct comparison to some results given in Ref. 8.

The neutron and gamma dose rate response functions were generated with the use of a short Matlab program, mkerma, that takes the nuclide-dependent kerma factors distributed as part of the BUGLE-96 library and, along with the proper material densities, generates a macroscopic kerma factor for the material of interest. The goal here is to generate the desired response function in a consistent group structure for use in several utility codes for post processing the DORT flux solution. Fig. 4 contains a plot of the resultant neutron and gamma kerma factors for air, with units of rad/hr per unit flux.

As indicated, the flux to biological dose conversion factors were needed for comparison to some results tabulated in the NAC-UMS FSAR. Several specific data points for the desired response function are given in Tables 5.4 and 5.5 in the Radiation Shielding text by Chilton et. al. (see Ref. 9). The Chilton data were processed in a short Matlab code, bio_resp_func, and averaged over the BUGLE-96 energy group structure to convert the pointwise data to proper form for later use in post processing the DORT results. In addition, these 47/20 group flux to biological dose conversion factors, with units of mrem/hr, were compared to similar data from Ref. 8 (which used a different group structure). The results of this comparison are summarized in Fig. 5, which

Table 4 Material compositions (atom/b-cm) for the NAC-UMS DORT RZ calculations.

Material	^{10}B	^{12}C	^{16}O	Al	Cr	^{55}Mn	Fe	Ni	Zirc	^{235}U	^{238}U	H	Ca	Na	Si
# 1 Fuel/Basket Material	1.909e-4	2.398e-4	9.604e-3	1.995e-3	8.378e-4	8.346e-5	2.853e-3	3.711e-4	2.967e-3	3.457e-5	4.767e-3	0.0	0.0	0.0	0.0
# 2 Fuel Region Annulus	0.0	0.0	0.0	5.678e-3	1.693e-3	1.686e-4	5.764e-3	7.498e-4	0.0	0.0	0.0	0.0	0.0	0.0	0.0
# 3 Upper Plenum	0.0	0.0	0.0	0.0	2.271e-3	2.262e-4	7.733e-3	1.006e-3	2.967e-3	0.0	0.0	0.0	0.0	0.0	0.0
# 4 UP Annulus	0.0	0.0	0.0	0.0	1.343e-3	1.338e-4	4.573e-3	5.948e-4	0.0	0.0	0.0	0.0	0.0	0.0	0.0
# 5 Upper End Fittings	0.0	0.0	0.0	0.0	2.759e-3	2.749e-4	9.396e-3	1.222e-3	0.0	0.0	0.0	0.0	0.0	0.0	0.0
# 6 UEF Annulus	0.0	0.0	0.0	0.0	2.501e-3	2.492e-4	8.519e-3	1.108e-3	0.0	0.0	0.0	0.0	0.0	0.0	0.0
# 7 Lower End Fittings	0.0	0.0	0.0	0.0	3.203e-3	3.191e-4	1.091e-2	1.419e-3	0.0	0.0	0.0	0.0	0.0	0.0	0.0
# 8 LEF Annulus	0.0	0.0	0.0	0.0	3.918e-3	3.904e-4	1.334e-2	1.736e-3	0.0	0.0	0.0	0.0	0.0	0.0	0.0
# 9 Stainless Steel	0.0	0.0	0.0	0.0	1.651e-2	0.0	6.320e-2	6.501e-3	0.0	0.0	0.0	0.0	0.0	0.0	0.0
# 10 Carbon Steel	0.0	3.925e-3	0.0	0.0	0.0	0.0	8.350e-2	0.0	0.0	0.0	0.0	0.0	0.0	0.0	0.0
# 11 Neutron Shield	8.507e-5	2.260e-2	2.610e-2	7.800e-3	0.0	0.0	0.0	0.0	0.0	0.0	0.0	5.850e-2	0.0	0.0	0.0
# 12 Concrete	0.0	0.0	4.493e-2	1.702e-3	0.0	0.0	3.386e-4	0.0	0.0	0.0	0.0	1.340e-2	1.483e-3	1.704e-3	1.621e-2
# 13 Air	0.0	0.0	5.085e-5	0.0	0.0	0.0	0.0	0.0	0.0	0.0	0.0	0.0	0.0	0.0	0.0

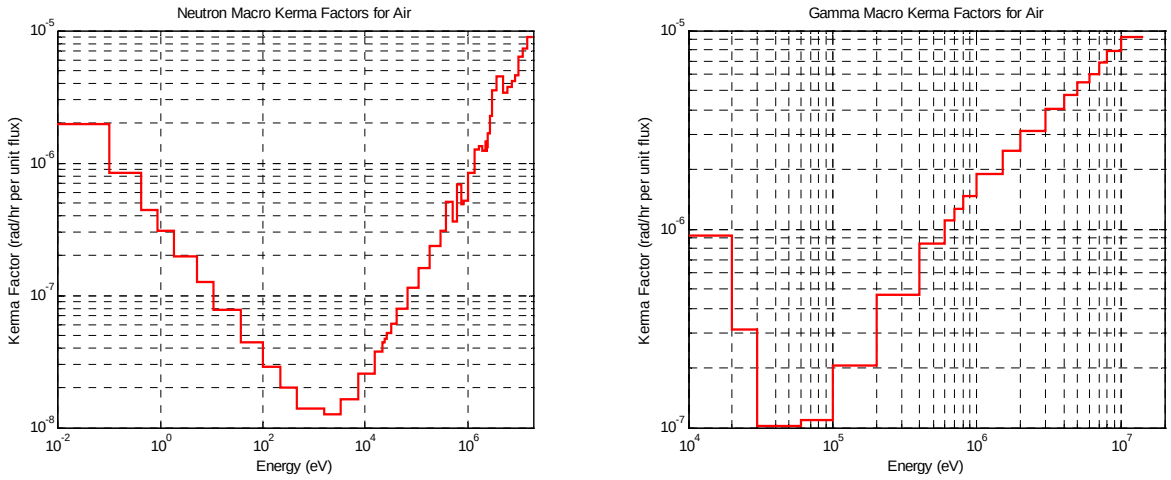

Fig. 4 Neutron and gamma kerma factors for air (rad/hr per unit flux).

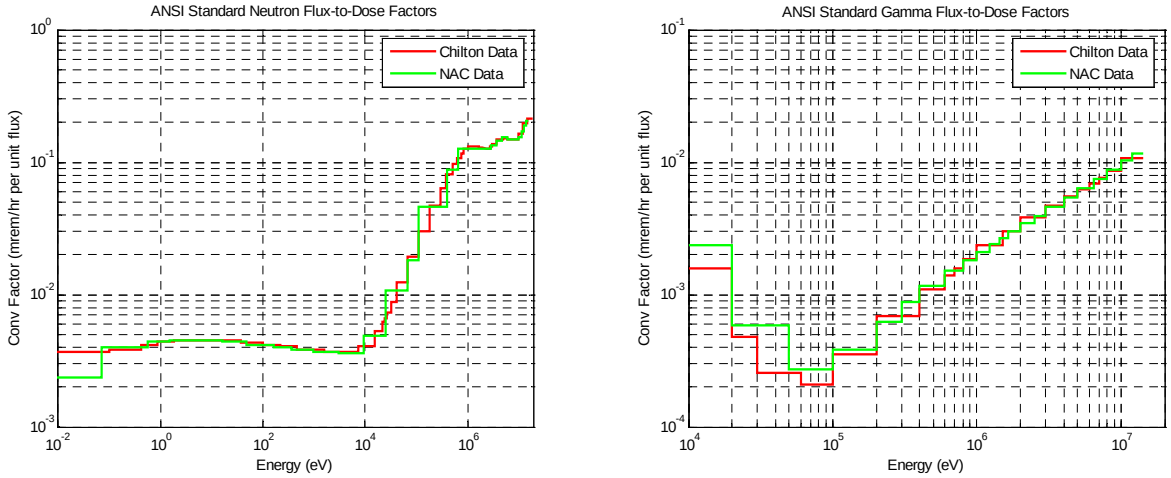

Fig. 5 Validation of flux to biological dose conversion factors (mrem/hr per unit flux).

shows that the two response functions are indeed similar. The good agreement seen here will allow direct comparison of cask surface dose estimates from the current work with the data from Ref. 8.

Source Generation and Analysis for a WE17x17 Assembly

The final task needed to complete the input for the DORT calculation is to quantify the neutron and gamma sources within a typical fuel assembly, and then to properly format this distributed source for use within the DORT RZ computational model. As noted previously, for spent nuclear fuel (SNF) applications, the neutron source is due primarily to actinide spontaneous fission and alpha decay, and the subsequent α,n reactions that occur in the fuel. The gamma source is the result of the radioactive decay of both the fission products and actinides in the fuel, as well as from the decay of activation products within the fuel hardware in both the active fuel region and the end fittings of the fuel assembly. For the preliminary calculations reported here,

only the gammas from the fission products and actinides in the fuel are treated -- the additional gamma source associated with the activated assembly hardware will be included in subsequent work. Thus, the present work is focused only on the neutron and gamma source due to the fission products and actinides within the active fuel region.

To determine the desired neutron and gamma sources, an ORIGEN fuel depletion calculation is performed that models the behavior of a particular fuel assembly during the full lifetime of the element, while in the core and after removal from the reactor. A standard Westinghouse PWR 17x17 assembly design was chosen as a typical PWR fuel element. In particular, a 17x17 assembly with 264 fuel pins and 25 instrument guide tubes was modeled using the data in the top part of Table 5 (the base data are from Ref. 8). Using a UO_2 density of 10.5 g/cm^3, an average burnup of 40000 MWD/MTU, and the geometry, enrichment, and average power generated per assembly from Table 5, one can compute all the parameters needed to run the desired ORIGEN calculation. The needed inputs include the mass per assembly of the individual nuclides associated with the fuel pins and the guide tubes, the THERM, RES, and FAST spectrum parameters that can be obtained from a 1-D pin cell calculation, and the full power days that the fuel is at power. The lower half of Table 5 summarizes these computed parameters.

The ORIGEN run includes the computed data from Table 5, the group boundaries for generating the multigroup neutron and gamma source spectra, and the shutdown time intervals for computation and edit of the desired source information. The quantities of interest here are the source magnitudes and spectra versus time after shutdown.

Table 5 Base and derived data for a Westinghouse 17x17 fuel assembly design.

Base Data					
Fuel Rod Data		**Instrument Guide Tube Data**		**Other Parameters**	
# of fuel rods	264	# of tubes	25	assembly power (MW)	18.48
rod pitch (in)	0.496	tube diameter (in)	0.482	assembly burnup (MWD/MTU)	40000
rod diameter (in)	0.374	tube thickness (in)	0.016	cooling time (years)	5
clad material	Zirc-4	tube material	Zirc	UO2 density (g/cc)	10.5
clad thickness (in)	0.0225				
pellet diameter (in)	0.3225				
initial enrich (w/o)	3.7				
active fuel length (in)	144				
pins along one side	17				
Derived Data					
Assembly Masses (g)		**Spectrum Parameters (see Ref. 5 for definitions)**		**Other Data**	
U235	17462	THERM	0.56	full power days	1025
U238	454494	RES	4.93		
O - fuel	63469	FAST	1.72		
Zr	108667				
Cr	1714				
Fe	155				
Ni	66				

As a reference, a minimum cool-down time of 5 years was selected for the current calculations. This is the time that an assembly must spend in the spent fuel pool before it can be moved to a dry storage facility. The ORIGEN results for the neutron and gamma spectra 5 years after shutdown were extracted for use in developing the distributed source for input to DORT. In addition, the magnitudes of the neutron and gamma sources versus time were also recorded so that time integrated effects could be treated within the current study.

The DORT distributed source can be input in a number of different ways. The goal here is to provide the full space and energy dependence of the source distribution where, for the BUGLE-96 group structure (67 groups), the first 47 groups hold the neutron source and the last 20 groups store the gamma source information. However, because the neutron and gamma sources behave differently versus burnup, the spatial distributions of the neutron and gamma sources are different. In particular, since the gamma source is primarily due to fission product decay, the fission product inventory is proportional to the number of fissions, and the term "burnup" is simply a measure of this latter quantity, it makes sense that the gamma source strength is directly proportional to burnup. However, this is not the case for the neutron source since it is related to the higher actinide inventories and these tend to follow a saturation curve versus burnup (buildup and loss tend toward equilibrium at higher burnups). Based on these arguments, correlations for the source strength versus burnup were generated in Ref. 8 and, with a known typical axial burnup profile, one can also generate typical axial profiles for the neutron and gamma sources. Using these data from Ref. 8, the desired profiles were reproduced here -- as shown in Fig. 6 -- and used as an ingredient in the generation of the full distributed source for use in DORT.

Note that Fig. 6 shows that the normalized gamma source profile, which is flat in the fuel center and drops off linearly in the top and bottom 15% of the active fuel length, integrates to nearly unity (as expected). However, the integral of the normalized axial distribution of the neutron source is about 1.12. This happens because of the nonlinear behavior of the neutron source strength with burnup -- thus, the axially integrated neutron source strength is not equal to the source strength associated with the average burnup.

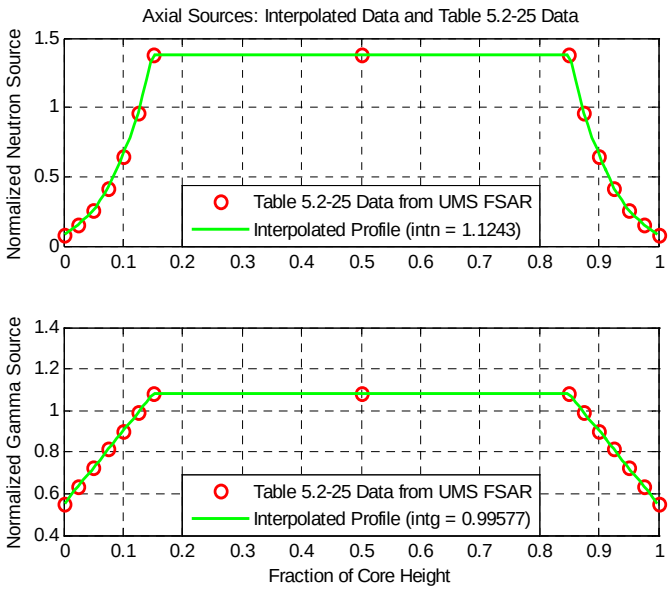

Fig. 6 Axial source profiles used within the DORT RZ model (data from Ref. 8)

To complete the source description, one needs to multiply the ORIGEN-generated source by 24, since there are 24 PWR assemblies in the canister region, and divide by the fuel volume, since DORT expects a distributed source with units of particles/second per unit volume. To automate this, a short Matlab script file was written to perform any necessary manipulations and to put the desired source into final form for input to DORT. The i-profile (r direction) is a constant, 24/volume, within the fuel and zero elsewhere, the j profile (z direction) uses the data from Fig. 6, and the g-profile (energy dependence) is obtained directly from the ORIGEN-generated neutron and gamma spectra at 5 years after shutdown. Multiplying these three components together, being careful to use the different axial profiles for the first 47 groups and last 20 groups, gives the final distributed source used within the DORT analysis. With this distributed source, everything is now available to do the actual DORT computations.

Before moving on to discuss the DORT results, however, we should first address the time dependence that is inherent in these computations. The assumption made here is that the DORT calculated dose rate versus time would follow the same time-dependent shape as the ORIGEN-generated source profile. Thus, if we represent the time dependence of the source as f(t), where $f(t_o) = 1.0$, then we have

Source Strength: $S(t) = S_o f(t)$

Dose Rate: $DR(t) = DR_o f(t)$

and the total integrated dose after t_f years (or hours) becomes

Total Dose: $$TD(t_f) = DR_o \int_{t_o}^{t_o + t_f} f(t)dt$$

The integral in the above expression for total dose can be obtained versus t_f using the data generated in the ORIGEN run, since the shutdown portion of the calculation was continued for over 100 years beyond shutdown. In particular, a Matlab program, we17x17_dose1, was written to plot the f(t) function for both the neutron source and the gamma energy released, and to integrate these for various lifetimes, t_f, for the storage cask. Note that t_o in these analyses represent 5 years after shutdown and that $t_o + t_f$ is the total shutdown time for a cask lifetime of t_f years.

The results from the above analyses are summarized in Fig. 7 and in Table 6. Here we see the expected exponential-type decay associated with the time dependence of the sources and the expected saturation or leveling-off of the integral of f(t) versus lifetime, t_f. One should also note that the integral of f(t) has units of time. Here, time units in hours were chosen so that the integral dose is simply given by (rad/hr)*(hr) = (rads). Also, the time-dependent data are included in both graphical and tabular form in Fig. 7 and Table 6, respectively, so that the results are easy to visualize and so that a numerical factor to convert dose rate to total dose is also readily available. For example, with a given value of DR_o from the DORT calculation, one can determine the total gamma dose for a 30-year lifetime by multiplying DR_o (in rad/hr) by 1.05×10^5 hours (from the last column in Table 6).

As a final point, one should note that both the normalized gamma source and the normalized energy versus time are given in Table 6. The profiles are clearly similar, but slightly different because one treats only the number of photons emitted per second and the other accounts for the change in the energy spectrum as well as the source strength versus time. Thus, for determining integral dose, the gamma energy profile versus time should give a better estimate of the real

quantity of interest. Since the emitted neutron spectrum does not change significantly with time, this type of distinction between source strength versus time and energy emitted versus time is not needed for determining the neutron integral dose.

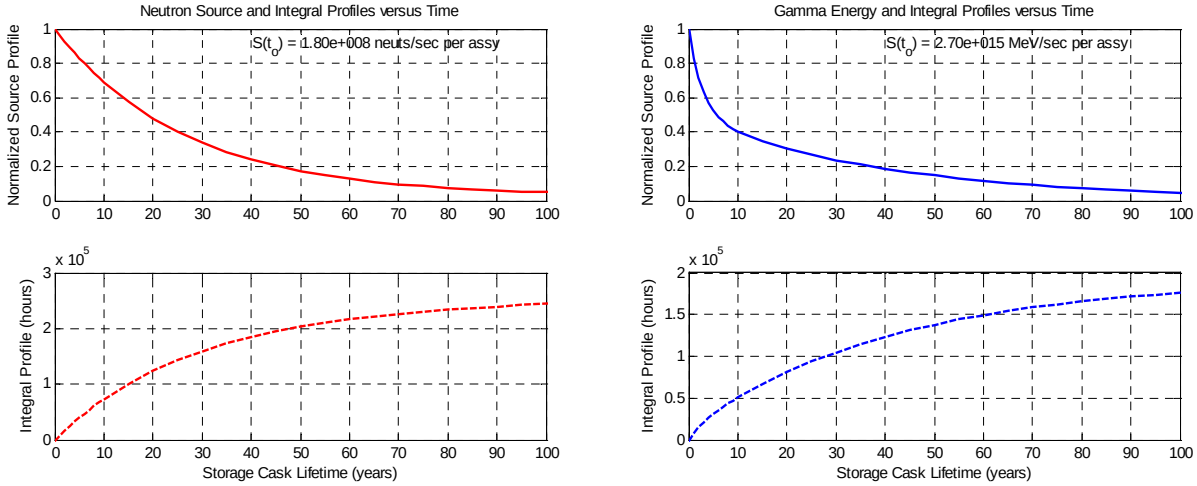

Fig. 7 Time dependence of the dose rate and integral dose.

Table 6 Data for normalized source and integral profiles for the WE17x17 assembly.

	Neutron Source		Gamma Source		Gamma Energy	
Lifetime (years)	**f(t)**	**Integral of f(t) (hours)**	**f(t)**	**Integral of f(t) (hours)**	**f(t)**	**Integral of f(t) (hours)**
0	1.000	0.00E+00	1.000	0.00E+00	1.000	0.00E+00
1	0.961	8.59E+03	0.824	7.99E+03	0.830	8.01E+03
2	0.928	1.69E+04	0.713	1.47E+04	0.715	1.48E+04
3	0.894	2.48E+04	0.640	2.06E+04	0.630	2.07E+04
4	0.861	3.25E+04	0.589	2.60E+04	0.570	2.59E+04
5	0.828	3.99E+04	0.551	3.10E+04	0.526	3.07E+04
6	0.800	4.71E+04	0.521	3.57E+04	0.489	3.52E+04
7	0.772	5.39E+04	0.497	4.02E+04	0.463	3.93E+04
8	0.744	6.06E+04	0.478	4.44E+04	0.437	4.33E+04
9	0.717	6.70E+04	0.460	4.85E+04	0.419	4.70E+04
10	0.689	7.31E+04	0.444	5.25E+04	0.404	5.06E+04
15	0.578	1.01E+05	0.386	7.07E+04	0.345	6.70E+04
20	0.482	1.24E+05	0.341	8.66E+04	0.303	8.12E+04
25	0.403	1.43E+05	0.303	1.01E+05	0.267	9.37E+04
30	0.338	1.60E+05	0.270	1.13E+05	0.237	1.05E+05
35	0.285	1.73E+05	0.241	1.24E+05	0.210	1.15E+05
40	0.241	1.85E+05	0.214	1.34E+05	0.187	1.23E+05
45	0.204	1.95E+05	0.192	1.43E+05	0.166	1.31E+05
50	0.174	2.03E+05	0.171	1.51E+05	0.148	1.38E+05
55	0.149	2.10E+05	0.154	1.58E+05	0.131	1.44E+05
60	0.128	2.16E+05	0.138	1.65E+05	0.117	1.49E+05
65	0.111	2.21E+05	0.124	1.71E+05	0.104	1.54E+05
70	0.097	2.26E+05	0.111	1.76E+05	0.093	1.59E+05
75	0.085	2.30E+05	0.100	1.80E+05	0.083	1.62E+05
80	0.075	2.33E+05	0.090	1.85E+05	0.074	1.66E+05
85	0.067	2.36E+05	0.081	1.88E+05	0.066	1.69E+05
90	0.061	2.39E+05	0.073	1.92E+05	0.059	1.72E+05
95	0.055	2.42E+05	0.067	1.95E+05	0.052	1.74E+05
100	0.050	2.44E+05	0.060	1.98E+05	0.047	1.76E+05

Calculational Results from the DORT RZ Model

With all the pieces available, one can finally complete the DORT input and run the desired calculation. The result of the DORT run is a very large flux file that contains information about the neutron and gamma radiation field throughout the system of interest. This flux file is usually read by some utility codes to extract specific information for several space and/or energy regions of interest in the model. At UMass-Lowell, the PROCESS, FEWGRP, and Plot_Flux codes are commonly used for this purpose.[6-7] In particular, PROCESS and FEWGRP, combined with an appropriate response library, are used to generate 1-D and 2-D response profiles integrated over some energy region. Using this approach, 9 different response profiles were generated to help quantify and visualize the results of the DORT case, as follows:

1. fast neutron flux (E > 0.111 MeV)
2. epithermal neutron flux (0.414 eV < E < 0.111 MeV)
3. thermal neutron flux (E < 0.414 eV)
4. total neutron flux
5. total gamma flux
6. air neutron dose rate (rad/hr)
7. air gamma dose rate (rad/hr)
8. neutron biological dose rate (mrem/hr)
9. gamma biological dose rate (mrem/hr)

where responses 6-9 use the response functions discussed previously (presented in Figs. 4 and 5). These 9 response distributions can then be plotted in different ways using the Plot_Flux code.

Here we present three sets of summary results: neutron and gamma flux profiles, the neutron and gamma dose rates at the top and side surfaces of the cask (for comparison to Ref. 8) and, finally, a series of plots showing the air dose rate distribution throughout the cask geometry. This latter set of results will be used to set guidelines for the concept development and the experimental program to address the viability of the new photocatalytic energy conversion process.

Figures 8 and 9 summarize the neutron and gamma flux profiles. In particular, Fig. 8 gives the radial and axial fast, epithermal, and thermal neutron flux profiles along the centerlines of the system. The log scale highlights the large attenuation that is observed with distance from the source region (fueled canister region). Also, as expected, one sees that there are essentially no thermal neutrons in the dry unmoderated canister region, yet the thermal flux increases quite rapidly, for example, near the concrete portions of the configuration, where the high-energy neutrons can easily moderate to thermal energies.

Figure 9 displays the total neutron and gamma flux profiles along the radial and axial centerlines. Here one sees that the gamma flux is generally orders of magnitude larger than the neutron flux throughout the canister-cask system, except near the top surface of the cask. Also, we can easily see that the gamma flux attenuates very rapidly in the structural regions of the system. For example, in the 10 inches of stainless steel at the top of the canister, the gamma flux drops by more than 5 orders of magnitude. The overall behavior here, in both Figs. 8 and 9, is exactly as expected -- which gives confidence in the validity of the overall computational model.

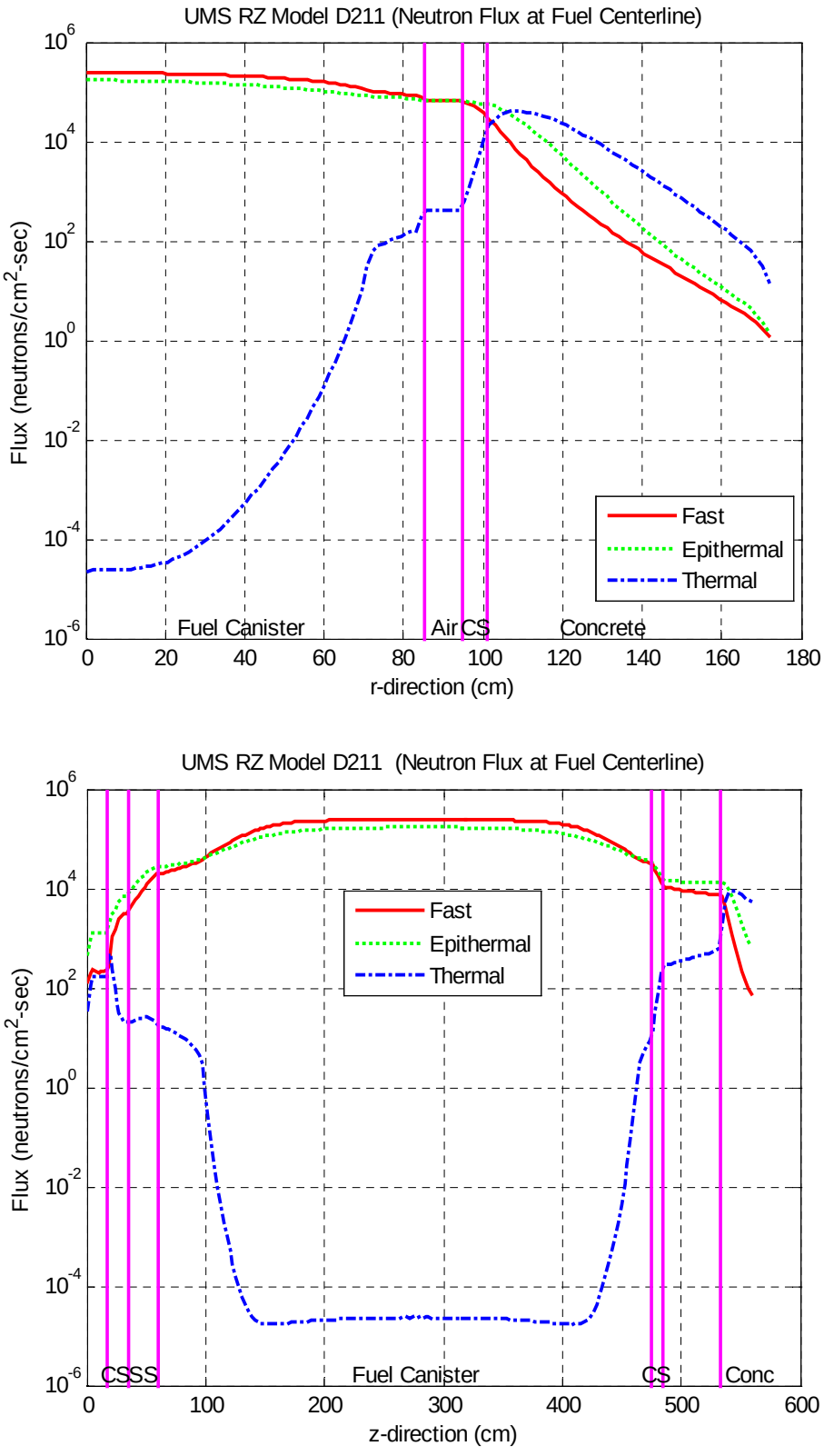

Fig. 8 Neutron flux radial and axial profiles at the fuel centerlines.

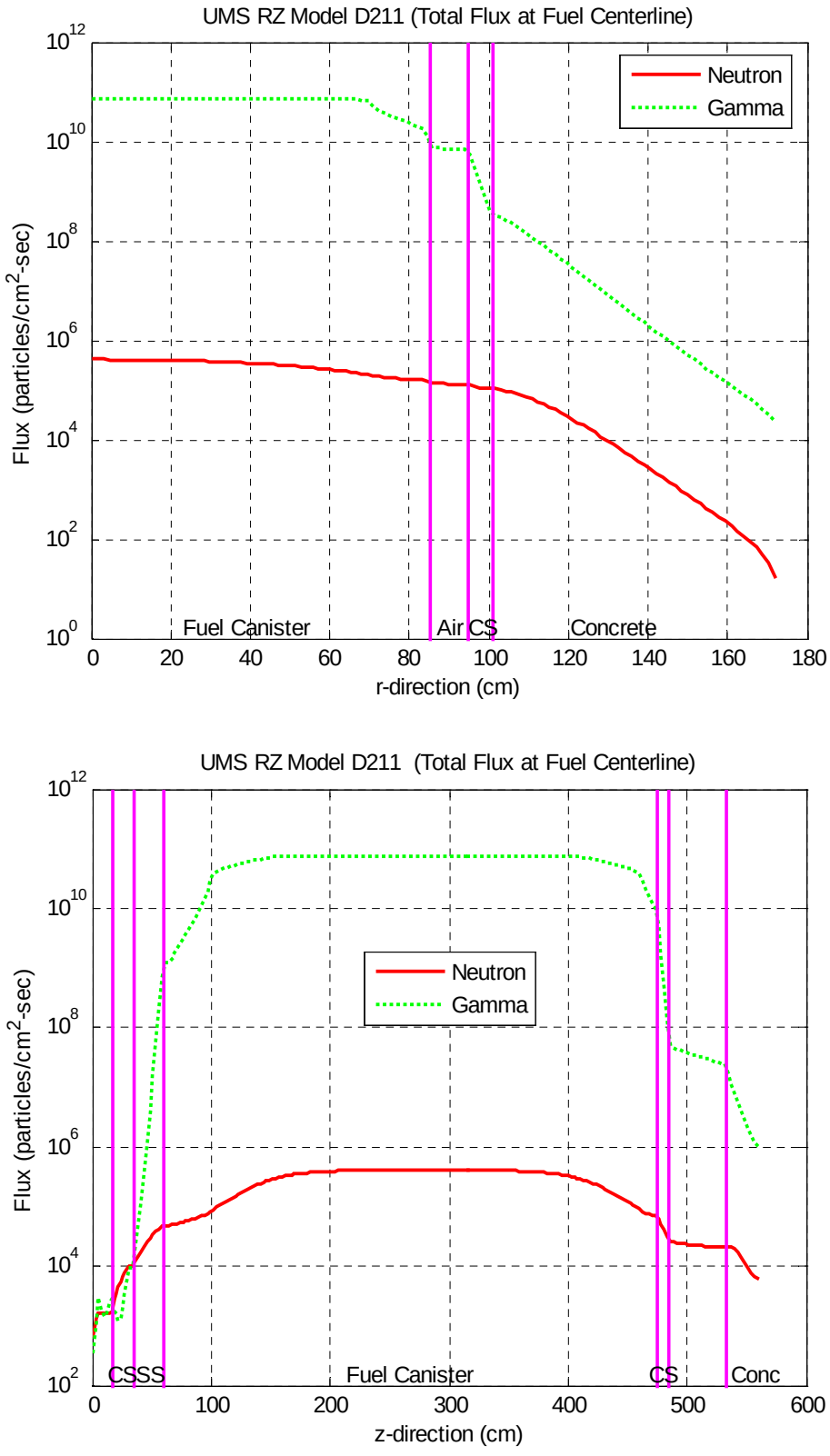

Fig. 9 Total neutron and gamma flux radial and axial profiles at the fuel centerlines.

In the NAC UMS FSAR (Ref. 8), the focus of the shielding analysis is on the biological dose at the surface of the cask and at various distances from the cask surface. In the current study, however, the region of interest is internal to the cask structure in the vicinity of the fuel canister where the radiation levels are high enough to support a photocatalytic energy conversion system. The two analyses are quite different -- here we use a 2-D axisymmetric deterministic model and the work in Ref. 8 used a detailed 3-D Monte Carlo model of the system. Nevertheless, a comparison of the two studies, with a focus on the qualitative behavior of the surface dose rates, can give a quick check of the general consistency of the two models.

To aid in the comparison, Fig. 10 shows the surface biological dose profiles obtained from the DORT RZ model. On the top surface, the neutron dose rate is the larger dose component out to about 20 cm into the radial concrete shield. There is a peak in both the neutron and gamma dose rate in the radial location of the air gap outside the fuel canister. At this point, the neutron dose rate is about 22 mrem/hr on the top surface of the cask. The DORT-calculated neutron dose rate agrees very well with the data in Ref. 8 (peaks at about 25 mrem/hr), but the gamma dose rate due to the fuel gammas is larger here than in Ref. 8 (not sure why?).

On the outer radial surface, the gamma dose component dominates. Reference 8 reports a peak in the azimuthal average dose rate of about 32 mrem/hr, and this compares reasonably well to the DORT value for the axisymmetric model of about 21 mrem/hr. Considering the differences in the models and the differences in the reported results, these general comparisons are quite reasonable -- and they give some additional confidence in the validity of the mathematical model and the tools used in the current study.

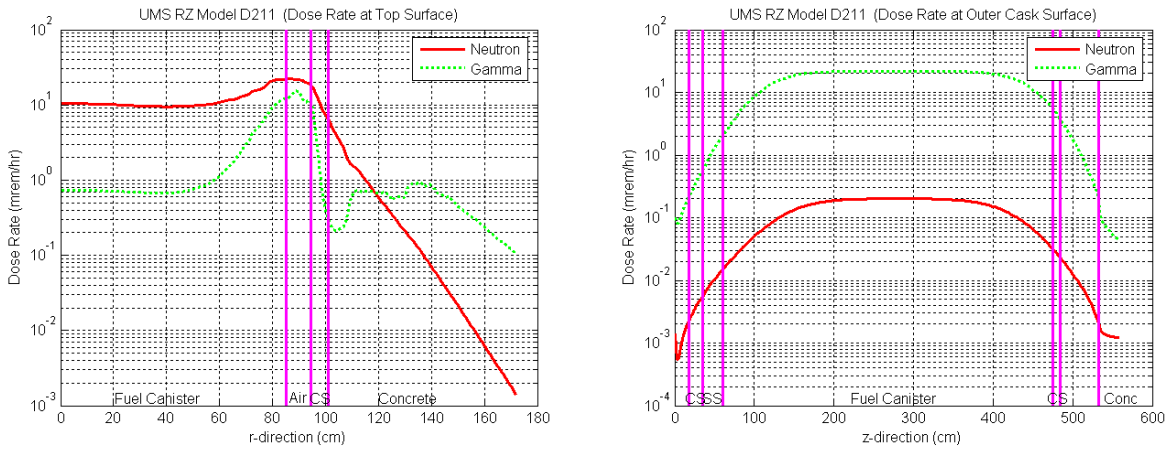

Fig. 10 Neutron and gamma biological dose rate profiles along cask surfaces.

The quantity of primary interest in the current work is the air dose rate distribution throughout the canister-cask geometry. As before, a quantitative perspective of the dose rate distribution is shown in Fig. 11, where the gamma and neutron dose rates along the radial and axial centerlines of the model are displayed. These curves clearly show that the neutron component is negligible, and that the gamma dose rates drop off very rapidly in the stainless steel (SS) and carbon steel (CS) structural components. This is also shown in a more qualitative sense in Fig. 12, which shows the gamma dose rate throughout the RZ model. The log of the dose rate is displayed so that one can see the large range in values that occur. In particular, one sees that the peak dose rate of nearly 10^5 rad/hr decreases very rapidly just outside the fueled region, and drops off to as low as 10^0 - 10^{-5} rad/hr outside the main structure/shield regions.

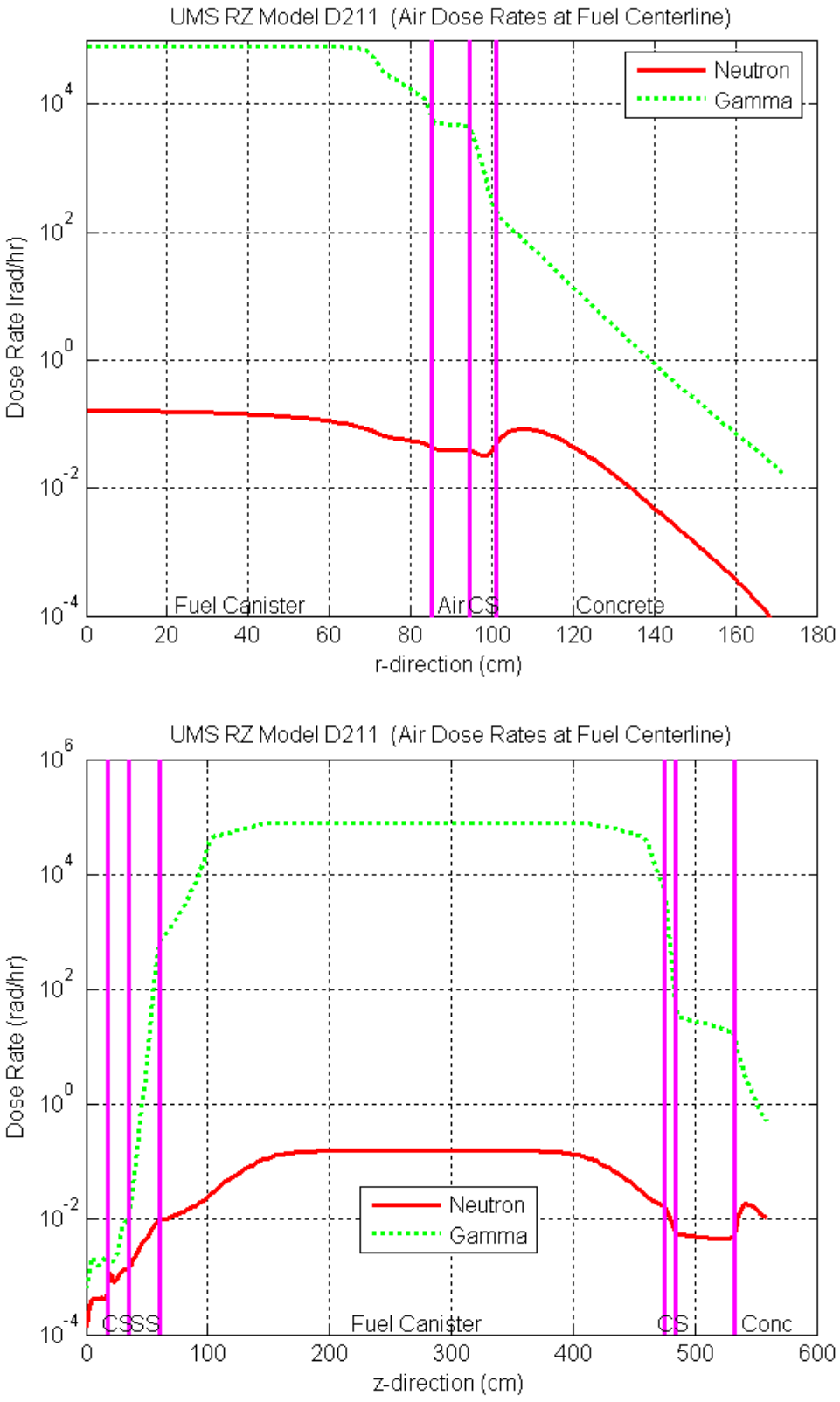

Fig. 11 Neutron and gamma air dose rate profiles along fuel centerlines.

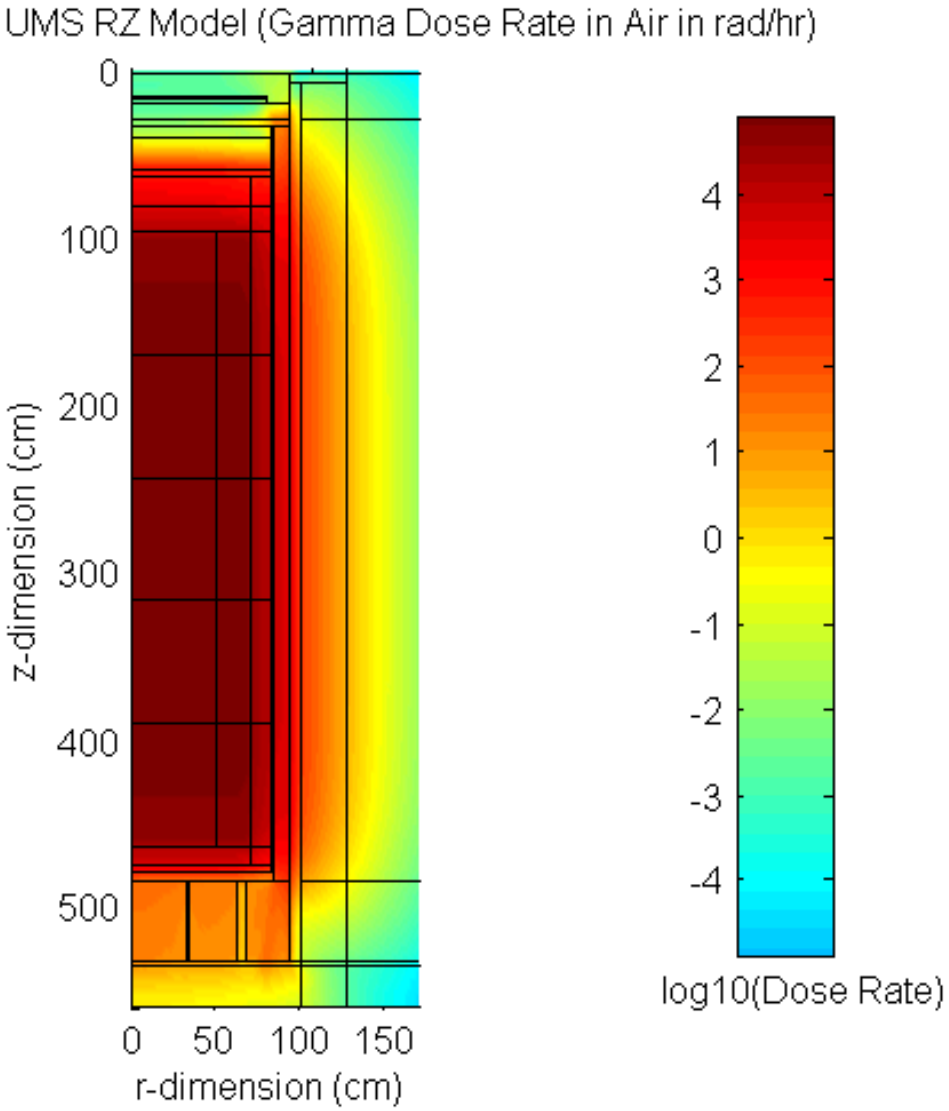

Fig. 12 Gamma air dose rate distribution throughout canister-cask geometry.

Although there is no experimental data, as yet, to identify the power production capability of the proposed photoconverter materials versus dose rate, we expect a low cutoff of about 100 rad/hr as a minimum useful dose rate. With this rough estimate as a lower limit, one sees from Figs. 11 and 12, that the viable regions for placement of the photoconverter materials are limited to the region just below the stainless steel canister lid within the cask shell-concrete interface region. If we also exclude the actual fuel region -- because of the potentially high temperatures present -- then the three most promising areas include the following:

1. Canister shell and radial air gap region (about 8000 - 10000 rad/hr),
2. Gap above the fuel (about 800 - 1000 rad/hr), and
3. Cask shell-concrete interface (about 150 - 200 rad/hr).

The detailed gamma dose rate profiles at these locations, plotted on a linear scale, are given in Figs. 13 - 15, respectively. Thus, from the current preliminary analysis, these regions appear to be the most promising areas for further focus. They offer a range of potential gamma dose rates to air ranging from about 100 rad/hr to 10000 rad/hr or more. Independent of the other factors involved (such as the environmental temperature, for example), this range of dose rates should allow some flexibility in the design and placement of a photocatalytic energy conversion system.

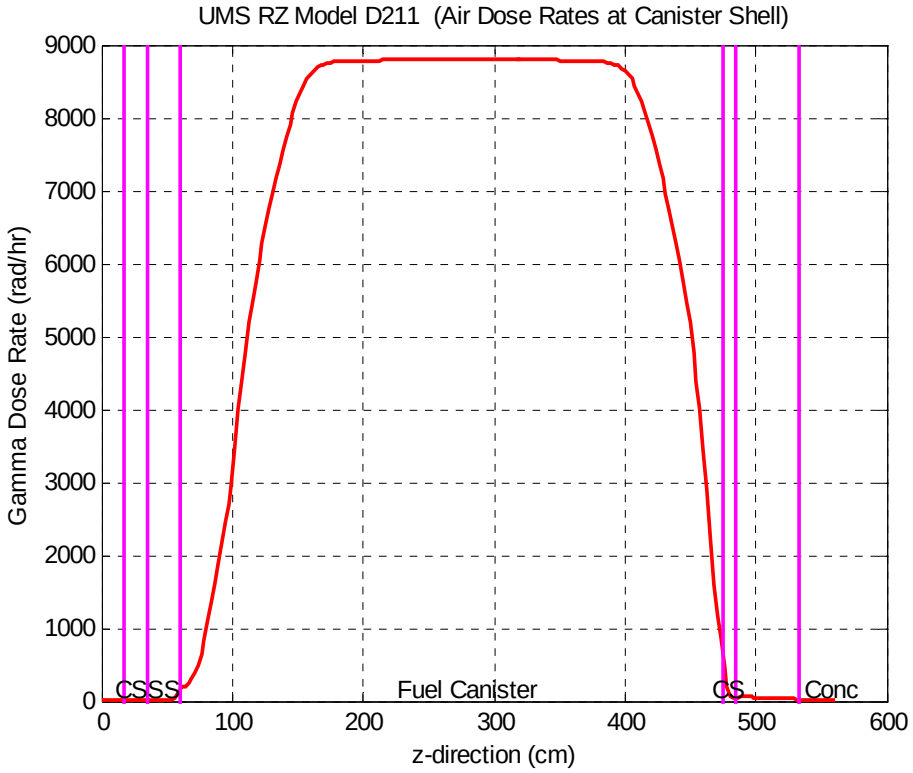

Fig. 13 Gamma dose rate axial profile at the canister shell.

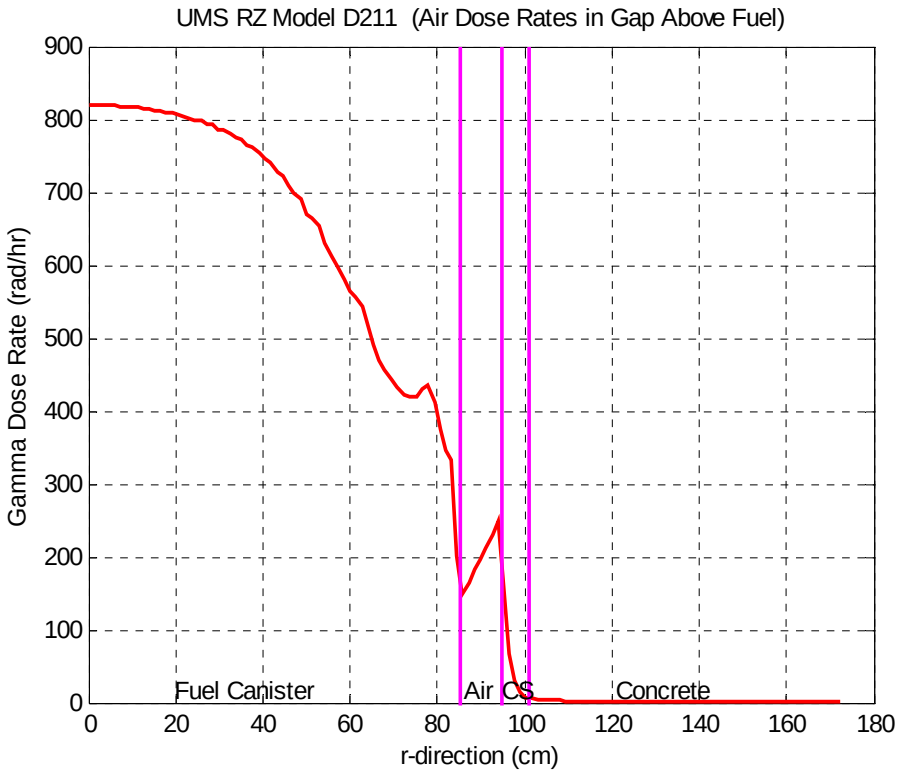

Fig. 14 Gamma dose rate radial profile in the gap above the fuel.

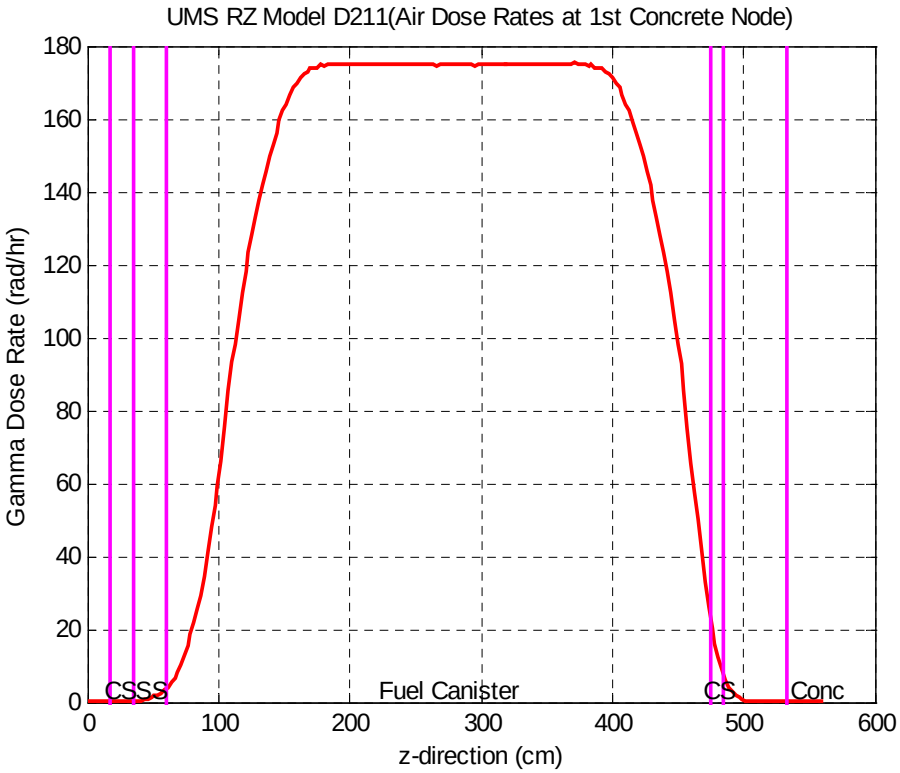

Fig. 15 Gamma dose rate axial profile at cask shell-concrete interface.

Conclusions and Recommendations for the Testing Program

The goal of this study was to estimate the neutron and gamma dose rates and lifetime doses in air throughout a typical SNF storage configuration to support an experimental program for testing photoconverter materials for use in a new photocatalytic energy conversion process. The NAC Universal Multipurpose Cask System (NAC-UMS) was chosen as the typical storage configuration for the current study. The results presented here are considered preliminary primarily because more work is needed to define all the gamma source components needed for the DORT transport calculations. In the current calculations, only the gammas from the fission products and actinides within the fuel are treated -- the additional gamma source associated with the activated fuel assembly hardware within the active fuel region and in the fuel end regions and plenna will need to be included in subsequent work. This additional source could increase the computed air dose rates by a factor of 2 - 3 or more in some regions of the canister-cask geometry. Thus, the results presented in the previous section must be treated as only preliminary estimates of the real expected radiation environment for the conditions specified in the DORT calculations.

However, it should be emphasized that loading the fuel storage canister with 24 PWR assemblies that all have the design basis average burnup of 40000 MWD/MTU, and the minimum allowed cooling time of 5 years, is probably not very realistic for a typical cask loading. Note that the configuration modeled here represents the harshest conditions expected -- meaning that the radiation environment in a typical configuration will have lower dose rates than observed for the design basis configuration. Qualitatively, we expect that the dose rate estimates computed here to be more consistent with the typical cask loading rather than the design basis configuration -- because of the missing gamma source components. Thus, we expect that the current dose estimates to be quite representative and they should be sufficient to guide the experimental program and overall concept development for the photocatalytic energy conversion system. Establishing more accurate worse-case dose rates for the design basis configuration will require proper treatment of the missing gamma source components -- and this will be done in a later phase of the overall project.

With an understanding that the results presented earlier probably represent typical conditions, we can use these data to specify some suggestions to guide the material irradiation program. The first rather obvious conclusion, based on the relative importance of the neutron and gamma dose rates (see Fig. 11), is that no neutron irradiation tests will be required, at least in the early phases of this project. Thus, all our emphasis at this point should be on gamma testing.

Now, for the gamma component, it appears that the expected gamma dose rates will vary significantly with placement within the canister-cask configuration, with potentially useful dose rates as low as about 100 rad/hr for placement of the photoconverter material at the liner-concrete interface to dose rates as high as 10000 rad/hr or more if the energy-conversion materials are placed on the fuel side of the cask's concrete liner (in the air gap). This range is quite large! To establish an upper bound for all normal conditions and useful locations within the system, and to account for possible design basis conditions, dose rates as high as 25000 rad/hr should be considered as part of the experimental program.

Thus, one suggestion for a materials characterization program that evaluates the power generation capability versus dose rate would include 10 different gamma dose rate points ranging from 100 rad/hr to 25000 rad/hr as indicated in Table 7. Also included here, as an example, is

the estimated integral dose for a 30-year lifetime corresponding to the given initial dose rate. The integral dose values simply identify a range for the expected total 30-year integrated gamma dose to the photoconverter material. Thus, we see that 30-year integral doses of 10 Mrad to 2600 Mrad are possible.

Table 7 Possible gamma dose rates and estimated 30-year integral doses for the testing program.

Dose Rate (rad/hr)	100	200	500	1000	2000	5000	10000	15000	20000	25000
Integral Dose (Mrad)	10.5	21.0	52.5	105	210	525	1050	1575	2100	2625

Assuming adequate power production characteristics for the range of dose rates given in Table 7, and stable behavior at lower total doses, one plan for evaluating power generation and generic material behavior versus total dose would include the following nine total dose points: 0, 50, 100, 200, 500, 1000, 1500, 2000, and 2500 Mrad. Of course, a full matrix of 10 x 9 = 90 combinations of dose rate and integral dose conditions is not necessary, since the lower dose rates will never lead to the larger integrated doses. A more reasonable combination of dose rate and integral dose pairs is indicated in Table 8, where an x in a given bin implies that the photo-converter material would be tested at this dose rate and integral dose combination. As apparent, after a more comprehensive evaluation of the unirradiated material (at zero integrated dose), only three dose rate values would be required for each integral dose. This only gives 30 unique combinations for testing where, of course, the decision to test a particular material at the next higher integrated dose would only be made after favorable evaluation at the lower levels.

Table 8 Possible gamma dose rate and integral dose combinations for the testing program.

Integral Dose (Mrad) Dose Rate (rad/hr)	**0**	**50**	**100**	**200**	**500**	**1000**	**1500**	**2000**	**2500**
100	x	x							
200	x	x	x						
500	x	x	x	x					
1000	x		x	x	x				
2000	x			x	x	x			
5000	x				x	x	x		
10000						x	x	x	
15000							x	x	x
20000								x	x
25000									x

In addition to preparing a preliminary irradiation testing program as outlined in Table 8, the current radiation field characterization effort also tried to identify potential locations within the canister-cask geometry for physical integration of the photoconverter materials. This task was somewhat complicated by the harsh thermal environment that is present in most areas within the cask. As an example, some of the maximum component temperatures for the normal storage condition for 24 design basis PWR assemblies were extracted from Ref. 8 and reproduced here in Table 9. Some observations based on these data are as follows:

1. With the high temperatures shown in Table 9 for the fuel region, it does not make sense to consider placing the photoconverter material within the fuel region -- especially since we expect the performance and stability of these materials to degrade at higher temperature.
2. Although Table 9 shows that the temperatures in the canister structural and shield lids are more reasonable (about 100 C), the gamma dose rate attenuates significantly through this area (see Fig. 11). Because of the low dose rates, this region is also not appropriate.
3. Although no explicit temperature is given for the He-filled gap region between the upper fuel end fittings and the canister shield lid, the peak temperatures here should still be near 100 C yet, the dose rate, which is about 800 rad/hr, may be reasonable for producing adequate power from the photoconverter materials. Thus, this region may be one deserving further consideration.
4. Another possible candidate location, this time outside the fuel storage canister, is the regions on either side of the cask's carbon steel liner. These locations are not ideal since, for safeguards concerns, the original goal was to make the photoconverter material an integral part of the sealed canister unit. However, the peak temperatures in the air, carbon steel liner, and the concrete near the steel shell are less than 100 C and, from previous discussion, the gamma dose rates here may be suitable for the intended application. Thus, these locations are also potential candidates for placement of the photoconverter materials.
5. Finally, it is apparent from the high temperatures (up to 100 C or more) that thermal considerations may be very important when evaluating the power production capability, material stability, and service lifetime of the overall energy conversion system. Therefore, temperature considerations must become an integral part of the planned testing program.

Table 9 Maximum component temperatures within the canister-cask storage system (data from Ref. 8).

Component	Maximum Temperature	
	^{o}F	^{o}C
Fuel Cladding	648	342
Heat Transfer Disk	599	315
Support Disk	601	316
Top Weldment	399	204
Bottom Weldment	159	71
Canister Shell	351	177
Canister Structural Lid	204	96
Canister Shield Lid	212	100
Concrete/Carbon Steel liner	186	86
Air at Outlet	173	57

In summary, this work has estimated the radiation field present within a typical canister-cask storage facility and it has identified three potential locations for the placement of the photoconverter materials for the new energy conversion system based on a trade-off in reasonable gamma dose rates and as low as possible temperatures for the photoconverter materials. The three locations include one position in the sealed canister (gap above the fuel) and two positions within the cask geometry (either side of the carbon steel concrete liner). The gamma dose rates vary considerably in these three locations (100 rad/hr to 10000 rad/hr), so a material-testing program that covers a wide range of dose rates and integral doses is envisioned.

The results here are preliminary because only the dominant component of the gamma source was used in the radiation transport calculations. Although this is certainly sufficient to help guide and parameterize the experimental program, further work to refine the estimates obtained here may be needed. Refinements to the current work will be made, as needed, after some preliminary results from the testing program become available.

References

18. B. O'Regan and M. Graetzel "A Low Cost High Efficiency Solar Cell Based on Dye-sensitized Colloidal TiO_2 Films,**" Nature**, **353**, 737 (1991).

19. M. Graetzel, "Molecular Photovoltaics that Mimic Photosynthesis," **Pure Appl. Chem.**, **73**, 459 (2001).

20. "DOORS3.2a - One, Two, and Three Dimensional Discrete Ordinates Neutron/Photon Transport Code System," Radiation Safety Information Computational Center, CCC-650 (2003).

21. "BUGLE-96 - Coupled 47 Neutron, 20 Gamma-Ray Cross Section Library Derived from ENDF/B-VI for LWR Shielding and Pressure Vessel Dosimetry Applications," Radiation Safety Information Computational Center, DLC-185 (1996).

22. "SCALE 5: Modular Code System for Performing Standardized Computer Analyses for Licensing Evaluation for Workstations and Personal Computers," Radiation Safety Information Computational Center, CCC-725 (2004).

23. J. R. White, A. Jirapongmed, and J. Byard, "Preliminary Characterization of the Irradiation Facilities Within the LEU-Fueled UMass-Lowell Research Reactor," Proceedings of Topical Meeting on Advances in Reactor Physics and Mathematics and Computation, Pittsburgh, PA (May 2000).

24. J. R. White, J. Byard, and A. Jirapongmed, "Calculational Support for the Startup of the LEU-Fueled UMass-Lowell Research Reactor," Proceedings of Topical Meeting on Advances in Reactor Physics and Mathematics and Computation, Pittsburgh, PA (May 2000).

25. "Final Safety Analysis Report for the UMS Universal Storage System," NAC International, Docket No. 72-1015 (March 2004).

26. A. B. Chilton, J. K. Shultis, and R. E. Faw, **Principles of Radiation Shielding**, Prentice Hall, Inc. (1984).